Please cite this article in press as: Veeckmans et al., Ferroptosis inhibition enhances liver and lung graft function, Cell (2026), https://doi.org/10.1016/j.cell.2026.04.024

Cell

CellPress
OPEN ACCESS

Article

Ferroptosis inhibition enhances liver and lung graft function

Geraldine Veeckmans,[1,16] Lene Devos,[2,16] Nicholas Gilbo,[3,4,16] Dieter Van Beersel,[5,6,16] Camilla Scarpellini,[7,16] Joris Blondeel,[2,12] Magali Walravens,[1] Greta Klejborowska,[7] Caroline Lanthier,[7] Michele Wölk,[8] Sebastian Müller,[9] Christine Gaillet,[9] Ludovic Colombeau,[9] Behrouz Hassannia,[1] Matthias Längin,[10] Martin Bender,[10] Jan-Michael Abicht,[10] Bruno Reichart,[11] Hans De Winter,[7] Maria Fedorova,[8] Raphaël Rodriguez,[9] Jacques Pirenne,[2,12] Laurens J. Ceulemans,[13,14] Ina Jochmans,[2,12,16] Koen Augustyns,[7,16] Diethard Monbaliu,[2,12,16] Arne Neyrinck,[5,6,16] and Tom Vanden Berghe[1,15,16,17,18,*]

[1]Cell Death Signaling Lab, Department of Biomedical Sciences, Inflamed Centre of Excellence, University of Antwerp, Antwerp, Belgium
[2]Transplantation Research Group, Department of Microbiology, Immunology, and Transplantation, KU Leuven, Leuven, Belgium
[3]Department of Visceral Surgery and Transplantation, CHU Liège, University of Liège, Liège, Belgium
[4]Centre de Recherche et d'Enseignement du Département de Chirurgie (CREDEC), GIGA Metabolism and Cardiovascular Biology, University of Liège, Liège, Belgium
[5]Anesthesiology and Algology, Department of Cardiovascular Sciences, KU Leuven, Leuven, Belgium
[6]Department of Anesthesiology, University Hospitals Leuven, Leuven, Belgium
[7]Medicinal Chemistry Research Group, Department of Pharmaceutical Sciences, University of Antwerp, Antwerp, Belgium
[8]Center of Membrane Biochemistry and Lipid Research, University Hospital Carl Gustav Carus and Faculty of Medicine of TU Dresden, Dresden, Germany
[9]Institut Curie, CNRS, INSERM, PSL Research University, Paris, France
[10]Department of Anaesthesiology, University Hospital, LMU Munich, Munich, Germany
[11]Walter Brendel Centre of Experimental Medicine, LMU Munich, Munich, Germany
[12]Abdominal Transplantation, University Hospitals Leuven, Leuven, Belgium
[13]Department of Thoracic Surgery, University Hospitals Leuven, Leuven, Belgium
[14]Department of Chronic Diseases and Metabolism (CHROMETA), Laboratory of Respiratory Diseases and Thoracic Surgery (BREATHE), KU Leuven, Leuven, Belgium
[15]Department of Biomedical Molecular Biology, Ghent University, Ghent, Belgium
[16]These authors contributed equally
[17]Senior author
[18]Lead contact
*Correspondence: tom.vandenberghe@uantwerpen.be
https://doi.org/10.1016/j.cell.2026.04.024

SUMMARY

Ischemia-reperfusion injury (IRI) is a major clinical challenge in transplantation, vascular surgeries, myocardial infarction, and stroke. Disruption of energy and redox homeostasis triggers ferroptosis, a regulated, iron-dependent form of cell death, leading to organ dysfunction. We identify an early and transient increase of lipid peroxidation in human liver transplants and validate it as a therapeutic target. FXT-001, a ferroptosis inhibitor with dual radical and iron-trapping activity, provides robust protection in preclinical models, including *ex situ* perfusion of porcine liver and lung grafts. In a split *ex vivo* machine perfusion setting using declined human donors, FXT-001 treatment preserves graft viability, whereas untreated lungs deteriorate. We also develop FXT-002 and FXT-003 with enhanced pharmacokinetic and safety profiles. These findings support the use of ferroptosis inhibitors as a therapeutic strategy in transplantation and other IRI-associated conditions.

INTRODUCTION

Ischemia-reperfusion injury (IRI) is a major clinical complication associated with myocardial infarction, cardiovascular surgery, stroke, and organ transplantation.[1] The initial deprivation of oxygen and nutrients during ischemia disrupts cellular homeostasis, while subsequent reperfusion exacerbates tissue damage through oxidative stress, immune activation, and regulated cell death.[1] Among the various cell death pathways implicated in IRI, ferroptosis—a regulated, iron-dependent form of necrotic cell death driven by lipid peroxidation—has emerged as a key contributor to parenchymal injury and long-term organ dysfunction.[2–4] Ferroptosis executes from a self-propagating cycle of excessive lipid peroxidation within cellular membranes, driven by unbound redox-active iron and molecular oxygen, which disrupts membrane integrity and results in cell death.[2] Under physiological conditions, cells counterbalance this process by controlling the lipid saturation level,[2] the labile iron pool,[5] and the

Please cite this article in press as: Veeckmans et al., Ferroptosis inhibition enhances liver and lung graft function, Cell (2026), https://doi.org/10.1016/j.cell.2026.04.024

propagation of radical chain reactions within cellular membranes.[6]

Despite growing recognition of its role in IRI, no approved therapies effectively target ferroptosis in clinical settings.[7] When natural defenses fail to detoxify phospholipid peroxides mediated by, e.g., glutathione peroxidase 4 (GPX4),[8] synthetic lipophilic radical-trapping agents (RTAs) have demonstrated potent cytoprotective effects in preclinical models.[6] However, poor *in vivo* stability and the limited solubility of several first-generation ferroptosis inhibitors have hindered clinical translation. FXT-001 (formerly UAMC-3203), a best-in-class analog of ferrostatin-1,[9] exhibits favorable drug-like properties and therapeutic potential across multiple ferroptosis-driven disease models. We and others have shown that ferroptosis inhibition mitigates IRI in liver,[8,10,11] kidney,[4,11,12] heart,[13–15] intestine,[16] pancreas,[17] and brain[18–20] in rodents. Moreover, elevated circulating levels of malondialdehyde (MDA)—a biomarker of lipid peroxidation—correlate with poor outcomes in liver transplant recipients, underscoring the clinical relevance of ferroptosis in transplantation.[21]

Organ transplantation remains a life-saving therapy for patients with end-stage organ failure, yet 10%–20% of waitlisted individuals die before receiving a graft.[1] To expand the donor pool, transplant centers increasingly rely on higher-risk organs, for which machine perfusion has become a promising strategy to assess and improve graft quality *ex situ*.[22] This perfusion window offers a unique opportunity to intervene pharmacologically and limit ferroptosis-mediated damage prior to implantation.

Here, we report on the development of next-generation ferroptosis inhibitors (FXT-002 and FXT-003), and demonstrate that FXT-001 confers robust protection against lipid peroxidation-driven injury in *ex situ* perfusion models of porcine livers and both porcine and human lungs. These findings provide a translational foundation for targeting ferroptosis in clinical transplantation and other IRI-associated conditions.

RESULTS

Favorable lead ferroptosis inhibitors

To complete the lead optimization of FXT-001 (Figure 1A), we conducted comprehensive absorption, distribution, metabolism, and excretion (ADME) and safety profiling. FXT-001 potently inhibited ferroptotic cell death in the nanomolar range, displayed high thermodynamic solubility across a broad pH range (pH 2–7), and showed moderate lipophilicity based on both experimental $LogD_{7.4}$ and predicted calculated logP (cLogP) values (Figure 1B). The compound was highly stable for up to 2 h in phosphate-buffered saline (PBS, pH 7.4) as well as in mouse and human plasma, with binding to plasma proteins (Figure 1B). FXT-001 exhibited moderate intrinsic clearance in mouse, human, and rat microsomes (Figure 1B). By contrast, clearance was high in dog and minipig microsomes and in hepatocytes across all species tested (Figure 1B).

In vitro toxicological assessment revealed low cytotoxicity, resulting in a favorable selectivity index (Figure 1C). No signs of mitochondrial toxicity, genotoxicity, cardiotoxicity, mutagenicity, or reactive metabolite formation were observed (Figure 1C). At high micromolar concentrations, evidence of phospholipidosis was noted (Figure 1C), a known class effect of cationic amphiphilic drugs and a potential risk factor for tissue phospholipid accumulation.[23] FXT-001 showed no relevant inhibition of major cytochrome P450 (CYP450) enzymes, except for moderate inhibition of CYP3A4 in the presence of midazolam (Figure 1C). Off-target screening identified 13 proteins with >50% inhibition, most of which are predominantly expressed in the central nervous system (Figure 1C).

Pharmacokinetic profiling in mice following intravenous administration revealed a time-dependent decline in plasma levels (Figure 1D), which was indicative of rapid tissue redistribution. Accordingly, FXT-001 concentrations in kidney, liver, lung, heart, and epididymal and inguinal adipose tissue were highest at 0.5 h and subsequently declined over time (Figure 1E). In line with its lack of *in vitro* blood-brain barrier (BBB) permeability (Figure 1B), only low and intermittent brain concentrations were detected (Figure 1E). Oral bioavailability was limited (Figure 1D).

To strengthen the preclinical pipeline, we identified two next-generation analogs, FXT-002 and FXT-003. From a library of more than 250 radical-trapping compounds synthesized in our laboratory, FXT-002 and FXT-003 were selected as the top-performing candidates. Both analogs retained the potency and solubility of FXT-001 (Figure S1A) while exhibiting enhanced microsomal stability and no evidence of phospholipidosis (Figure S1A). Following intravenous administration, they displayed pharmacokinetic profiles similar to FXT-001 (Figures S1B and S1D–S1H), with FXT-002 notably demonstrating improved oral bioavailability (Figure S1C).

In a mouse model of iron-overload-induced multi-organ dysfunction,[4] FXT-002 and FXT-003 showed comparable therapeutic efficacy to FXT-001, significantly reducing plasma injury markers (Figures S1I–S1K). Moreover, both compounds improved survival, rescuing 50%–60% of mice, to a similar extent as FXT-001 in this extremely severe injury model (Figure S1L). Collectively, these findings support FXT-001 as a promising lead compound with favorable drug-like properties and highlight FXT-002 and FXT-003 as next-generation ferroptosis inhibitors with promising pharmacokinetic and safety profiles.

FXT-001 modulates lipid radical chain reactions and subcellular iron homeostasis

To shed light on the mechanism of action (MoA) of FXT-001, we synthesized a biologically active alkyne-containing analog (C_1FXT-001) to perform *in situ* click labeling and cell imaging using confocal fluorescence microscopy[24] (Figure 2A). Colocalization analysis revealed broad distribution across subcellular compartments, with particularly strong correlation in the mitochondria followed by the endoplasmic reticulum, endolysosomes, and the Golgi apparatus[25] (Figures 2B, 2C, and S2A–S2C).

To test the functional role of lipophilicity, we designed two analogs with reduced lipophilicity: L_1FXT-001 (cLogP = 0.4) and L_2FXT-001 (cLogP = 2.4) (Figure 2D). Neither compound demonstrated RTA activity in liposomal membranes as assessed by the fluorescence-enabled inhibited autoxidation (FENIX) assay (Figure 2F), despite retaining similar antioxidant capacity to FXT-001 in the 2,2-diphenyl-1-picrylhydrazyl (DPPH) assay (Figure 2E). Consistently, both analogs failed to protect cells

Please cite this article in press as: Veeckmans et al., Ferroptosis inhibition enhances liver and lung graft function, Cell (2026), https://doi.org/10.1016/j.cell.2026.04.024

CellPress
OPEN ACCESS

A

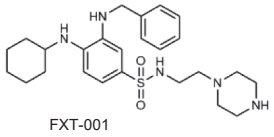

B

ADME		
IC_{50}		10 ± 7 nM
HT thermodynamic solubility	pH 2	8094 µM
	pH 7	6900 µM
LogD	pH 7.4	2.43
cLogP		4.2
Chemical stability	pH 7.4	100%
Plasma stability	human	100%
	mouse	93%
Plasma Protein Binding *(fraction unbound)*	human	6.1 %
	mouse	3.7 %
Microsomal stability *(µl/min/mg protein)*	human	29.3
	mouse	48.0
	rat	23.3
	dog	126
	minipig	231
Hepatocyte stability *(µL/min/10^6 cells)*	human	21.2
	mouse	60.0
	rat	40.8
	dog	61.9
	minipig	46.9
MDCK-MDR1		Not permeable

C

Safety and Toxicity		
EC_{50}		19.5 µM (SI > 2000)
Mitochondrial toxicity		Non-mitotoxic Glu/Gal: 1.03
Cardiotoxicity	hERG channel inhib.	43% inhib. at 10 µM
	Ion channel inhib.	Nav1.5 IC_{50} > 30 µM
		Cav1.2 IC_{50} > 30 µM
Genotoxicity	Micronucleus	AC_{50} = 21.9 µM (3h)
		AC_{50} > 100 µM (24h)
	Ames fluctuation	Not mutagenic
Reactive metabolite formation *(Glutathione trapping)*		Non
Phospholipidosis		AC_{50} = 15 µM
CYP450 *Inhibition assay*	CYP1A2	IC_{50} > 25 µM
	CYP2B6	IC_{50} > 25 µM
	CYP2C8	IC_{50} > 25 µM
	CYP2C9	IC_{50} > 25 µM
	CYP2C19	IC_{50} > 25 µM
	CYP2D6	IC_{50} > 25 µM
	CYP3A4	IC_{50} = 14.8 µM [a]
		IC_{50} = 3.88 µM [b]
Off-target activities *(Safety Screen 87 Panel)*		13 targets Response > 50%

D

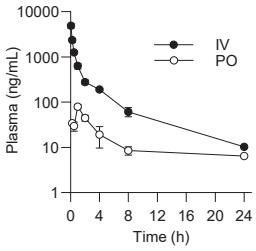

E

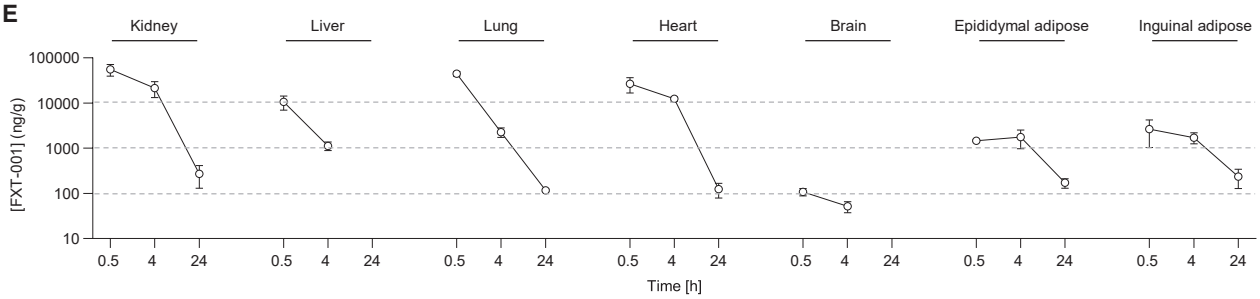

Figure 1. FXT-001 exhibits favorable ADME properties, pharmacokinetics, and safety-toxicity profile

(A) Chemical structure of FXT-001.

(B) ADME properties of FXT-001. Ferroptosis inhibition (half maximal inhibitory concentration [IC_{50}], HT1080 cells, n = 6, mean ± SD). High-throughput thermodynamic solubility (24 h, USP-grade buffer). LogD (n-octanol/0.1 M phosphate buffer). cLogP (using Collaborative Drug Discovery [CDD] Vault software). Chemical stability (2 h, phosphate buffer, pH 7.4, 37°C). Plasma stability (2 h, 37°C). Plasma protein binding (unbound fraction 4 h, 0.1 M phosphate buffer, pH 7.4, 37°C). Microsomal stability. Hepatocyte stability. Permeability assay using Madin-Darby canine kidney (MDCK) originating cell line with overexpression of MDR1 gene (encoding for P-gp protein) (1 h, 10 µM, HBSS, pH 7.4, 37°C, n = 2).

(C) Safety and toxicity profile of FXT-001. Cytotoxicity (half maximal effective concentration [EC_{50}], HepG2 cells, n = 3, mean). Glucose/galactose fold change (activation concentration 50% [AC_{50}] ratio, n = 3). Cardiotoxicity, potassium (hERG), sodium (Nav1.5) or calcium channel (Cav1.2) inhibition. Genotoxicity, micronucleus test (AC_{50}, TK6 cells, n = 3) and Ames fluctuation test. Reactive metabolite formation (1 h, human microsomes ± (un)labeled glutathione [GSH]). Phospholipidosis (AC_{50} ratio, HepG2 cells, 72 h, n = 3). CYP450 inhibition (IC_{50}, 7 isoforms, 8 substrates, 6 concentrations, 5–15 min incubation, 37°C). Off-target activities of FXT-001 (Safety Screen87 Panel, Eurofins).

(D) Plasma distribution of FXT-001 (10 mg/kg) following intravenous (i.v.) or oral administration (PO) in CD-1 male mice (n = 3–6 per time point). Data are mean ± SEM.

(E) Tissue distribution of FXT-001 (10 mg kg^{-1}, i.v.) in kidney, liver, lung, heart, brain, and epididymal and inguinal adipose tissue of CD-1 male mice (n = 3–6 per time point; mean ± SEM). [a]Substrate testosterone; [b]Substrate midazolam.

See also Figure S1 and Table S1.

from ML162-induced cell death, which is in contrast to the strong protection observed with FXT-001 (Figure 2G).

To further interrogate membrane interactions, we performed umbrella sampling (US) and classical molecular dynamics (cMD) simulations of FXT-001 and L_1FXT-001 in a phospholipid bilayer. FXT-001 showed stable insertion, with its piperazine moiety interacting with phospholipid head groups and its lipophilic core embedding within the acyl chains, which is consistent with effective membrane-localized RTA activity (Figure 2H; Video S1). In contrast, L_1FXT-001 exhibited a positive potential of mean force (PMF) when translocating into the membrane, indicating an energetically unfavorable insertion profile (Figure 2H).

The *o*-phenylenediamine moiety in FXT-001 contributes to its RTA activity and is also known to bind iron.[26,27] To interrogate the functional importance of this moiety, we synthesized an inactive analog, RFXT-001, by substituting the aniline nitrogens with a carbonyl group (Figure 2I). This modification abolished antioxidant activity in both the DPPH and FENIX assays (Figures 2J and 2K) and eliminated Fe^{3+}-binding capacity, as assessed by nuclear magnetic resonance (^{1}H NMR) (Figures S2D–S2F). Notably, FXT-001 altered intracellular iron distribution, increasing mitochondrial iron content as measured by a mitochondrial-specific Fe^{2+} turn-off fluorescent probe[28] (Figures 2M, S2G, S2K, and S2L) and inductively coupled plasma mass spectrometry (ICP-MS) (Figures 2N, S2M, and

Please cite this article in press as: Veeckmans et al., Ferroptosis inhibition enhances liver and lung graft function, Cell (2026), https://doi.org/10.1016/j.cell.2026.04.024

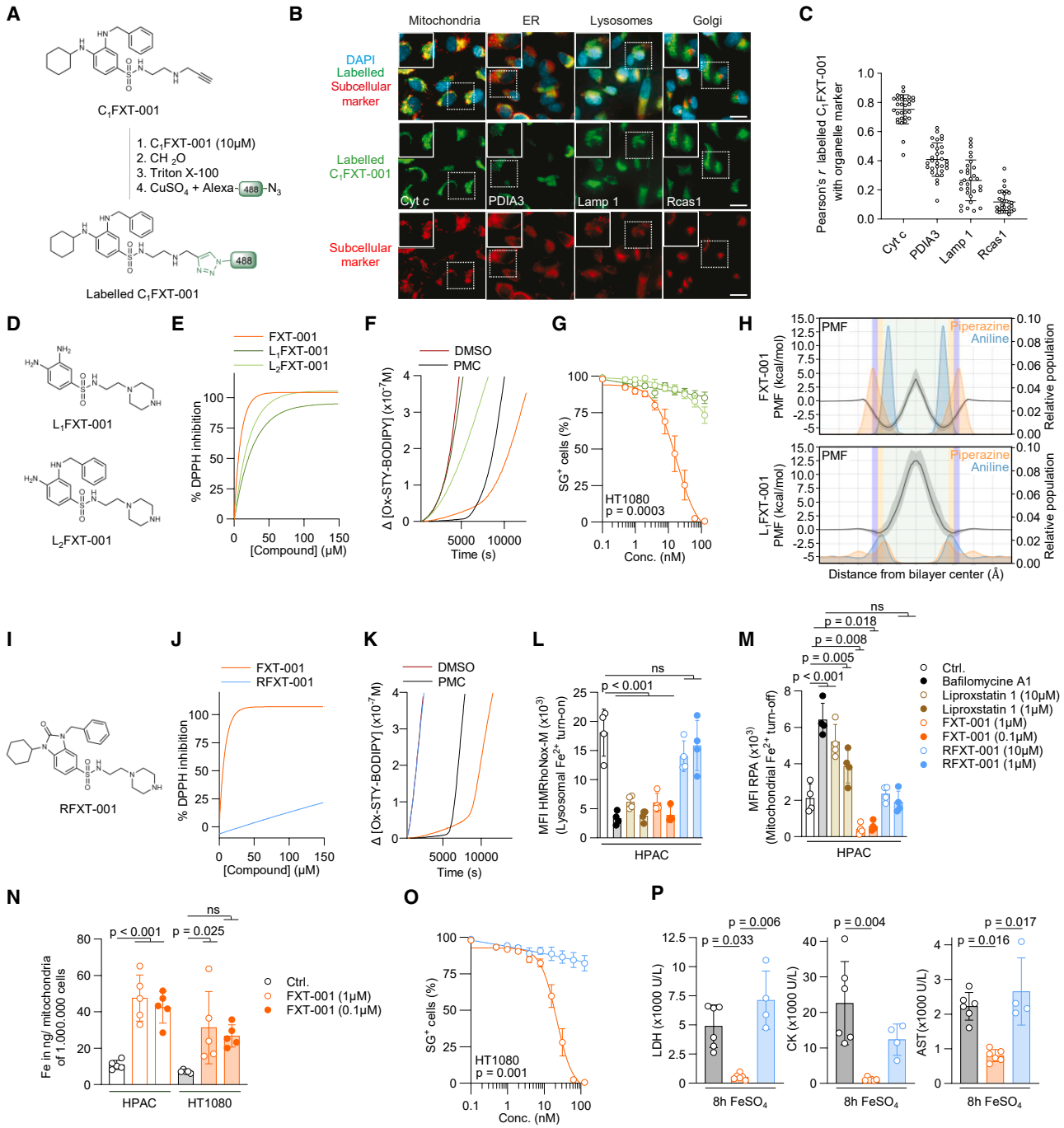

Figure 2. FXT-001 controls subcellular lipid radical propagation and iron homeostasis

(A) Chemical structure of C_1FXT-001 and labeled C_1FXT-001.

(B) Fluorescence microscopy images showing C_1FXT-001 labeled with Alexa Fluor 488 Azide in HT1080 treated cells (10 μM for 1 h). Monoclonal antibodies against cytochrome *c*, protein disulfide isomerase family A member 3 (PDIA3), lysosomal-associated membrane protein 1 (LAMP1), and receptor-binding cancer-associated surface antigen 1 (RCAS1) were used to stain the mitochondria, endoplasmic reticulum, lysosomes, and Golgi apparatus, respectively. 4′,6-diamidino-2-phenylindole (DAPI) was used to stain nuclear DNA. Scale bar represents 20 μm. A 60× objective was used for acquisitions and images were acquired as z stacks.

(C) Pearson's correlation coefficient used to assess the linear correlation between the intensity values of corresponding individual pixels in the fluorescent channels. Data are the mean ± SD.

(D) Chemical structure of L_1FXT-001 and L_2FXT-001.

(E) DPPH assay to determine the cell-free radical scavenging activity of FXT-001, L_1FXT-001, and L_2FXT-001.

(legend continued on next page)

Please cite this article in press as: Veeckmans et al., Ferroptosis inhibition enhances liver and lung graft function, Cell (2026), https://doi.org/10.1016/j.cell.2026.04.024

S2N). In parallel, a reduction in chemically reactive lysosomal Fe^{2+} was observed using a lysosomal-specific Fe^{2+} turn-on probe[29] (Figures 2L and S2H–S2J). These effects were absent in cells treated with RFXT-001 (Figures 2L–2N and S2G–S2N). Consistent with these findings, the ferroptosis-protective effect observed with FXT-001 in cellular models was lost upon substitution with RFXT-001 (Figure 2O), as was the reduction in plasma injury markers in an iron overload-induced multi-organ dysfunction *in vivo* (Figure 2P). Collectively, these findings demonstrate that the efficacy of FXT-001 critically depends on its lipophilic anchors and *o*-phenylenediamine moiety, which is essential for suppressing lipophilic radical chain reactions and modulating subcellular iron distribution upon direct binding.

FXT-001 attenuates liver injury and improves function in a porcine transplant setting

Lipid peroxidation proceeded under hypothermic conditions (4°C), and FXT-001 effectively suppressed ML162-induced ferroptotic cell death in human epithelial cells (HT1080) (Figure S3A). Similarly, elevated levels of MDA were observed in both porcine liver and bile duct tissue following static cold storage (SCS), which is indicative of oxidative stress during cold ischemia (Figures S3B–S3F). Analysis of tissue concentration confirmed hepatic accumulation of FXT-001 following administration via cold flush with preservation solution in the porcine model. Hepatic concentrations in porcine livers exposed to 4 h of cold ischemia ranged from 0.08 to 0.48 μM and from 0.44 to 2.47 μM when preceded by 1 h of warm ischemia (Figure S3G).

To assess therapeutic efficacy, FXT-001 was investigated in a porcine model of liver donation after circulatory death (DCD), which consists of 1 h of warm ischemia and 6 h of isolated reperfusion with leucocyte-containing blood, to mimic transplantation (Figure 3A; Video S2).[30] Porcine livers received either vehicle or FXT-001 treatment via the back-table flush and SCS preservation solution. Following 4 h SCS and 6 h reperfusion, hepatocellular injury markers, including aspartate aminotransferase (AST), alanine transaminase (ALT), and lactate dehydrogenase (LDH), were significantly elevated (Figures 3B–3D). FXT-001 treatment significantly reduced ALT over time (Figure 3B), and the area under the curve (AUC) for AST release in perfusate was reduced by 40% compared with vehicle controls (Figure S3H).

Both groups showed bile production (Figure 3E), progressive decreases in glucose (Figure 3G) and lactate (Figure 3H), and maintained a stable pH during reperfusion (Figure S3J). Although FXT-001 treatment was associated with a non-significant increase in bile production (Figure S3I), bile volume inversely correlated with AST levels (Figure 3F), confirming that less-injured livers have better preserved choleretic function. FXT-001 significantly altered glucose metabolism, with higher glucose concentrations observed at the onset of reperfusion (30 min) and significantly faster clearance in treated livers (Figure 3G). As glucose uptake primarily occurs in ischemia-prone pericentral hepatocytes, these findings suggest that FXT-001 protects the hepatic lobule region most susceptible to IRI.

FXT-001 did not affect pro-inflammatory cytokines (interleukin [IL]-1β, IL-6, IL-8, and tumor necrosis factor [TNF]-α) (Figures S3K–S3N) but significantly increased IL-10 (Figure 3I), whereas the overall reduction in pro-fibrotic TGF-β was not significant (Figure 3J). Histopathological injury scores, 4-hydroxynonenal (4-HNE) and terminal deoxynucleotidyl transferase dUTP nick end labeling (TUNEL) staining (Figures S3S–S3U), and lipidomic profiles (Figures 3K–3N) were similar between groups, likely reflecting the regional heterogeneity of liver injury. Likewise, MDA levels in liver tissue (Figure S3O), bile duct tissue (Figure S3P), and bile (Figure S3Q) remained unchanged. However, perfusate MDA

(F) FENIX assay to determine lipid radical-trapping activity of FXT-001, L_1FXT-001, and L_2FXT-001. DMSO was used as negative control and 2,2,5,7,8-pentamethyl-6-chromanol (PMC) was used as positive control.
(G) Percentage of Sytox Green-positive HT1080 cells pretreated with 100 nM ML162, followed by FXT-001, L_1FXT-001, or L_2FXT-001 (125–0.488 nM). Fluorescence (485/520 nm) measured at 24 h; mean ± SEM (n = 3).
(H) Graphical overview showing the preferred binding locations of FXT-001 and L_1FXT-001. PMF (black) and compound distributions (blue, orange) are plotted as a function of the distance between the compound and the center of the membrane bilayer. The gray shaded area in the PMF plot denotes the spread between the three replicas, defined by the minimum and maximum values of each property. Choline (purple) and phosphate (yellow) membrane layers, as well as the lipid bilayer itself (light green), are shown as vertical bars. The locations of these layers are approximate and solely serve for visualization purposes. The distribution of the aniline and piperazine group of each compound was calculated from the distance between the centers of geometry of their respective nitrogens to the lipid bilayer center.
(I) Chemical structure of RFXT-001.
(J) DPPH assay to determine the cell-free radical scavenging activity of FXT-001 and RFXT-001.
(K) FENIX assay to determine lipid radical-trapping activity of FXT-001 and RFXT-001. DMSO was used as negative control and PMC was used as positive control.
(L and M) Flow cytometry of human glucocorticoid-sensitive pancreatic ductal adenocarcinoma (HPAC) cells treated with the indicated compound for 5 h and then with the lysosomal iron(II) turn-on probe HMRhoNox-M or mitochondrial iron(II) turn-off probe rhodamine B-[(1,10-phenanthroline-5-yl)aminocarbonyl]benzyl ester (RPA) for 1 h. Data are the mean ± SD (n = 4). MFI, mean fluorescence intensity.
(N) Total iron content in mitochondria measured by ICP-MS. Data are the mean ± SD (n = 4). Data generated using both HPAC and HT1080 cells.
(O) Percentage Sytox Green-positive HT1080 cells pretreated with 100 nM ML162, followed by FXT-001 or RFXT-001 (125–0.488 nM). Fluorescence (485/520 nm) measured at 24 h; mean ± SEM (n = 3).
(P) Plasma levels of LDH, creatine kinase (CK), and AST in mice subjected to acute iron overload (intraperitoneal [i.p.] 250 mg kg^{-1}) 8 h after treatment with vehicle (n = 6) or equimolar amounts of FXT-001 (i.p. 12 mg kg^{-1}; n = 6) or RFXT-001 (i.p. 11 mg kg^{-1}; n = 4). Data are the mean ± SD. Statistical differences shown for the cell death assays were analyzed using one-way ANOVA (G, p = 0.0003 at 125 nM) and unpaired, two-tailed t test (O, p = 0.0011 at 125 nM). Differences in the frequency distribution of the compounds (FXT-001 vs. L_1FXT-001) were assessed using a chi-squared goodness-of-fit test (H, $p < 0.001$). Ordinary one-way ANOVA followed by a Sidak test was used to compare differences between the groups (L–N). *In vivo* data (P) were analyzed using Kruskal-Wallis followed by Dunn's post hoc test.
See also Figure S2, Methods S1, Data S1, and Video S1.

Please cite this article in press as: Veeckmans et al., Ferroptosis inhibition enhances liver and lung graft function, Cell (2026), https://doi.org/10.1016/j.cell.2026.04.024

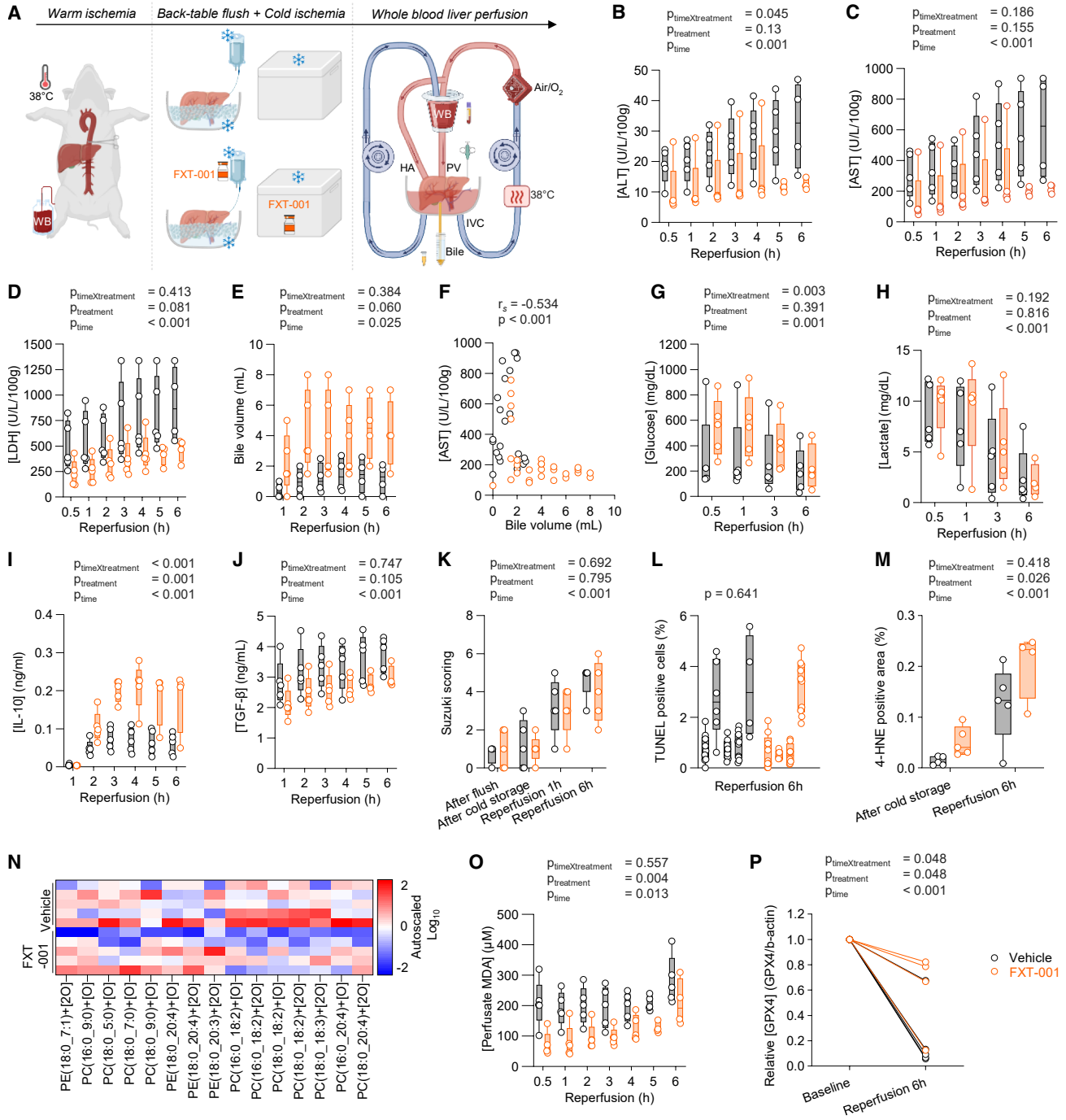

Figure 3. FXT-001 improves liver injury and function in a preclinical model of liver DCD

(A) Experimental setup of the pig model of liver DCD. After 60 min of warm ischemia (WI), FXT-001 was introduced during the back-table flush and in the preservation solution during cold storage (cold ischemia). Vehicle livers were exposed to preservation solution only. After cold storage, 6 h of whole blood (WB) liver perfusion was performed to mimic transplantation, during which needle biopsies, perfusate, and bile samples were collected.

(B–D) Perfusate AST, ALT, and LDH concentrations during reperfusion (n = 5 for both groups).

(E) Bile volume produced by each liver during reperfusion (n = 4 for vehicle; n = 5 for FXT-001).

(F) Dot plot of AST concentrations correlated to bile volume at 1–6 h of reperfusion.

(G and H) Perfusate glucose and lactate concentration during reperfusion, respectively (n = 5 for both groups).

(I and J) Perfusate concentration of IL-10 and TGF-β during reperfusion, respectively (n = 5 for both groups).

(K) Liver parenchyma injury score after back-table flush, cold storage and, 1 and 6 h of reperfusion determined using the Suzuki scoring that quantifies liver necrosis, congestion, and vacuolization.

(legend continued on next page)

Please cite this article in press as: Veeckmans et al., Ferroptosis inhibition enhances liver and lung graft function, Cell (2026), https://doi.org/10.1016/j.cell.2026.04.024

concentrations were significantly reduced in the FXT-001-treated group up until 5 h (Figure 3O), and degradation of GPX4 appeared attenuated toward the end of reperfusion (Figures 3P and S3R).

Despite limited clinical data linking ferroptosis to transplant injury, this evidence is critical for therapeutic translation. To address this, we first analyzed plasma samples from 116 liver transplant recipients collected perioperatively and through to postoperative day 5 for the extent of their lipid peroxidation.[31,32] Relative plasma MDA levels were significantly elevated during the early reperfusion phase, peaking at 30 min post reperfusion (Figures 4A and 4B) and correlating with serum AST concentrations at both 30 min (Figure S4A) and 6 h post reperfusion (Figure 4C). Notably, higher MDA levels were detected in patients with AST > 2,000 IU/L at 6 h post reperfusion (Figure 4D), a threshold accepted as a surrogate biomarker of severe hepatic IRI predicting graft failure and patient survival.[22] In contrast, MDA concentrations did not significantly differ between patients with or without early allograft dysfunction (EAD; Figure S4B),[33] nor did it correlate with established EAD risk factors such as donor age (Figure S4C), donor type (Figure S4D), cold ischemia time (Figure S4E), or model for end-stage liver disease (MELD) score (Figure S4F).

To further assess the translational relevance of lipid peroxidation in large-animal models, we examined plasma from 17 baboons undergoing orthotopic pig-to-baboon cardiac xenografts.[34,35] In this setting, MDA levels peak within 1 h following cardiopulmonary bypass, mirroring the early increase of lipid peroxidation observed in human liver transplant recipients (Figure S4G). These findings characterize lipid peroxidation dynamics in cardiac xenotransplantation and reinforce the role of ferroptosis in graft injury across species and organ types.

Taken together, these human and large-animal data establish MDA, a surrogate for lipid peroxidation, as a rapid and mechanistically relevant marker of acute transplant injury and demonstrate that FXT-001 mitigates liver damage and improves graft function by preventing phospholipid peroxidation in a clinically relevant pig model.

FXT-001 mitigates lung injury in porcine and human donor grafts

Given the high tissue oxygen pressure (PO_2) and cardiac output that passes through the pulmonary vasculature under physiological conditions, we hypothesized that lung tissue may be relatively resistant to ferroptosis. To test this, we first attempted to induce acute lung injury by administering iron overload (300 mg kg^{-1} $FeSO_4$) to non-injured porcine lungs maintained on an *ex vivo* lung perfusion (EVLP) system. This normothermic platform permits controlled mechanical ventilation and metabolic activity outside the body. Remarkably, within 1 h, the lung exhibited severe fluid accumulation and functional deterioration, which was accompanied by marked elevations in MDA levels in the perfusate, indicating rapid and severe lipid peroxidation (Figures S5A–S5D; Video S3).

Next, the effect of FXT-001 was investigated in a porcine EVLP model (Figure 5A; Video S4). Donor lungs were subjected to 3 h of warm ischemia, followed by 8 h of EVLP to assure reproducible lung IRI. At reperfusion onset, lungs were randomized to receive either vehicle or FXT-001 treatment via the perfusate. Non-injured lungs served as baseline controls under identical conditions. Baseline hemodynamic and perfusate parameters were comparable across all groups (Figure 5B; Videos S5 and S6).

Lung injury was quantified by the wet-to-dry (W/D) weight ratio, the gold standard for extravascular lung water and capillary leakage. FXT-001 treatment significantly reduced the W/D ratio in right lower lobe biopsies compared with vehicle (Figure 5C), with robust effects in 3 out of 5 grafts. Vehicle-treated lungs showed significantly higher W/D ratios relative to the non-ischemic controls, confirming injury severity. To capture regional organ differences, computed tomography (CT)-based lung density measurements of the left lung showed reduced water content in FXT-001-treated lungs (Figure 5D), with CT density strongly correlating with W/D ratios (Figure 5E). Representative CT images of lung grafts at the end of EVLP are shown in Figures 5F and S5E.

Graft performance was further assessed through physiological parameters. No significant differences were observed in static compliance (Cstat) (Figure 5G), pulmonary vascular resistance (PVR), or oxygenation capacity (arterial partial pressure of oxygen [PaO_2]/fraction of inspired oxygen [FiO_2] ratio) (Figures S5F and S5G). Histopathological injury (hematoxylin and eosin [H&E]) and 4-HNE stainings did not differ between treated and untreated lungs (Figures S5K and S5L). FXT-001 treatment significantly reduced perfusate levels of IL-6 and IL-8 (Figures 5H and 5I), while concentrations of interferon (IFN)-y, TNF-α, IL-1β, and IL-10 levels remained

(L) Percentage of TUNEL-positive cells after 6 h of reperfusion.
(M) Percentage of 4-HNE-positive area in liver tissue after cold storage and 6 h of reperfusion.
(N) Heatmap showing relative quantities of oxidized phospholipids in liver tissue at 6 h reperfusion. Oxidized lipids were relatively quantified by liquid chromatography-tandem mass spectrometry (LC-MS/MS). Isomeric species were summed as +[O]. PE, phosphatidylethanolamine; PC, phosphatidylcholine.
(O) Perfusate concentration of MDA during reperfusion (n = 5 for both groups).
(P) Relative liver protein concentration of GPX4 compared to β-actin (n = 5 for both groups). Longitudinal data were analyzed using two-way ANOVA or mixed-effects model when appropriate. Tukey's multiple comparison was applied to compare two conditions within the datasets (B–E, G–K, M, O, and P). Multiple-comparison analysis for (J) revealed a significant difference at 2 h (p = 0.0303), 3 h (p = 0.0001), 4 h (p = 0.0036), and 5 h (p = 0.0371). Multiple-comparison analysis for (O) showed statistically significant differences at 0.5 h (p = 0.0126), 1 h (p = 0.0148), 2 h (p = 0.0160), 3 h (p = 0.0278), 4 h (p = 0.0352), and 5 h (p = 0.0007), whereas no significant difference was observed at time point 6. Spearman correlations (r_s) were used to assess correlation between two variables (F). A nested t test was used to compare vehicle- and FXT-001-treated groups (L). Boxplots represent the 25–75 percentiles with the median indicated as a line in the middle and whiskers extending from minimum to maximum values (B–E, G–M, and O). Due to technical failure, two datapoints are missing in the FXT-001 group at 5 and 6 h of reperfusion (B–P).
See also Figure S3 and Video S2.

Please cite this article in press as: Veeckmans et al., Ferroptosis inhibition enhances liver and lung graft function, Cell (2026), https://doi.org/10.1016/j.cell.2026.04.024

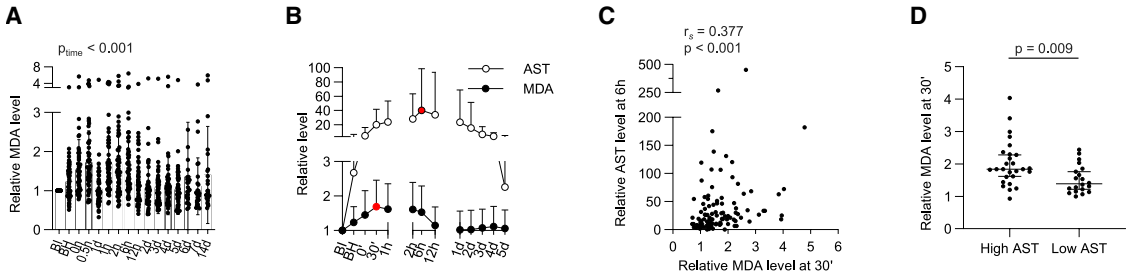

Figure 4. Early lipid peroxidation burst during liver transplantation

(A and B) Relative MDA and AST concentrations in plasma samples of liver transplant patients (n = 116 patients). BI, before incision; BH, before hepatectomy.
(C) Dotplot of relative AST concentration at 6 h of post transplantation correlated to relative MDA concentrations at 30 min post transplantation.
(D) Relative MDA concentration at 30 min post transplantation in patients with high AST (>2,000 IU/L) and low AST (<500 IU/L) concentration. Spearman correlations (r_s) were used to assess correlation between two variables (C). Longitudinal data were analyzed using mixed-effects model. Tukey's multiple comparison was applied to compare two conditions within the datasets (A). Mann-Whitney test was used to compare high and low AST patients (D). Barplots and *xy*-graphs are represented in means ± SD (A and B). Median and 95% confidence interval are shown in (D).
See also Figure S4.

unaffected (Figures S5H–S5J). MDA levels in sequential perfusate samples were significantly reduced after 7 and 8 h in the FXT-001 group, suggesting suppression of lipid peroxidation (Figure 5J).

To evaluate translational potential, we applied FXT-001 in a reconditioning protocol using human donor lungs declined for transplantation for having too low quality due to underlying (lung) pathology in the donor or for logistic reasons (Figure 6A). Right and left lungs were separated and perfused simultaneously on a split-EVLP system using STEEN preservation solution, with one lung receiving FXT-001 and the other vehicle (Figure 6B; Videos S7 and S8). FXT-001 reduced extravascular lung water, as indicated by lower W/D ratios, less weight gain (Figures 6C and 6D), and better preserved compliance (Figure 6E). Representative CT images of human lung grafts at the end of EVLP are shown in Figure 6F. Cytokine (IFN-γ, TNF-α, IL-1β, IL-6, IL-8, and IL-10) (Figures S6A–S6F) and MDA levels (Figure S6G) did not differ between the groups. Collectively, these results establish ferroptosis as a previously unrecognized driver of lung graft injury and demonstrate that treatment with the ferroptosis inhibitor FXT-001 confers functional and biochemical protection in both porcine and human donor lungs.

DISCUSSION

This study identifies FXT-001 as a potent, drug-like ferroptosis inhibitor with translational potential across multiple organ systems vulnerable to IRI. Through rigorous pharmacological profiling, mechanistic characterization, and validation in clinically relevant porcine and human *ex situ* liver and lung perfusion models, we demonstrate that FXT-001 mitigates ferroptosis-associated tissue damage and preserves graft function. Next-generation ferroptosis inhibitors, FXT-002 and FXT-003, with promising pharmacokinetic and safety profiles, might further strengthen the translational pipeline.

We observed organelle-specific localization of FXT-001, predominantly in mitochondria[36] and to a lower extent in endoplasmic reticulum[37,38] and endolysosomes,[39] which are subcellular compartments implicated in ferroptosis propagation and initiation, respectively. Mechanistically, the *o*-phenylenediamine moiety of FXT-001 is essential for both suppressing lipophilic radical chain reactions and modulating subcellular iron distribution, thereby directly impacting ferroptosis. Notably, lysosomal iron and lysosome-to-mitochondria iron transfer has recently been shown to contribute to ferroptosis vulnerability.[39–41] Structurally related analogs lacking either lipophilic anchoring or iron binding/radical-trapping capacity failed to inhibit lipid peroxidation or confer cellular protection. Complementary *in silico* simulations further support the functional importance of membrane partitioning and suggest that the amphiphilic nature of FXT-001 underlies its ability to prevent lipid oxidation *in situ*. The development of FXT-002 and FXT-003 builds on these findings by optimizing microsomal stability and minimizing phospholipidosis risk, a common concern among cationic amphiphilic compounds.[42] Both analogs demonstrated comparable life-saving efficacy *in vivo*, reinforcing the validity of the ferroptosis pathway as a druggable target in acute organ failure.

In porcine and human lung grafts, pharmacological inhibition with FXT-001 significantly improved the key clinical markers of reperfusion injury, including W/D ratio, edema formation, and lung compliance, and reduced biological MDA accumulation. In porcine liver grafts, FXT-001 preserved metabolic function and cellular integrity post reperfusion, as evidenced by reduced transaminase release, improved choleretic function, and modulated glucose clearance, which suggested a protective role in ischemia-prone pericentral hepatocytes.[43]

In clinical transplantation, organ protective measures can be administered in the donor, during static (hypothermic) preservation, dynamic machine perfusion, or post transplantation in the recipient. Importantly, we demonstrate ongoing lipid peroxidation during both static and dynamic preservation as well as early reperfusion. Specific organ treatment during these time intervals therefore represents a feasible strategy for the clinical translation of ferroptosis inhibition. However, additional dosing may be required to avoid partial exhaustion of the inhibitor and further reduce the MDA accumulation toward the end of reperfusion. While our perfusion models served both as therapeutic

Please cite this article in press as: Veeckmans et al., Ferroptosis inhibition enhances liver and lung graft function, Cell (2026), https://doi.org/10.1016/j.cell.2026.04.024

CellPress
OPEN ACCESS

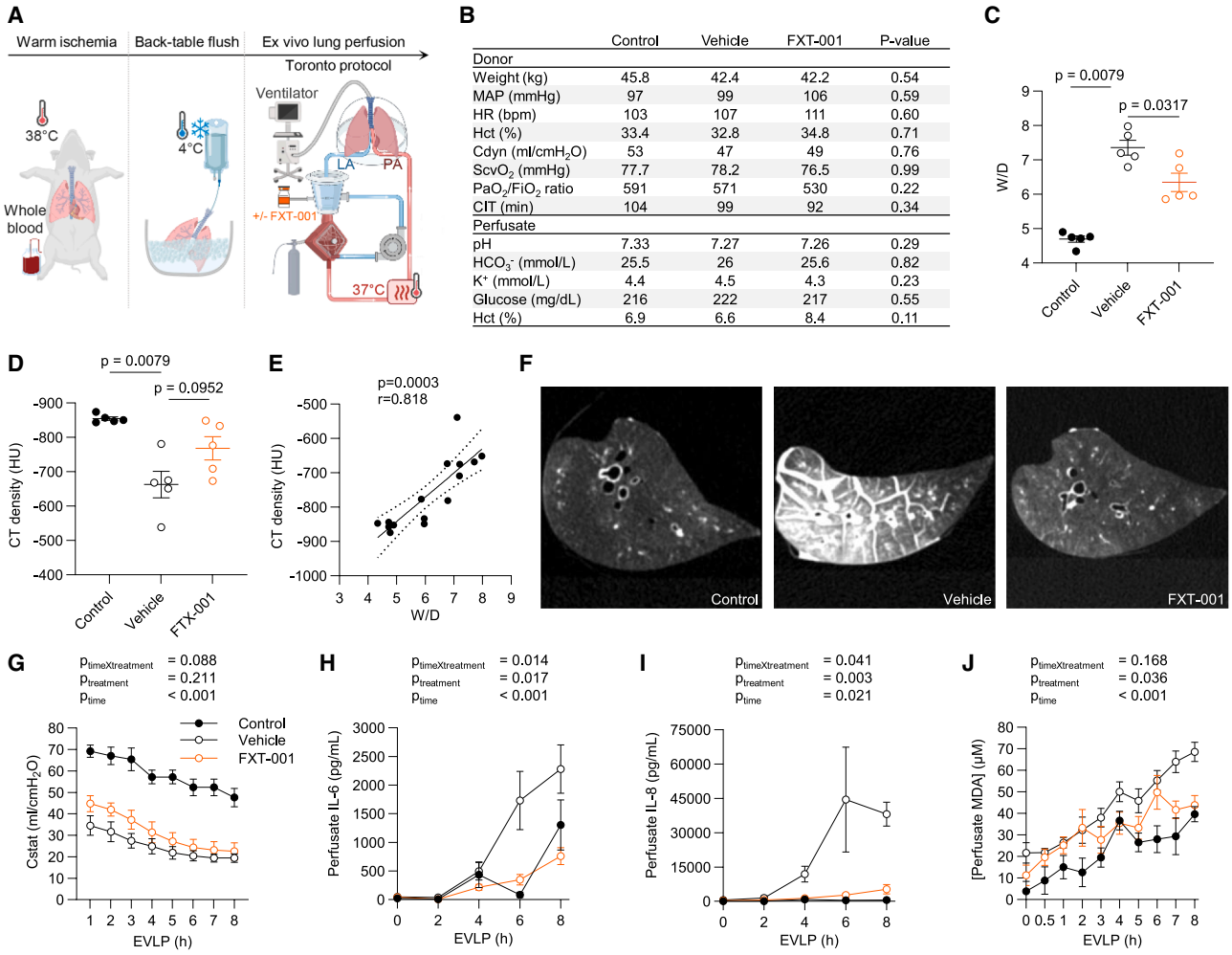

	Control	Vehicle	FXT-001	P-value
Donor				
Weight (kg)	45.8	42.4	42.2	0.54
MAP (mmHg)	97	99	106	0.59
HR (bpm)	103	107	111	0.60
Hct (%)	33.4	32.8	34.8	0.71
Cdyn (ml/cmH_2O)	53	47	49	0.76
$ScvO_2$ (mmHg)	77.7	78.2	76.5	0.99
PaO_2/FiO_2 ratio	591	571	530	0.22
CIT (min)	104	99	92	0.34
Perfusate				
pH	7.33	7.27	7.26	0.29
HCO_3^- (mmol/L)	25.5	26	25.6	0.82
K^+ (mmol/L)	4.4	4.5	4.3	0.23
Glucose (mg/dL)	216	222	217	0.55
Hct (%)	6.9	6.6	8.4	0.11

Figure 5. FXT-001 protects porcine lung grafts during EVLP

(A) Experimental *ex vivo* porcine perfusion model used to evaluate the efficacy of FXT-001 in blocking IRI during normothermic machine perfusion. Porcine lung grafts underwent 3 h of WI in the donor animal, followed by back-table cold flush. All grafts were then perfused for 8 h on an EVLP system following the Toronto protocol, using a closed atrium and WB supplementation. The vehicle and control lungs ($n = 5$ per group) received no additives in the perfusate, while the FXT-001 group ($n = 5$) received the ferroptosis inhibitor dissolved in the perfusate at the onset of reperfusion. The control lungs were cold flushed without prior WI.

(B) Baseline animal and perfusate parameters. Values are depicted as mean ± 25%–75% interquartile range.

(C) W/D lung weight ratios at 8 h of normothermic EVLP.

(D) CT-based density measurements of porcine lungs after 8 h of normothermic EVLP.

(E) Correlation between CT density measurements and W/D ratios.

(F) Representative CT images of porcine lung grafts.

(G) Cstat of porcine lungs at different time points during EVLP.

(H and I) IL-6 (H) and IL-8 (I) concentrations in porcine lung perfusate at baseline, 2, 4, 6, and 8 h of normothermic EVLP.

(J) Perfusate MDA concentrations measured at baseline and at different time points during porcine normothermic EVLP. MAP, mean arterial pressure; HR, heart rate; Hct, hematocrit; Cdyn, dynamic compliance; $ScvO_2$, central venous oxygen saturation; PaO_2, arterial partial pressure of oxygen; FiO_2, fraction of inspired oxygen; CIT, cold ischemic time; HCO_3^-, bicarbonate; K^+, potassium; IL, interleukin. A Kruskal-Wallis test was used to compare baseline pig parameters, with values presented as mean and interquartile range (25%–75%) (B). All other data are presented as mean ± SEM. A Mann-Whitney test was used to compare differences between groups (C and D). A Spearman's rank correlation test was performed to assess the correlation between CT density and W/D ratio (E). For (G–J), a two-way ANOVA was used for statistical analysis followed by Tukey's post hoc test to compare vehicle vs. FXT-001. Multiple-comparison analysis for (J) showed statistically significant differences at 7 h ($p = 0.0092$) and 8 h ($p = 0.0063$), whereas no significant difference was observed at earlier time points. $n = 5$ per group.

See also Figure S5 and Videos S4–S6.

platforms and surrogates for transplantation, ADME/pharmacokinetic studies particularly support the potential of recipient-directed treatment. Finally, because organ injury in clinical transplantation often initiates in the donor prior to procurement, future applications may also explore donor-based administration strategies.

Please cite this article in press as: Veeckmans et al., Ferroptosis inhibition enhances liver and lung graft function, Cell (2026), https://doi.org/10.1016/j.cell.2026.04.024

A

Exp.	Donor type	Reasons for declining	WIT	CIT	Treatment	EVLP
1	DCD III	Moderate COPD	21'	17h	Vehicle	6h
					FXT-001	6h
2	DCD V	Severe COPD	12'	22h	Vehicle	4h
					FXT-001	4h
3	DCD III	Renal cell carcinoma	20'	6h 22'	Vehicle	6h
					FXT-001	6h
4	DBD	Suspicious lung nodulus	/	12h	Vehicle	6h
					FXT-001	6h
5	DBD	Logistical reasons	/	13h	Vehicle	6h
					FXT-001	6h

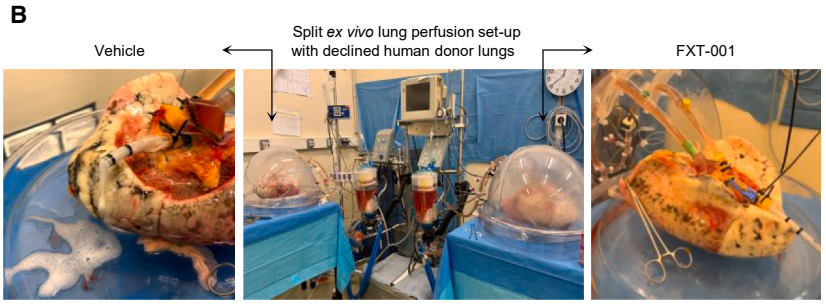

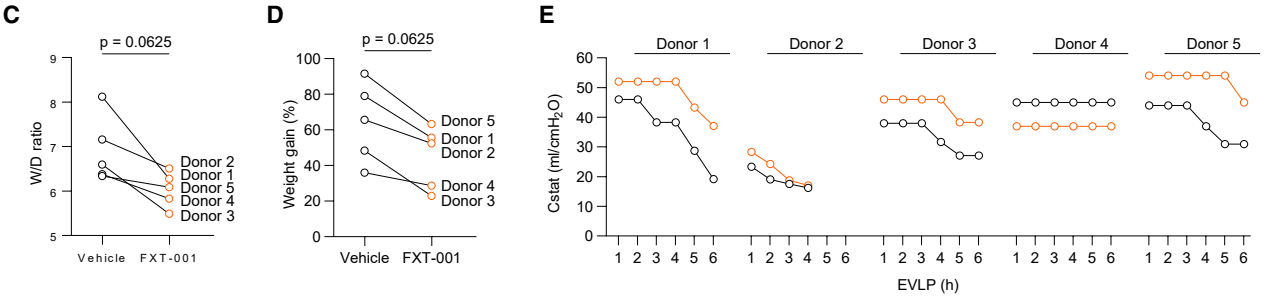

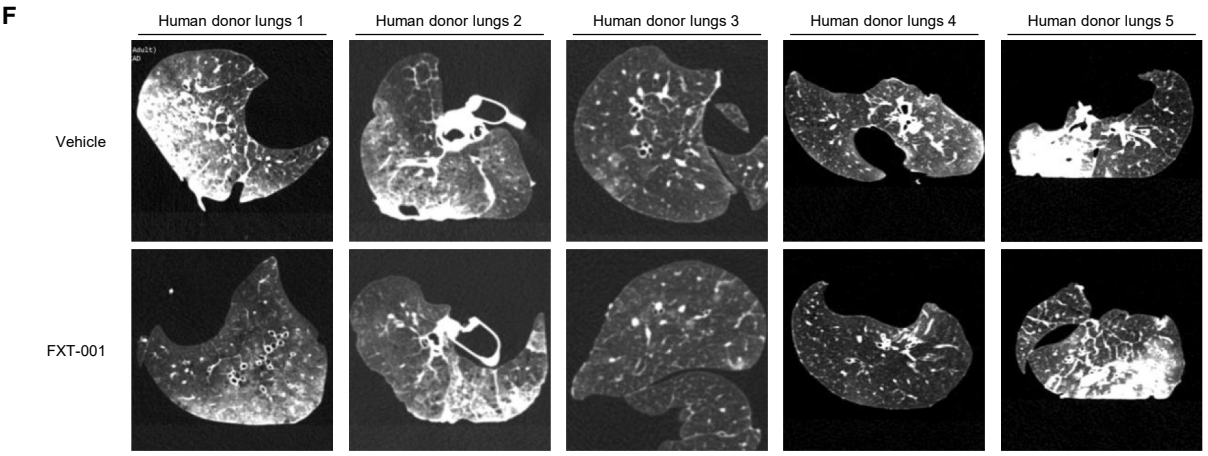

Figure 6. FXT-001 protects human lung grafts during EVLP

(A) Overview of DCD or donation after brain death (DBD) donor lungs declined for transplantation, including the corresponding reason for declining the organ, warm ischemia time (WIT), CIT, assigned treatment (vehicle vs. FXT-001) and EVLP duration.

(B) Schematic presentation of the split *ex vivo* perfusion set up with declined human donor lungs.

(C) W/D weight ratios of the right lower lobe.

(D) Lung weight gain (percentage).

(E) Cstat at baseline and up to 6 h of normothermic EVLP. Vehicle-treated donors are shown in black and FXT-001-treated donors in orange.

(F) CT-based images of declined human lungs on EVLP. A Wilcoxon matched-pairs signed rank test was used to compare vehicle vs. FXT-001 (C and D). $n = 1$ per group.

See also Figure S6 and Videos S7 and S8.

Ferroptosis has increasingly been recognized as a potential regulator of immune homeostasis and post-transplantation immune responses.[44,45] In the experimental liver perfusion setting, the observed increase in IL-10 and slightly decreased TGF-β suggest a partially immunosuppressive yet non-fibrotic microenvironment. In porcine lungs, the immune response was attenuated based on IL-6 and IL-8 suppression. The absence of this response in the human lung grafts may be due to severe additional underlying clinical donor injury or the use of an acellular perfusate.

While MDA levels correlated with liver injury in human transplant recipients, they lacked specificity for EAD, which suggested that other cell death pathways likely contribute to graft injury, and that the predictive capacity of this biomarker is mainly limited to the first hours after reperfusion.

Importantly, administration of a ferroptosis inhibitor to human donor lungs on EVLP, across diverse underlying pathologies, reduces extravascular lung water development by approximately 20%. Owing to the limited number of human experiments, these data are descriptive rather than statistically powered.

Nevertheless, given the strong correlation between primary graft dysfunction and short-term post-transplantation morbidity and mortality, interventions that reduce edema formation remain critically important. Overall, the present work provides a proof of concept of the therapeutic potential of FXT-001 in organ preservation by modeling early transplant responses in high-risk organs and evaluating clinically relevant biomarkers for graft suitability.

In conclusion, our findings show that lipid peroxidation peaks within the first hour after transplantation, contributes to transplant-related organ injury, and positions FXT-001 and its analogs as promising lead candidates for clinical translation. FXT-001 is a first-in-class, intravenously administered ferroptosis inhibitor with high aqueous solubility and sufficient half-life designed for protection of peripheral organs during IRI and *ex situ* organ preservation. Beyond transplantation, the implications of ferroptosis inhibitors are far reaching. Any organ or organ system subject to ischemia—from surgical clamping during major operations, to perfusion deficits in stroke, myocardial infarction, general thrombosis, and critical illness—may benefit from targeted ferroptosis blockade at the time of reperfusion. By bridging fundamental insights into ferroptosis biochemistry with preclinical efficacy in large-animal and human tissue models, this work provides a foundation for the therapeutic targeting of ferroptosis across a wide spectrum of ischemic diseases.

Limitations of the study

Although FXT-001 reduced perfusate MDA levels and improved organ function, histopathological injury markers remained largely unchanged in both liver and lung grafts. This may reflect regional heterogeneity of tissue injury or limited sensitivity due to sampling constraints. Additionally, FXT-001 also showed inconsistent modulation of inflammatory cytokines across models, which may indicate that ferroptosis contributes only indirectly to the complex immunobiology of IRI. Finally, while our study did not include *in vivo* graft or recipient survival, these endpoints should be addressed in the first-in-human studies.

RESOURCE AVAILABILITY

Lead contact

Requests for further information and resources should be directed to and will be fulfilled by the lead contact, Tom Vanden Berghe (tom.vandenberghe@uantwerpen.be).

Materials availability

Material generated in this study will be made available on request, but a payment and/or a completed materials transfer agreement may be required.

Data and code availability

MS analysis and NMR spectra data have been deposited in Mendeley Data and are publicly available as of the date of publication (Mendeley Data: 10.17632/n7jbyznw8g.1). This article does not report any original code. Any additional information required to reanalyze the data reported in this article is available from the lead contact upon request.

ACKNOWLEDGMENTS

We thank the VIB Microscopy Core for their dedicated support with imaging and the VIB Metabolomics Core (at KU Leuven) for quantifying FXT-001 delivery in liver grafts. We are grateful to Erik Fransen for his insightful feedback on statistical analyses and An Vermeulen for PK expert advice. We also thank Herald Berghmans, Francesca Barbieri, Geert Dams, and Hilde Geryl for their excellent technical and experimental assistance, as well as Emily Van San and Cédric Peleman for their valuable contributions. We acknowledge Tine Wylin and Veerle Heedfeld for their critical support in organizing and conducting the porcine liver experiments and the student researchers of the KU Leuven Transplantation Research Group for their help with sample collection during the animal and clinical studies. For lung experiments, we are grateful to Mr. Walter Coudyzer for assistance with the CT imaging of frozen lungs. We also thank Professor Louis Libbrecht (Department of Pathology, AZ Groeninge, and Lab of Hepatology, KU Leuven) for his expert histopathological assessment of liver injury and Claire Evers for her support in obtaining ethical approvals. We acknowledge EuroCC Belgium and LUMI-BE for awarding this project access to the LUMI supercomputer, which is owned by the EuroHPC Joint Undertaking and hosted by CSC (Finland) and the LUMI consortium. In terms of financial support, the J.P., I.J., K.A., D.M., A.N., and T.V.B. labs are supported by the Fund for Scientific Research (FWO) Flanders (SBO, S001522N). The T.V.B. and K.A. labs are further supported by Excellence of Science CD-INFLADIS and Consortium of Excellence at the University of Antwerp INFLA-MED. The T.V.B. lab is additionally supported by the Industrial Research Fund, the Foundation against cancer (F/2022/2067), VLAIO Baekeland, and BOF-IMPULS from the University of Antwerp. The K.A. lab has received funding from the European Union's Horizon 2020 research and innovation program under the Marie Skłodowska-Curie grant agreements no. 765608 (IT-DED3) and no. 101065370 (NeuroFerro) and from the University of Antwerp, SEP-BOF grant no. 44874. G.V. received funding from the Fund for Scientific Research (FWO) Flanders (1SH9524N). N.G. is supported by a Postdoctoral Clinical Master Specialist Fellowship by the Fund for Scientific Research (FRS – FNRS, 1R00424F). I.J. is a senior clinical investigator of the Research Foundation Flanders (FWO: 1800126N). D.M. is senior clinical investigator at FWO. The M.F. lab is supported by "Sonderzuweisung zur Unterstützung profilbestimmender Struktureinheiten" by the SMWK to Technical University Dresden; TG70 by Sächsische Aufbaubank and SMWK, a measure that is co-financed with tax funds on the basis of the budget passed by the Saxon state parliament (to M.F.); Deutsche Forschungsgemeinschaft (FE 1236/5-1 and FE 1236/8-1 to M.F.); and Bundesministerium für Bildung und Forschung (031L0315A, DEEP_HCC and 01EJ2205A, FERROPath to M.F.).

AUTHOR CONTRIBUTIONS

I.J., K.A., N.G., D.M., A.N., L.J.C., and T.V.B. contributed to the conceptualization and design of this research; G.V., L.D., N.G., D.V.B., C.S., J.B., M. Walravens, M. Wölk, G.K., S.M., C.L., L.C., C.G., and B.H. performed experiments and data collection; L.D., M.L., M.B., J.-M.A., B.R., I.J., and D.M. dealt with baboon or patient plasma and data collection; H.D.W. was involved with software and formal analysis; G.V., L.D., N.G., D.V.B., C.S., C.G., K.A., and T.V.B. drafted the manuscript and prepared figures; G.V., L.D., N.G., D.V.B., C.S., J.B., M. Walravens, G.K., M. Wölk, S.M., C.L., L.C., B.H., R.R., M.L., M.B., J.-M.A., B.R., H.D.W., M.F., J.P., L.J.C., I.J., K.A., D.M., A.N., and T.V.B. revised and approved the final version of the manuscript.

DECLARATION OF INTERESTS

T.V.B., C.S., B.H., G.K., C.L., and K.A. hold patents related to ferroptosis inhibitors. T.V.B. and K.A. are founders of FiriX Therapeutics.

STAR★METHODS

Detailed methods are provided in the online version of this paper and include the following:

- KEY RESOURCES TABLE
- EXPERIMENTAL MODEL AND STUDY PARTICIPANT DETAILS
  - For *in vivo* animal studies
  - For studies involving human participants
- METHOD DETAILS
  - Adsorption, Distribution, Metabolism and Excretion (ADME) and safety–toxicity studies

SUPPLEMENTAL INFORMATION

Supplemental information can be found online at https://doi.org/10.1016/j.cell.2026.04.024.

Received: July 24, 2025
Revised: October 23, 2025
Accepted: April 10, 2026

REFERENCES

1. Eltzschig, H.K., and Eckle, T. (2011). Ischemia and reperfusion–from mechanism to translation. Nat. Med. *17*, 1391–1401. https://doi.org/10.1038/nm.2507.
2. Dixon, S.J., Lemberg, K.M., Lamprecht, M.R., Skouta, R., Zaitsev, E.M., Gleason, C.E., Patel, D.N., Bauer, A.J., Cantley, A.M., Yang, W.S., et al. (2012). Ferroptosis: an iron-dependent form of nonapoptotic cell death. Cell *149*, 1060–1072. https://doi.org/10.1016/j.cell.2012.03.042.
3. Jiang, X., Stockwell, B.R., and Conrad, M. (2021). Ferroptosis: mechanisms, biology and role in disease. Nat. Rev. Mol. Cell Biol. *22*, 266–282. https://doi.org/10.1038/s41580-020-00324-8.
4. Van Coillie, S., Van San, E., Goetschalckx, I., Wiernicki, B., Mukhopadhyay, B., Tonnus, W., Choi, S.M., Roelandt, R., Dumitrascu, C., Lamberts, L., et al. (2022). Targeting ferroptosis protects against experimental (multi)organ dysfunction and death. Nat. Commun. *13*, 1046. https://doi.org/10.1038/s41467-022-28718-6.
5. Hassannia, B., Wiernicki, B., Ingold, I., Qu, F., Van Herck, S., Tyurina, Y.Y., Bayır, H., Abhari, B.A., Angeli, J.P.F., Choi, S.M., et al. (2018). Nano-targeted induction of dual ferroptotic mechanisms eradicates high-risk neuroblastoma. J. Clin. Investig. *128*, 3341–3355. https://doi.org/10.1172/JCI99032.
6. Scarpellini, C., Klejborowska, G., Lanthier, C., Hassannia, B., Vanden Berghe, T., and Augustyns, K. (2023). Beyond ferrostatin-1: a comprehensive review of ferroptosis inhibitors. Trends Pharmacol. Sci. *44*, 902–916. https://doi.org/10.1016/j.tips.2023.08.012.
7. Devos, L., Dubois, A., Fieuws, S., Vanden Berghe, T., Pirenne, J., Ceulemans, L.J., Monbaliu, D., and Jochmans, I. (2025). The Efficacy of Ferroptosis Inhibition on Ischemia-Reperfusion Injury of Abdominal Organs: A Systematic Review and Meta-analysis. Transplantation *109*, e539–e553. https://doi.org/10.1097/TP.0000000000005405.
8. Friedmann Angeli, J.P., Schneider, M., Proneth, B., Tyurina, Y.Y., Tyurin, V.A., Hammond, V.J., Herbach, N., Aichler, M., Walch, A., Eggenhofer, E., et al. (2014). Inactivation of the ferroptosis regulator Gpx4 triggers acute renal failure in mice. Nat. Cell Biol. *16*, 1180–1191. https://doi.org/10.1038/ncb3064.
9. Devisscher, L., Van Coillie, S., Hofmans, S., Van Rompaey, D., Goossens, K., Meul, E., Maes, L., De Winter, H., Van Der Veken, P., Vandenabeele, P., et al. (2018). Discovery of Novel, Drug-Like Ferroptosis Inhibitors with in Vivo Efficacy. J. Med. Chem. *61*, 10126–10140. https://doi.org/10.1021/acs.jmedchem.8b01299.
10. Yamada, N., Karasawa, T., Wakiya, T., Sadatomo, A., Ito, H., Kamata, R., Watanabe, S., Komada, T., Kimura, H., Sanada, Y., et al. (2020). Iron overload as a risk factor for hepatic ischemia-reperfusion injury in liver transplantation: Potential role of ferroptosis. Am. J. Transplant. *20*, 1606–1618. https://doi.org/10.1111/ajt.15773.
11. Mishima, E., Ito, J., Wu, Z., Nakamura, T., Wahida, A., Doll, S., Tonnus, W., Nepachalovich, P., Eggenhofer, E., Aldrovandi, M., et al. (2022). A non-canonical vitamin K cycle is a potent ferroptosis suppressor. Nature *608*, 778–783. https://doi.org/10.1038/s41586-022-05022-3.
12. Linkermann, A., Skouta, R., Himmerkus, N., Mulay, S.R., Dewitz, C., De Zen, F., Prokai, A., Zuchtriegel, G., Krombach, F., Welz, P.S., et al. (2014). Synchronized renal tubular cell death involves ferroptosis. Proc. Natl. Acad. Sci. USA *111*, 16836–16841. https://doi.org/10.1073/pnas.1415518111.
13. Li, W., Feng, G., Gauthier, J.M., Lokshina, I., Higashikubo, R., Evans, S., Liu, X., Hassan, A., Tanaka, S., Cicka, M., et al. (2019). Ferroptotic cell death and TLR4/Trif signaling initiate neutrophil recruitment after heart transplantation. J. Clin. Investig. *129*, 2293–2304. https://doi.org/10.1172/JCI126428.
14. Li, R.L., Fan, C.H., Gong, S.Y., and Kang, S. (2021). Effect and Mechanism of LRP6 on Cardiac Myocyte Ferroptosis in Myocardial Infarction. Oxid. Med. Cell. Longev. *2021*, 8963987. https://doi.org/10.1155/2021/8963987.
15. Gao, M., Monian, P., Quadri, N., Ramasamy, R., and Jiang, X. (2015). Glutaminolysis and Transferrin Regulate Ferroptosis. Mol. Cell *59*, 298–308. https://doi.org/10.1016/j.molcel.2015.06.011.
16. Li, Y., Feng, D., Wang, Z., Zhao, Y., Sun, R., Tian, D., Liu, D., Zhang, F., Ning, S., Yao, J., et al. (2019). Ischemia-induced ACSL4 activation contributes to ferroptosis-mediated tissue injury in intestinal ischemia/reperfusion. Cell Death Differ. *26*, 2284–2299. https://doi.org/10.1038/s41418-019-0299-4.
17. Bruni, A., Pepper, A.R., Pawlick, R.L., Gala-Lopez, B., Gamble, A.F., Kin, T., Seeberger, K., Korbutt, G.S., Bornstein, S.R., Linkermann, A., et al. (2018). Ferroptosis-inducing agents compromise in vitro human islet viability and function. Cell Death Dis. *9*, 595. https://doi.org/10.1038/s41419-018-0506-0.
18. Liu, Y., Zheng, Y., Karatas, H., Wang, X., Foerch, C., Lo, E.H., and van Leyen, K. (2017). 12/15-Lipoxygenase Inhibition or Knockout Reduces Warfarin-Associated Hemorrhagic Transformation After Experimental Stroke. Stroke *48*, 445–451. https://doi.org/10.1161/STROKEAHA.116.014790.

19. Cui, Y., Zhang, Y., Zhao, X., Shao, L., Liu, G., Sun, C., Xu, R., and Zhang, Z. (2021). ACSL4 exacerbates ischemic stroke by promoting ferroptosis-induced brain injury and neuroinflammation. Brain Behav. Immun. *93*, 312–321. https://doi.org/10.1016/j.bbi.2021.01.003.

20. Tuo, Q.Z., Lei, P., Jackman, K.A., Li, X.L., Xiong, H., Li, X.L., Liuyang, Z.Y., Roisman, L., Zhang, S.T., Ayton, S., et al. (2017). Tau-mediated iron export prevents ferroptotic damage after ischemic stroke. Mol. Psychiatry *22*, 1520–1530. https://doi.org/10.1038/mp.2017.171.

21. Lorente, L., Rodriguez, S.T., Sanz, P., Abreu-González, P., Díaz, D., Moreno, A.M., Borja, E., Martín, M.M., Jiménez, A., and Barrera, M.A. (2016). Association between Pre-Transplant Serum Malondialdehyde Levels and Survival One Year after Liver Transplantation for Hepatocellular Carcinoma. Int. J. Mol. Sci. *17*, 500. https://doi.org/10.3390/ijms17040500.

22. Nasralla, D., Coussios, C.C., Mergental, H., Akhtar, M.Z., Butler, A.J., Ceresa, C.D.L., Chiocchia, V., Dutton, S.J., García-Valdecasas, J.C., Heaton, N., et al. (2018). A randomized trial of normothermic preservation in liver transplantation. Nature *557*, 50–56. https://doi.org/10.1038/s41586-018-0047-9.

23. Bauch, C., Bevan, S., Woodhouse, H., Dilworth, C., and Walker, P. (2015). Predicting in vivo phospholipidosis-inducing potential of drugs by a combined high content screening and in silico modelling approach. Toxicol. In Vitro *29*, 621–630. https://doi.org/10.1016/j.tiv.2015.01.014.

24. Cañeque, T., Müller, S., and Rodriguez, R. (2018). Visualizing biologically active small molecules in cells using click chemistry. Nat. Rev. Chem. *2*, 202–215. https://doi.org/10.1038/s41570-018-0030-x.

25. Sassano, M.L., Tyurina, Y.Y., Diokmetzidou, A., Vervoort, E., Tyurin, V.A., More, S., La Rovere, R., Giordano, F., Bultynck, G., Pavie, B., et al. (2025). Endoplasmic reticulum-mitochondria contacts are prime hotspots of phospholipid peroxidation driving ferroptosis. Nat. Cell Biol. *27*, 902–917. https://doi.org/10.1038/s41556-025-01668-z.

26. Renovitch, G.A., and Baker, W.A. (1969). Complexes of iron with o-phenylenediamine. J. Chem. Soc. A *75–78*, 75. https://doi.org/10.1039/J19690000075.

27. Helberg, J., and Pratt, D.A. (2021). Autoxidation vs. antioxidants – the fight for forever. Chem. Soc. Rev. *50*, 7343–7358. https://doi.org/10.1039/D1CS00265A.

28. Petrat, F., Weisheit, D., Lensen, M., De Groot, H., Sustmann, R., and Rauen, U. (2002). Selective determination of mitochondrial chelatable iron in viable cells with a new fluorescent sensor. Biochem. J. *362*, 137–147. https://doi.org/10.1042/0264-6021:3620137.

29. Niwa, M., Hirayama, T., Okuda, K., and Nagasawa, H. (2014). A new class of high-contrast Fe(II) selective fluorescent probes based on spirocyclized scaffolds for visualization of intracellular labile iron delivered by transferrin. Org. Biomol. Chem. *12*, 6590–6597. https://doi.org/10.1039/c4ob00935e.

30. Gilbo, N., Blondeel, J., Wylin, T., Heedfeld, V., Jochmans, I., Pirenne, J., Korf, H., and Monbaliu, D. (2024). The dynamics of cytokine release during 24 hours continuous normothermic machine perfusion liver preservation: An explorative porcine study. Artif. Organs *48*, 606–618. https://doi.org/10.1111/aor.14717.

31. Jochmans, I., Meurisse, N., Neyrinck, A., Verhaegen, M., Monbaliu, D., and Pirenne, J. (2017). Hepatic ischemia/reperfusion injury associates with acute kidney injury in liver transplantation: Prospective cohort study. Liver Transpl. *23*, 634–644. https://doi.org/10.1002/lt.24728.

32. Meurisse, N., Mertens, M., Fieuws, S., Gilbo, N., Jochmans, I., Pirenne, J., and Monbaliu, D. (2023). Effect of a Combined Drug Approach on the Severity of Ischemia-Reperfusion Injury During Liver Transplant: A Randomized Clinical Trial. JAMA Netw. Open *6*, e230819. https://doi.org/10.1001/jamanetworkopen.2023.0819.

33. Olthoff, K.M., Kulik, L., Samstein, B., Kaminski, M., Abecassis, M., Emond, J., Shaked, A., and Christie, J.D. (2010). Validation of a current definition of early allograft dysfunction in liver transplant recipients and analysis of risk factors. Liver Transpl. *16*, 943–949. https://doi.org/10.1002/lt.22091.

34. Längin, M., Mayr, T., Reichart, B., Michel, S., Buchholz, S., Guethoff, S., Dashkevich, A., Baehr, A., Egerer, S., Bauer, A., et al. (2018). Consistent success in life-supporting porcine cardiac xenotransplantation. Nature *564*, 430–433. https://doi.org/10.1038/s41586-018-0765-z.

35. Längin, M., Reichart, B., Steen, S., Sjöberg, T., Paskevicius, A., Liao, Q., Qin, G., Mokelke, M., Mayr, T., Radan, J., et al. (2020). Cold non-ischemic heart preservation with continuous perfusion prevents early graft failure in orthotopic pig-to-baboon xenotransplantation. Xenotransplantation *28*, e12636. https://doi.org/10.1111/xen.12636.

36. Gao, M., Yi, J., Zhu, J., Minikes, A.M., Monian, P., Thompson, C.B., and Jiang, X. (2019). Role of Mitochondria in Ferroptosis. Mol. Cell *73*, 354–363.e3. https://doi.org/10.1016/j.molcel.2018.10.042.

37. Kagan, V.E., Mao, G., Qu, F., Angeli, J.P.F., Doll, S., Croix, C.S., Dar, H.H., Liu, B., Tyurin, V.A., Ritov, V.B., et al. (2017). Oxidized arachidonic and adrenic PEs navigate cells to ferroptosis. Nat. Chem. Biol. *13*, 81–90. https://doi.org/10.1038/nchembio.2238.

38. von Krusenstiern, A.N., Robson, R.N., Qian, N., Qiu, B., Hu, F., Reznik, E., Smith, N., Zandkarimi, F., Estes, V.M., Dupont, M., et al. (2023). Identification of essential sites of lipid peroxidation in ferroptosis. Nat. Chem. Biol. *19*, 719–730. https://doi.org/10.1038/s41589-022-01249-3.

39. Cañeque, T., Baron, L., Müller, S., Carmona, A., Colombeau, L., Versini, A., Solier, S., Gaillet, C., Sindikubwabo, F., Sampaio, J.L., et al. (2025). Activation of lysosomal iron triggers ferroptosis in cancer. Nature *642*, 492–500. https://doi.org/10.1038/s41586-025-08974-4.

40. Rizzollo, F., Escamilla-Ayala, A., Fattorelli, N., Lysiak, N.B., More, S., Hernández Varas, P., Barazzuol, L., Van den Haute, C., Van Asselberghs, J., Nittner, D., et al. (2025). BDH2-driven lysosome-to-mitochondria iron transfer shapes ferroptosis vulnerability of the melanoma cell states. Nat. Metab. *7*, 1851–1870. https://doi.org/10.1038/s42255-025-01352-4.

41. Mai, T.T., Hamaï, A., Hienzsch, A., Cañeque, T., Müller, S., Wicinski, J., Cabaud, O., Leroy, C., David, A., Acevedo, V., et al. (2017). Salinomycin kills cancer stem cells by sequestering iron in lysosomes. Nat. Chem. *9*, 1025–1033. https://doi.org/10.1038/nchem.2778.

42. Reasor, M.J., Hastings, K.L., and Ulrich, R.G. (2006). Drug-induced phospholipidosis: issues and future directions. Expert Opin. Drug Saf. *5*, 567–583. https://doi.org/10.1517/14740338.5.4.567.

43. Watson, C.J.E., and Jochmans, I. (2018). From "Gut Feeling" to Objectivity: Machine Preservation of the Liver as a Tool to Assess Organ Viability. Curr. Transplant. Rep. *5*, 72–81. https://doi.org/10.1007/s40472-018-0178-9.

44. Bell, H.N., Stockwell, B.R., and Zou, W. (2024). Ironing out the role of ferroptosis in immunity. Immunity *57*, 941–956. https://doi.org/10.1016/j.immuni.2024.03.019.

45. Bai, Y.Z., Kopecky, B.J., Lavine, K.J., and Kreisel, D. (2023). Ferroptosis in the post-transplantation inflammatory response. Cell. Immunol. *393–394*, 104774. https://doi.org/10.1016/j.cellimm.2023.104774.

46. Gilbo, N., Jacquemin, M., Nasralla, D., Lazzaro, S., Libbrecht, L., Lavend'homme, R., Peerlinck, K., Ploeg, R.J., Friend, P.J., Pirenne, J., et al. (2022). Coagulation Factors Accumulate During Normothermic Liver Machine Perfusion Regardless of Donor Type and Severity of Ischemic Injury. Transplantation *106*, 510–518. https://doi.org/10.1097/tp.0000000000003763.

47. Percie du Sert, N., Hurst, V., Ahluwalia, A., Alam, S., Avey, M.T., Baker, M., Browne, W.J., Clark, A., Cuthill, I.C., Dirnagl, U., et al. (2020). The ARRIVE guidelines 2.0: Updated guidelines for reporting animal research. PLoS Biol. *18*, e3000410. https://doi.org/10.1371/journal.pbio.3000410.

48. Kilkenny, C., Browne, W.J., Cuthill, I.C., Emerson, M., and Altman, D.G. (2010). Improving bioscience research reporting: the ARRIVE guidelines for reporting animal research. PLoS Biol. *8*, e1000412. https://doi.org/10.1371/journal.pbio.1000412.

49. Blondeel, J., Gilbo, N., Wylin, T., Heedfeld, V., and Monbaliu, D. (2023). Porcine Normothermic Isolated Liver Perfusion. J. Vis. Exp. https://doi.org/10.3791/65336.

50. Liu, C., Ma, J., Zhang, J., Zhao, H., Zhu, Y., Qi, J., Liu, L., Zhu, L., Jiang, Y., Tang, G., et al. (2019). Testosterone Deficiency Caused by Castration Modulates Mitochondrial Biogenesis Through the AR/PGC1α/TFAM Pathway. Front. Genet. *10*, 505. https://doi.org/10.3389/fgene.2019.00505.

51. Chacon-Alberty, L., Ye, S., Daoud, D., Frankel, W.C., Virk, H., Mase, J., Hochman-Mendez, C., Li, M., Sampaio, L.C., Taylor, D.A., et al. (2021). Analysis of sex-based differences in clinical and molecular responses to ischemia reperfusion after lung transplantation. Respir. Res. *22*, 318. https://doi.org/10.1186/s12931-021-01900-y.

52. Li, B., Harjani, J.R., Cormier, N.S., Madarati, H., Atkinson, J., Cosa, G., and Pratt, D.A. (2013). Besting Vitamin E: Sidechain Substitution is Key to the Reactivity of Naphthyridinol Antioxidants in Lipid Bilayers. J. Am. Chem. Soc. *135*, 1394–1405. https://doi.org/10.1021/ja309153x.

53. Shah, R., Farmer, L.A., Zilka, O., Van Kessel, A.T.M., and Pratt, D.A. (2019). Beyond DPPH: Use of Fluorescence-Enabled Inhibited Autoxidation to Predict Oxidative Cell Death Rescue. Cell Chem. Biol. *26*, 1594–1607.e7. https://doi.org/10.1016/j.chembiol.2019.09.007.

54. Ingold, K.U. (1961). Inhibition of the Autoxidation of Organic Substances in the Liquid Phase. Chem. Rev. *61*, 563–589. https://doi.org/10.1021/cr60214a002.

55. Gérard-Monnier, D., Erdelmeier, I., Régnard, K., Moze-Henry, N., Yadan, J.C., and Chaudière, J. (1998). Reactions of 1-Methyl-2-phenylindole with Malondialdehyde and 4-Hydroxyalkenals. Analytical Applications to a Colorimetric Assay of Lipid Peroxidation. Chem. Res. Toxicol. *11*, 1176–1183. https://doi.org/10.1021/tx9701790.

56. Folch, J., Lees, M., and Sloane Stanley, G.H. (1957). A simple method for the isolation and purification of total lipides from animal tissues. J. Biol. Chem. *226*, 497–509. https://doi.org/10.1016/S0021-9258(18)64849-5.

57. Ni, Z., Angelidou, G., Hoffmann, R., and Fedorova, M. (2017). LPPtiger software for lipidome-specific prediction and identification of oxidized phospholipids from LC-MS datasets. Sci. Rep. *7*, 15138. https://doi.org/10.1038/s41598-017-15363-z.

58. Adams, K.J., Pratt, B., Bose, N., Dubois, L.G., St John-Williams, L., Perrott, K.M., Ky, K., Kapahi, P., Sharma, V., MacCoss, M.J., et al. (2020). Skyline for Small Molecules: A Unifying Software Package for Quantitative Metabolomics. J. Proteome Res. *19*, 1447–1458. https://doi.org/10.1021/acs.jproteome.9b00640.

59. MacLean, B., Tomazela, D.M., Shulman, N., Chambers, M., Finney, G.L., Frewen, B., Kern, R., Tabb, D.L., Liebler, D.C., and MacCoss, M.J. (2010). Skyline: an open source document editor for creating and analyzing targeted proteomics experiments. Bioinformatics *26*, 966–968. https://doi.org/10.1093/bioinformatics/btq054.

60. Chong, J., Soufan, O., Li, C., Caraus, I., Li, S., Bourque, G., Wishart, D.S., and Xia, J. (2018). MetaboAnalyst 4.0: towards more transparent and integrative metabolomics analysis. Nucleic Acids Res. *46*, W486–W494. https://doi.org/10.1093/nar/gky310.

61. Schott-Verdugo, S., and Gohlke, H. (2019). PACKMOL-Memgen: A Simple-To-Use, Generalized Workflow for Membrane-Protein–Lipid-Bilayer System Building. J. Chem. Inf. Model. *59*, 2522–2528. https://doi.org/10.1021/acs.jcim.9b00269.

62. Case, D.A., Aktulga, H.M., Belfon, K., Cerutti, D.S., Cisneros, G.A., Cruzeiro, V.W.D., Forouzesh, N., Giese, T.J., Götz, A.W., Gohlke, H., et al. (2023). AmberTools. J. Chem. Inf. Model. *63*, 6183–6191. https://doi.org/10.1021/acs.jcim.3c01153.

63. Jorgensen, W.L., Chandrasekhar, J., Madura, J.D., Impey, R.W., and Klein, M.L. (1983). Comparison of simple potential functions for simulating liquid water. J. Chem. Phys. *79*, 926–935. https://doi.org/10.1063/1.445869.

64. Dickson, C.J., Walker, R.C., and Gould, I.R. (2022). Lipid21: Complex Lipid Membrane Simulations with AMBER. J. Chem. Theory Comput. *18*, 1726–1736. https://doi.org/10.1021/acs.jctc.1c01217.

65. Vassetti, D., Pagliai, M., and Procacci, P. (2019). Assessment of GAFF2 and OPLS-AA General Force Fields in Combination with the Water Models TIP3P, SPCE, and OPC3 for the Solvation Free Energy of Druglike Organic Molecules. J. Chem. Theory Comput. *15*, 1983–1995. https://doi.org/10.1021/acs.jctc.8b01039.

66. Wang, J., Wang, W., Kollman, P.A., and Case, D.A. (2006). Automatic atom type and bond type perception in molecular mechanical calculations. J. Mol. Graph. Model. *25*, 247–260. https://doi.org/10.1016/j.jmgm.2005.12.005.

67. Jakalian, A., Bush, B.L., Jack, D.B., and Bayly, C.I. (2000). Fast, efficient generation of high-quality atomic charges. AM1-BCC model: I. Method. J. Comput. Chem. *21*, 132–146. https://doi.org/10.1002/(SICI)1096-987X(20000130)21:2<132::AID-JCC5>3.0.CO;2-P.

68. Lee, C.T., Comer, J., Herndon, C., Leung, N., Pavlova, A., Swift, R.V., Tung, C., Rowley, C.N., Amaro, R.E., Chipot, C., et al. (2016). Simulation-Based Approaches for Determining Membrane Permeability of Small Compounds. J. Chem. Inf. Model. *56*, 721–733. https://doi.org/10.1021/acs.jcim.6b00022.

69. Faulkner, C., and de Leeuw, N.H. (2021). Predicting the Membrane Permeability of Fentanyl and Its Analogues by Molecular Dynamics Simulations. J. Phys. Chem. B *125*, 8443–8449. https://doi.org/10.1021/acs.jpcb.1c05438.

70. Grossfield, A. WHAM: the weighted histogram analysis method. Version WHAM-release-2.1.0. http://membrane.urmc.rochester.edu/content/wham/.

71. Kumar, S., Rosenberg, J.M., Bouzida, D., Swendsen, R.H., and Kollman, P.A. (1995). Multidimensional free-energy calculations using the weighted histogram analysis method. J. Comput. Chem. *16*, 1339–1350. https://doi.org/10.1002/jcc.540161104.

72. Gilbo, N., Wylin, T., Heedfeld, V., Jochmans, I., Pirenne, J., Friend, P., and Monbaliu, D. (2022). Porcine Liver Normothermic Machine Perfusion: Methodological Framework and Potential Pitfalls. Transplant. Direct *8*, e1276. https://doi.org/10.1097/txd.0000000000001276.

73. Devos, L.W.T. (2025). Protocol - 4-HNE immunofluorescence staining. Protocols.io.

74. Decuypere, J.P., Hutchinson, S., Monbaliu, D., Martinet, W., Pirenne, J., and Jochmans, I. (2020). Autophagy Dynamics and Modulation in a Rat Model of Renal Ischemia-Reperfusion Injury. Int. J. Mol. Sci. *21*, 7185. https://doi.org/10.3390/ijms21197185.

Please cite this article in press as: Veeckmans et al., Ferroptosis inhibition enhances liver and lung graft function, Cell (2026), https://doi.org/10.1016/j.cell.2026.04.024

CellPress
OPEN ACCESS

STAR★METHODS

KEY RESOURCES TABLE

REAGENT or RESOURCE	SOURCE	IDENTIFIER
Antibodies		
Mouse mAb Cytochrome c (6H2.B4)	Cell Signaling Technology	Cat.#12963; RRID:AB_2637072
Rabbit mAb RCAS1 (D2B6N) XP	Cell Signaling Technology	Cat.#12290; RRID:AB_2736985
Rabbit mAb LAMP1 (D2D11) XP	Cell Signaling Technology	Cat.#9091; RRID:AB_2687579
Mouse mAb Anti-PDIA3 (CL2444)	Sigma Aldrich	Cat# AMAb90988; RRID:AB_2665750
Alexa Fluor 647 Goat anti-mouse	Invitrogen	Cat#A21237; RRID:AB_1500743
Alexa Fluor 647 Goat anti-rabbit	Invitrogen	Cat# A21246; RRID:AB_1500778
Goat anti-mouse IgG Alexa Fluor 635 conjugated	Thermo Fisher Scientific	Cat# A31574; RRID:AB_1500640
Donkey anti-rabbit IgG (H+L) polyclonal antibody, Alexa Fluor 555 conjugated	Thermo Fisher Scientific	Cat# A-31572; RRID:AB_162543
Rabbit Polyclonal 4-Hydroxynonenal antibody	Abcam	Cat.# ab46545; RRID: AB_722490
Goat anti-Rabbit IgG (H+L) Cross-Adsorbed Secondary Antibody, Alexa Fluor™ 488	Thermo Fisher Scientific	Cat.# A-11008; RRID: AB_143165
Goat GPX4 Polyclonal Antibody	MyBioSource	Cat.# MBS420590; RRID:AB_2112421
Biological samples		
Human plasma samples from liver transplant patients (KILT study)	University hospitals in Leuven, Belgium	PubMed: PMID: 28124458, clinicaltrials.gov: NCT01333319 & CTC reference number: s53174
Human plasma samples from liver transplant patients (CAPITL Study)	University hospitals in Leuven, Belgium	PubMed: PMID: 36853611, clinicaltrials.gov: NCT02251041 & CTC reference number: s54348
Human lung grafts declined for transplantation for too low quality	University hospitals in Leuven, Belgium	N/A
Chemicals, peptides, and recombinant proteins		
FXT-001	The medicinal chemistry laboratory, University of Antwerp	PubMed: PMID: 30354101, CAS Number: 2271358-64-4, PubChem CID number: 137701965
FXT-002	This paper	N/A
FXT-003	The medicinal chemistry research, University of Antwerp	Patent/Reference: WO2024062043, PubChem CID number: 171100465
L_1FXT-001	This paper	N/A
L_2FXT-001	This paper	N/A
RFXT-001	This paper	N/A
C_1FXT-001	This paper	N/A
ML162	Selleckchem	Cat.#S4452
Sytox Green	Thermo Fisher Scientific	Cat.#10768273
iron(II) sulfate heptahydrate ($FeSO_4.7H_2O$)	Sigma Aldrich	Cat.#F7002-250G-D
1-Methyl 2-phenylindole	Sigma Aldrich	Cat.# 404888
1,1,3,3-tetramethoxypropane	Sigma-Aldrich	Cat.#108383
Sytox Green	Fisher Scientific	Cat.#10768273
IGL-1®	Institute George Lopez, Lissieu, France	REF: IGL-1/1000
Geloplasma®	Fresenius Kabi, Schelle, Belgium	Cat.#247429
Heparin	Leo Pharmaceutical products, Denmark	Cat.#BR-1005

(*Continued on next page*)

Please cite this article in press as: Veeckmans et al., Ferroptosis inhibition enhances liver and lung graft function, Cell (2026), https://doi.org/10.1016/j.cell.2026.04.024

Continued

REAGENT or RESOURCE	SOURCE	IDENTIFIER
Calcium gluconate	Braun Medical SA, Melsungen, Germany	Cat.#570/13596667/1214
Sodium bicarbonate	Braun Medical SA, Melsungen, Germany	Cat.#3622339
DAPI	ThermoScientific	Cat.#62248
Steen Solution™	Xvivo (Perfusion AB, Gothenburg, Sweden)	N/A
Perfadex® Plus solution	Xvivo Perfusion AB, Gothenburg, Sweden	N/A
Methanol-d_4	Eurisotop	Cat#D048FD
styrene-conjugated BODIPY (STY-BODIPY)	The medicinal chemistry laboratory, University of Antwerp	Shah et al.[53]
(E)-1,2-bis((2-methyldecan-2-yl)oxy)diazene (DTUN)	The medicinal chemistry laboratory, University of Antwerp	Shah et al.[53]
L-α-phosphatidylcholine (Egg, Chicken),	Merck Life Science B.V.	Cat#P3556
2,2-Diphenyl-1-picrylhydrazyl (DPPH)	Merck Life Science B.V.	Cat#D9132
Critical commercial assays		
Click-iT™ EdU Cell Proliferation Kit for Imaging	Thermo Fisher Scientific	Cat.#C10337
ProcartaPlex Porcine Mix&Match 6-plex (IFN gamma, IL-1 beta, IL-10, IL-6, IL-8 (CXCL8), TNF alpha)	Thermo Fisher Scientific	Cat.#PPX-06-MXEPVRF
ProcartaPlex Human Mix&Match 6-plex (IFN gamma, IL-1 beta, IL-10, IL-6, IL-8 (CXCL8), TNF alpha)	Thermo Fisher Scientific	Cat.#PPX-07-MXDJZ6F
In Situ Cell Death Detection Kit TMR red	Roche	Cat.#12156792910
Mini-PROTEAN TGX gells	Bio-Rad, USA	Cat.#4569036
Transfer Turbo Transfer Pack	Bio-Rad, USA	Cat.#1704156
IL-1b	Bio-Techne Ireland Limited	Cat.#PLB00B
IL-6	LIFE TECHNOLOGIES EUROPE BV	Cat.#ESIL6
IL-8	Bio-Techne Ireland Limited	Cat.#P8000
IL-10	Bio-Techne Ireland Limited	Cat.#P1000
TNF-a	Bio-Techne Ireland Limited	Cat.#PTA00
TGF-b	Bio-Techne Ireland Limited	Cat.#DB100C
Experimental models: Cell lines		
Human fibrosarcoma cell line (HT-1080 cells)	ATCC	CCL-121
Human hepatocellular carcinoma cell line (HepG2 cells)	ATCC	Cyprotex Discovery Limited
Human Embryonic Kidney cell line (HEK293 cells)	ATCC	Cyprotex Discovery Limited
Madin-Darby canine kidney (MDCK) cells	NIH (Rockville, MD, USA)	Cyprotex Discovery Limited
Human lymphoblast (TK6) cells	Cyprotex Discovery Limited	Cyprotex Discovery Limited
Chinese hamster ovary (CHO) cells	Eurofins Cerep	Eurofins Cerep
Human Embryonic Kidney cell line (HEK293 cells)	Eurofins Cerep	Eurofins Cerep
Experimental models: Organisms/strains		
Mouse: C57BL/6NCrl	Charles River laboratories	Strain code: 027
Porcine: TN70	Tojapigs Escharen, Nijmegen, The Netherlands	N/A
Salmonella typhimurium tester strains (TA98, TA100, TA1535 and TA1537)	Eurofins Cerep	Eurofins Cerep
Pooled liver microsomes (Human, Mouse, Rat, Dog, Monkey, Minipig, Rabbit, Guinea Pig)	Cyprotex Discovery Limited	Cyprotex Discovery Limited

(*Continued on next page*)

Please cite this article in press as: Veeckmans et al., Ferroptosis inhibition enhances liver and lung graft function, Cell (2026), https://doi.org/10.1016/j.cell.2026.04.024

Continued

REAGENT or RESOURCE	SOURCE	IDENTIFIER
Deposited data		
NMR spectra: Mestrenova or TopSpin MS analysis: MassLynx	Mendeley Data	Mendeley Data: https://doi.org/10.17632/n7jbyznw8g.1
Software and algorithms		
Fiji	National Institutes of Health	http://fiji.sc; RRID:SCR_002285
Horos DICOM Viewer, version 3 (LGPL-3.0)	Horos Project	https://horosproject.org/download-horos/; RRID:SCR_017340
Collaborative Drug Discovery (CDD) Vault software	CDD Vault	https://www.collaborativedrug.com/; RRID:SCR_025149
Zeiss ZEN Black 2.6 software	ZEISS	RRID:SCR_018163
GraphPad Prism	GraphPad Software	http://www.graphpad.com/; RRID:SCR_002798
Bruker Topspin (v.4.1.4) and (v.4.1.1) software	TopSpin NMR software	RRID:SCR_014227
MestReNova version 14.3.1 or higher	Mestrelab Research	https://mestrelab.com/
Agilent Biotek Gen 5 software	Agilent	https://www.agilent.com/
Jeol Software	Jeol	https://www.jeol.com/products/scientific/nmr_software/Delta5.php
LPPtiger 2.0	Ni et al.[57]	https://github.com/SysMedOs/lpptiger
Skyline v. 23.1	Maclean et al.[59]	https://skyline.ms/project/home/software/Skyline/begin.vie; RRID:SCR_014080
MetaboAnalyst online platform v5.0	Chong et al.[60]	https://www.metaboanalyst.ca/
PACKMOL-Memgen software package	Schott-Verdugo and Gohlke[61]	https://m3g.github.io/packmol/
AMBER 24 software	Case et al.[62]	http://ambermd.org/; RRID:SCR_014230
ChemDraw 23.1.2	Revity Signals	https://revvitysignals.com/products/research/chemdraw
G*Power 3.1.9.7	Heinrich-Heine-Universität Düsseldorf	http://www.gpower.hhu.de/; RRID: SCR_013726
Image Lab software	Bio-Rad, USA	http://www.bio-rad.com/en-us/sku/1709690-image-lab-software; RRID:SCR_014210
BioRender: Scientific Image and Illustration Software	BioRender	https://BioRender.com/8ktzfjh
Other		
High Throughput Thermodynamic Solubility – MS	Cyprotex Discovery Limited	https://www.evotec.com/physicochemical-profiling/solubility-services
LogD Shake Flask	Cyprotex Discovery Limited	https://www.evotec.com/physicochemical-profiling/lipophilicity-services
Plasma Stability	Cyprotex Discovery Limited	https://www.evotec.com/drug-metabolism/plasma-stability
Plasma Protein Binding	Cyprotex Discovery Limited	https://www.evotec.com/physicochemical-profiling/matrix-binding
Microsomal Stability	Cyprotex Discovery Limited	https://www.evotec.com/drug-metabolism/microsomal-stability
Hepatocyte Stability	Cyprotex Discovery Limited	https://www.evotec.com/drug-metabolism/hepatocyte-stability
MDCK-MDR1 Permeability Assay	Cyprotex Discovery Limited	https://www.evotec.com/drug-permeability-and-transporters/mdck-mdr1-permeability

(*Continued on next page*)

Continued

REAGENT or RESOURCE	SOURCE	IDENTIFIER
EC_{50} in HepG2 (cytotoxicity) and mitochondrial toxicity	Cyprotex Discovery Limited	https://www.evotec.com/toxicology/mitochondrial-toxicity
Cardiotoxicity: hERG channel inhibition	Cyprotex Discovery Limited	https://www.evotec.com/cardiotoxicity/herg-safety
hERG Potassium Channel Assay - Qube APC	Eurofins Cerep	https://www.eurofinsdiscovery.com/catalog/cipa-express-herg-potassium-channel-assay-qube-apc-6-conc.-safetyscreen-us/CYL8038QB2DREX
hNav1.5 Sodium Channel Assay (Qube APC)	Eurofins Cerep	https://www.eurofinsdiscovery.com/catalog/cipa-hnav1-5-sodium-channel-assay-qube-apc-1-conc-safetyscreen-us/CYL8004QB2
hCav1.2 (L-type) CiPA Calcium Channel Assay (Qube APC)	Eurofins Cerep	https://www.eurofinsdiscovery.com/catalog/cipa-hcav1.2-l-type-calcium-channel-assay-qube-apc-6-conc.-safetyscreen-us/CYL7051QB2DR
Genotoxicity: Micronucleus test	Cyprotex Discovery Limited	https://www.evotec.com/genotoxicity/in-vitro-micronucleus-test-mnt-flow-cytometry-tk6
Ames fluctuation test	Eurofins Cerep	https://www.eurofinsdiscovery.com/catalog/ames-fluctuation-test-us/G175
Reactive Metabolite Formation (Stable Labelled Glutathione Trapping)	Cyprotex Discovery Limited	https://www.evotec.com/mechanistic-toxicity/reactive-metabolite
Phospholipidosis and Steatosis Assay	Cyprotex Discovery Limited	https://www.evotec.com/mechanistic-toxicity/drug-induced-phospholipidosis-steatosis-assay
Cytochrome P450 (CYP450) Inhibition (Reversible IC_{50})	Cyprotex Discovery Limited	https://www.evotec.com/drug-metabolism/cytochrome-p450-cyp-inhibition-ic50
Off-target Activities (Eurofins Safety Screen 87 Panel)	Eurofins Cerep	https://www.eurofinsdiscovery.com/catalog/safetyscreen87-panel-fr/P342
Cytotoxicity Screening Panel	Cyprotex Discovery Limited	https://www.evotec.com/mechanistic-toxicity/cytotoxicity-screening-panel
In vivo pharmacokinetics	Selvita	https://selvita.com/drug-discovery/small-molecules/expertise-areas/dmpk

EXPERIMENTAL MODEL AND STUDY PARTICIPANT DETAILS

For *in vivo* animal studies

Mice

All experiments were approved by the animal ethics committee of Antwerp University (2022–58). The animal housing within the animal facility of the University of Antwerp adheres to current ethical standards. Mice were group housed in individually ventilated cages maintaining standardized conditions including a 14/10hours light/dark cycle, humidity of 55% and temperature control set at 21°C. Both water and food were provided ad libitum. All experiments were conducted in male C57BL/6N mice (Charles River Laboratories), aged 8–12 weeks. To ensure methodological consistency with the previously validated experimental iron-intoxication model,[4] the same sex and experimental conditions were used in the present study.

Porcine livers

Prepubescent pigs (3 months; male; TN70, Tojapigs Escharen, The Netherlands) were housed at the KU Leuven animal facility in single pens with 12h light-dark cycle and access to food (MPig- H; ssniff, Soest, Germany). Animals were fasted for 12h before surgery with access to tap water. After organ procurement, animals were euthanized by exsanguination and an intravenous bolus of potassium under anaesthesia.[46] Liver studies were approved by the KU Leuven Animal Care Committee (P121/2022) and conducted in accordance with European guidelines. Results are reported following the ARRIVE guidelines.[47,48] Male pigs were used to maintain consistency with the previously optimized model.[49] Prepubescent animals (3 months of age) were selected to minimize confounding by circulating sex hormones.[50]

Please cite this article in press as: Veeckmans et al., Ferroptosis inhibition enhances liver and lung graft function, Cell (2026), https://doi.org/10.1016/j.cell.2026.04.024

Porcine lungs

The experimental porcine study (3 months, domestic male pigs, TN70, Tojapigs Escharen, The Netherlands) was approved by the Ethical Committee for Animal Research KU Leuven (P147/2023). All animals received human care in accordance with the Principles of Laboratory Animal Care, formulated by the National Society for Medical Research and Guide for the Care and Use of Laboratory Animals, prepared by the Institute of Laboratory Animal Resources and published by the National Institutes of Health, USA (NIH Publication No. 86-23, revised 1996). Prepubescent male pigs (3 months of age) were selected to minimize confounding by circulating sex hormones.[51]

Orthotopic pig-to-baboon cardiac xenotransplants

Plasma samples analyzed in this study were derived from a previously published orthotopic pig-to-baboon cardiac xenotransplantation study.[34,35] Briefly, baboon plasma samples (n = 17), obtained before (-7 days) and after (0 hours to day 7) cessation of cardiopulmonary bypass following xenotransplantation, were analyzed for signs of lipid peroxidation using the colorimetric MDA assay.

For studies involving human participants

Liver transplant patients

Two prospective clinical cohort studies (KILT[31] and CAPITL[32]), involving patients undergoing liver transplantation, were conducted at the University hospital in Leuven, Belgium. Both studies received approval from the UZ Leuven Ethical Committee (CTC reference number: s53174 and s54348) and were registered on clinicaltrials.gov with the number NCT01333319 and NCT02251041. The study protocols adhered to the ethical guidelines of the 1975 Declaration of Helsinki. Written informed consent was obtained from all participants once they were listed for transplantation. In summary, clinical data and plasma samples were collected from 80 participants in the KILT study (11/2011 – 05/2014) and 36 participants in the CAPITL study (09/2013 – 02/2018), before and at key points during liver transplantation, with follow-up until postoperative day 5. Only liver transplants included in the placebo control group of the CAPITL study were used for plasma MDA measurement.

Human lung grafts

Human lungs were used to assess the effectiveness of treatment with FXT-001. These lungs were declined for transplantation for too low quality due to underlying (lung) diseases in the organ donor. Lungs were harvested from organ donors whose organs or tissues were allocated to the University Hospitals Leuven, Belgium (local donor network). Both genders were included. Consent for organ donation/organ use agreed with the Belgian Donor Law (1986°), which is an "opt-out" system. This means that every deceased person is a potential organ donor unless formal refusal against organ donation has been registered during life. None of these donors was included into a clinical study.

For cell lines

All cell lines were cultured in a sterile humidified incubator at 37 °C and 5% CO_2. Human fibrosarcoma cell line HT-1080 cells (ATCC, Cat.#CCL-121) were maintained in MEM Alpha medium (22571-020, Thermo fisher Scientific) or Dulbecco's Modified Eagle Medium (DMEM)/ GlutaMAX (Gibco, 61965059) supplemented with 10% fetal bovine serum (A5256701, Thermo Fisher Scientific), 1% penicillin-streptomycin (15140-122, Thermo fisher Scientific), 1% L-glutamine (25030-081, Thermo Fisher Scientific), 1% MEM non-essential amino acid (M7145, Sigma-Aldrich) and 0.4% sodium pyruvate (S8636, Thermo Fisher Scientific). Human glucocorticoid-sensitive pancreatic ductal adenocarcinoma (HPAC) cells were cultured in RPMI/ GlutaMAX (Gibco, 61870-010) supplemented with 10% FBS (Gibco, 10270-106) and penicillin/streptomycin (BioWhittaker/Lonza, DE17-602E). Primary human pancreatic PDAC053T cells were grown in serum-free ductal medium: DMEM/F12 (Gibco, 10565018), supplemented with 0.61g/500mL nicotinamide (Sigma-Aldrich, 3376), 2.5g/500mL glucose (Sigma-Aldrich, G6152), 1:200 ITS+ (Corning, 354352), 1:20 Nu-serum IV (Corning, 355104), 100 ng/ml cholera toxin, 1 μM dexamethasone (Sigma-Aldrich, D4902), 50 nM 3,3',5-triiodo-L-thyronine (Sigma-Aldrich, T6397) and penicillin/streptomycin. Fresh bovine pituitary extract (Gibco, 13028-014, 22.7 ng/mL) and 50 ng/mL animal-free recombinant human EGF (Thermo Fisher Scientific, AF-100-15-1MG) were added to new medium when cells were split or plated. Detailed information about Human Embryonic Kidney (HEK) 293 cells, human hepatocellular carcinoma cells HepG2 and Madin-Darby canine kidney (MDCK) are not available as the experiments were performed under contract by Cyprotex Discovery Limited (Cheshire, UK).

METHOD DETAILS

Adsorption, Distribution, Metabolism and Excretion (ADME) and safety–toxicity studies

cLogP was calculated using CDD Vault software (Collaborative Drug Discovery Inc., Burlingame, California, USA). LC-MS/MS analytical method, High Throughput Aqueous Solubility, Log D, Chemical stability, Plasma stability, Plasma Protein Binding (PPB), Microsomal Stability, Hepatocyte stability, MDCK-MDR1 permeability assay, Cytotoxicity, Mitochondrial Toxicity, Micronucleus test, Reactive Metabolites formation, Phospholipids, Cytochrome P450 inhibition and Cytotoxicity Screening Panel were performed under contract by Cyprotex Discovery Limited (Cheshire, UK) and hERG Channel inhibition were performed under contract by Cyprotex Discovery Limited (Aptuit (Verona) Srl, IT). Ion Channel inhibition and Ames Fluctuation test were performed under contract by Eurofins Discovery Services North America, LLC (St Charles (MO), US) and Off-target Activities was performed under contract by Eurofins Cerep SA (Celle L'Evescault, FR). The specific URLs corresponding to each experiment are provided in the key resources table, and additional data are reported in Methods S1, Data S1, and Table S1.

Cell death assay

To determine IC_{50} values, HT1080 cells were seeded into a 96-well plate at a density of 10,000 cells per well and cultured overnight. Upon reaching approximately 80% confluency, cells were pretreated with 1.7 μM Sytox Green (Thermo Fisher Scientific, cat.#10768273) and 100 nM ML162 (Selleckchem, Cat.#S4452) in triplicate for 1 hour. Subsequently, a ½ concentration dilution of FXT-001 (125nM) or a FXT-analogue was performed. Cells treated only with ML162 were used as 100% cell death reference, while untreated conditions containing vehicle (0.04% DMSO) served as 0% cell death reference. Following treatment, cells were incubated at 37°C, 5% CO_2 for 24 hours. Fluorescence was measured using a FLUOstar Omega fluorescence plate reader (BMG Labtech) at an excitation/emission wavelength of 485/520 nm. The percentage of the cell death was calculated using the formula: ((AVG[compound] - AVG[background]) / (AVG[ML162] - AVG[background])) × 100. Cell death percentages were plotted in GraphPad Prism (v10.6.0), and IC50-values were calculated using a sigmoidal dose-response (variable slope) curve.

Kinetic solubility

A turbidimetric method was used. First, a series of DMSO compound stock solutions were prepared (0.15 - 5 mM) from the stock solution of the compound in DMSO (10 mM). An aliquot of 4μL stock solution was added to 196 μL PBS buffer (pH 7.4). A series of concentrations were prepared (3.13 - 200 μM), including a blank on a 96-well clear microtiter plate. The microtiter plate was shaken for 10 seconds and incubated for 2 hours at 37°C. Turbidity was measured using the UV/vis spectrophotometer Synergy MX, Biotek with Gen5. When there was no turbidity measured at a given concentration the sample was assumed to be dissolved.

Fluorescence-Enabled Inhibited Autoxidation (FENIX)

Unless otherwise stated, laboratory reagent-grade solvents were used. Reagents were obtained from various commercial sources and were used without any prior purification. Egg L-α-phosphatidylcholine (P3556, Merck Life Science B.V.) was used for the synthesis of liposomes suspension following the protocol reported by Li et al.[52] (E)-1,2-*bis*((2-methyldecan-2-yl)oxy)diazene (DTUN) was synthesized following the procedure described by Shah et al.[53] 4-Difluoro-5,7-dimethyl-3-(2-phenylethenyl)-4-bora-3a,4a-diaza-s-indacene (styrene-conjugated BODIPY or STY-BODIPY) was synthetized following the method described by Haidasz et al.[54] Fluorescence was measured using the UV/vis spectrophotometer Synergy MX, Biotek with Gen5. In order to quantify radical trapping antioxidant activity in phospholipid bilayers to a clear bottom black-walled 96-well plate for fluorescence-base assays (Invitrogen by Thermo Fisher Scientific) was added 250 μL of a solution containing liposomes (1 mM), STY-BODIPY (1 μM), and the respective radical trapping antioxidant (RTA) (4 μM). The solutions were made in larger volumes in Eppendorfs, pre-mixed and 250 μL aliquot was transferred to each well. The plate was incubated for 10 minutes at 37°C in the BioTek SynergyMx plate reader, followed by a fast-mixing protocol for 5 minutes. The plate was ejected from the plate reader and autoxidation was initiated by the addition of a 50 μL aliquot of DTUN (0.2 mM in EtOH/PBS (3/47, v/v), and the well were sealed with fluorescence compatible black film to avoid evaporation, followed by another mixing protocol for 5 minutes. Data were acquired by excitation probes at 488 nm and emission was measured at 518 nm (read intervals 1.0 min). Kinetic read parameters: (i) optic position: bottom, (ii) gain: 80, (iii) bandwidth: 9.0.

DPPH assay

The tested compounds were diluted from stock solution in absolute ethanol and incubated in the presence of 100 μM DPPH solution at 25°C in a 96-wells microplate (Fisher Scientific SAS, Illkirsh, France) in the dark. The absorbance at 517 nm was then measured every 10 minutes by using Eon microplate reader (BioTek) and data were used to calculate the specific absorbance of DPPH in each solution subtracting absorbance of all other components in the solution as following:

$$A_{max}^{DPPH} = Abs_{DPPH\ alone} - Abs_{blank}$$

$$A_{sample}^{DPPH} = Abs_{mix\ DPPH/compound} - Abs_{compound}$$

$$A_{min}^{DPPH} = Abs_{mix\ DPPH/PMC\ at\ 375\ \mu M} - Abs_{PMC\ at\ 375\ \mu M}$$

where A_max ^DPPH is the maximal absorbance of DPPH alone, A_sample ^DPPH is the specific absorbance of DPPH in a mix with a tested compound at given concentration, A_min ^DPPH is the specific absorbance of DPPH in a mix with PMC at 375 μM considered as the minimal absorbance. Then, the DPPH radical scavenging activity were calculated according to the following formula:

$$\%\ DPPH\ RSA = \frac{A_{max}^{DPPH} - A_{sample}^{DPPH}}{A_{max}^{DPPH} - A_{min}^{DPPH}} \times 100$$

Assays were conduct in triplicate at 10 concentration levels (0, 10, 12.5, 15, 25, 50, 75, 100, 125, 150, 250 μM) of the tested compound. Absorbance calculations were carried out using Microsoft Excel and regressions were performed using GraphPad Prism. The kinetic absorbance data were fitted with a one-phase exponential association model allowing us to calculate the time of half-reaction and the plateau of the maximum effect at each concentration.

Please cite this article in press as: Veeckmans et al., Ferroptosis inhibition enhances liver and lung graft function, Cell (2026), https://doi.org/10.1016/j.cell.2026.04.024

Chemical Stability

Compound (final concentration 1 μM; final DMSO concentration 0.25 %) is added to 0.1 M phosphate buffer pH 7.4 at 37 °C (final incubation volume 500 μL). A solvent control incubation is included, along with a positive control for 120 min. Compound is incubated for 0, 5, 15, 30, 60 and 120 min at 37 °C. The reactions are stopped by transferring 50 μL of incubate to 150 μL acetonitrile containing internal standard at the appropriate time points. The termination plates are centrifuged at 3,000 rpm for 30 min at 4 °C. Compounds are diluted in a 1:6 supernatant:water and analysed using UPLC-MS/MS system (Cyprotex)

Selectivity index (SI)

The selectivity index (SI) is a ratio that measures the window between cytotoxicity and the inhibitory ferroptotic effect. The higher the SI ratio, the more theoretically effective and safe a drug would be during in vivo treatment. SI values $\geq$ 10 are generally considered beneficial *in vitro*. Data is calculated by following the equation: SI = mean IC_{50} against normal cells HT-1080/mean IC_{50} from inhibition of ML162-induced ferroptosis in HT-1080.

Small molecule labelling using click chemistry and fluorescence imaging

To investigate the subcellular membrane localization of FXT-001 as a lipophilic radical trap, in situ Click-iT chemistry was performed. A Click-iT analogue of FXT-001, incorporating an alkyne moiety (C1FXT-001), was synthesized to enable fluorescent labeling with an azide-containing probe. The assay was performed independently by two laboratories (Vanden Berghe Lab and Rodriguez Lab) following a similar protocol as described elsewhere.[41] Briefly, HT-1080 cells were seeded in μ-Slide 8 Well high chambers (Ibidi, Cat.#80806) at a density of 20,000 cells per well and incubated overnight. Cells were subsequently treated with 10μM C1FXT-001 for 1 hour, fixed with 2% or 4% formaldehyde (Sigma Aldrich, Cat.#8.18708) in PBS for 12 minutes, and permeabilized with 0.1% Triton® X-100 (Millipore, Cat.#648462) in PBS for 20 minutes. A Click-iT® reaction cocktail (Cat.#C10337, Thermo Fisher Scientific) was then prepared with 86% 1X Click-iT reaction buffer, 4% $CuSO_4$ solution, 0.24% Alexa Fluor azide, and 5% reaction buffer additive (sodium ascorbate). Cells were incubated with the reaction cocktail for 30 minutes, protected from light. Subsequently, immunofluorescent staining was performed to label specific cellular membranes. The following primary and appropriate secondary antibodies were applied: Cytochrome c (6H2.B4) mouse mAb (12963, Cell Signaling Technology), RCAS1 (D2B6N) XP Rabbit mAb (Cat.#12290, Cell Signaling Technology), LAMP1 (D2D11) XP Rabbit mAb (Cat.#9091, Cell Signaling Technology), Anti-PDIA3 (CL2444) mouse mAb (Cat.#Ab90988, Sigma Aldrich), goat anti-mouse IgG Alexa Fluor 635 (Cat.#A-31574, Thermo Fisher Scientific) and donkey anti-rabbit IgG Alexa Fluor 555 (Cat.#A-31572, Thermo Fisher Scientific). All antibodies were diluted in a blocking buffer solution containing 5% BSA and 0.2% Tween-20 with each incubation performed for 1 hour. Nuclear staining was performed using 1 μg/mL DAPI (Southern Biotech, Cat. #0100-20) in 1× PBS. Cells were mounted using either PVA-DABCO mounting medium (Sigma-Aldrich, Cat. #10981) or VECTASHIELD containing DAPI (Vector Laboratories, H-1200-10). Vanden Berghe Lab: High-resolution fluorescence images were acquired using a ZEISS LSM880 Fast Airyscan confocal microscope (Carl Zeiss, Jena, Germany) operated in super-resolution Fast Airyscan mode. A Plan-Apochromat 63×/1.40 Oil DIC III objective was used for 3D acquisition of z-stacks comprising an average of 20 slices. Volume datasets were processed post-acquisition using the Airyscan processing algorithm (pixel reassignment and 2D Wiener deconvolution) in Zeiss ZEN Black 2.6 software. Colocalization analyses were performed using the JACoP (Just Another Colocalization Plugin) in Fiji. Rodriguez Lab: Fluorescence images were acquired using an Apotome Zeiss microscope with Apotome Zeiss Imaging Software. A 60× objective was used for image acquisition, and images were collected as z-stacks. Images were subsequently deconvoluted and processed using FIJI version 2.0.0-rc-69.

Isolation of mitochondria

Mitochondria were isolated using the Qproteome Mitochondria Isolation Kit (Qiagen, 37612) according to the manufacturer's protocol. Cells were washed and centrifuged at 500× g for 10 min and the supernatant was removed. Cells were then washed with a solution of 0.9% NaCl (Sigma-Aldrich, S7653-250G) and resuspended in ice-cold lysis buffer and incubated at 4 °C for 10 min. The lysate was then centrifuged at 1000× g for 10 min at 4 °C and the supernatant carefully removed. Subsequently, the cell pellet was resuspended in disruption buffer. Complete cell disruption was obtained by using a dounce homogenizer The lysate was then centrifuged at 1000× g for 10 min at 4 °C and the supernatant transferred to a clean tube. The supernatant was then centrifuged at 6000× g for 10 min at 4 °C to obtain mitochondrial pellets.

Inductively coupled plasma mass spectrometry (ICP-MS)

Glass vials equipped with Teflon septa were cleaned with nitric acid 65% (VWR, Suprapur, 1.00441.0250), washed with ultrapure water (Sigma-Aldrich, 1012620500) and dried. Cells were harvested and washed twice with 1× PBS. Cells were then counted using an automated cell counter (Entek) and transferred in 100 μL ultrapure water to the cleaned glass vials. The same volume of 1× PBS or ultrapure water was transferred into separate vials for the background subtraction, in triplicate per experiment. Samples were lyophilised using a freeze dryer (CHRIST, 2-4 LDplus). Samples were then mixed with ultrapure nitric acid 65% (VWR, Suprapur, 1.00441.0250) and heated at 80 °C overnight in the same glass vials closed with a lid carrying a Teflon septum. Samples were then cooled to room temperature and diluted with ultrapure water to a final concentration of 0.475 N nitric acid and transferred to metal-free centrifuge vials (VWR, 89049-172) for subsequent mass spectrometry analyses. Amounts of metals were measured using an Agilent 7900 ICP-QMS in low-resolution mode, taking natural isotope distribution into account. Sample introduction was

achieved with a micro-nebulizer (MicroMist, 0.2 mL/min) through a Scott spray chamber. Isotopes were measured using a collision-reaction interface with helium gas (5 mL/min) to remove polyatomic interferences. Scandium and indium internal standards were injected after inline mixing with the samples to control the absence of signal drift and matrix effects. A mix of certified standards was measured at concentrations spanning those of the samples to convert count measurements to concentrations in the solution. Values were normalised against mitochondria isolated from cell number.

Nuclear magnetic resonance spectroscopy

^{1}H NMR spectra were recorded on a 500 MHz Bruker spectrometer at 310 K using Bruker Topspin (v.4.1.4) software and analysed using Bruker Topspin (v.4.1.1) software. RFXT-001 (1.0 mg) and FXT-001 (0.8–0.9 mg) were each dissolved in 600 μL of methanol-d_4 (MeOD, Eurisotop, Cat#D048FD). For titration experiments, 3.0 μL of $FeCl_3$ or $FeCl_2$ solutions in MeOD (57.5/57.8 mM for RFXT-001; 51.4/50 mM for FXT-001) were added stepwise from 0 to 1.0 equivalent, with spectra recorded after each addition. For the naphthalene experiment, FXT-001 (0.9 mg) was pre-mixed with 1.0 equivalent of naphthalene (10 μL, 179.5 mM, Merck) in MeOD before titration with $FeCl_3$.

Chemical synthesis

The lysosomal Fe2+ probe HMRhoNox-M was synthesized as described in the literature[29] and spectral data were in accordance with the literature: 1H NMR (300 MHz, $CDCl_3$) δ 7.93 (1H, d, J = 2.0 Hz), 7.45 (dd, J = 8.5 Hz, 2.0 Hz, 1H), 7.40–7.30 (m, 3H), 7.05 (d, J = 8.5 Hz, 1H), 6.90 (d, J = 7.0 Hz, 1H), 6.80 (d, J = 8.0 Hz, 1H), 6.50–6.44 (m, 2H), 5.28–5.35 (m, 2H), 3.62 (m, 6H), 2.97 (s, 6H) ppm. The mitochondrial Fe2+ probe RPA was synthesized as described in the literature[28] and spectral data were in accordance with the literature: 1H NMR (300 MHz, $CDCl_3$) δ 11.53 (s, 1H), 9.36–9.16 (m, 2H), 8.85 (d, J = 8.1 Hz, 1H), 8.48 - 8.31 (m, 3H), 8.24 – 8.10 (m, 2H), 7.84 – 7.66 (m, 4H), 7.20-7.18 (m, 1 H), 7.06 – 6.89 (m, 6H), 6.73 (d, J = 9.3 Hz, 2H), 4.93 (s, 2H), 3.80 – 3.34 (m, 8H), 1.29 (t, J = 7.1 Hz, 12H) ppm.

Flow cytometry

Cells were seeded in 6-well plates at the density of 2×10^5 cells/well. After 24 h, cells were treated with the indicated concentrations of FXT-001, RFXT-001, C1FXT-001, Lip-1 (in-house) or Bafilomycin A1 (Baf-A1, Sigma-Aldrich, B1793) for 5 h. Cells were then treated HMRhoNox-M[29] (in-house, 1 μM) or RPA[28] (in-house, 1 μM) for 1 h. After incubation with iron probes, the media was removed and cells were washed with 1× PBS once before trypsinisation. Cells were harvested, pelleted, washed with 1× PBS and finally 500 μL of 1× PBS buffer containing 10% FBS and EDTA (0.1% v/v) was added. Data were recorded on an Attune NxT flow cytometer and analysed with FlowJo software v. 10.10.0.

Ferroptosis at 4°C

HT1080 cells were seeded into T25 flasks at a density of 950,000 cells per flask and incubated overnight to allow attachment. Once the cells reached approximately 80% confluency, the cell culture medium was supplemented with 1.7 μM Sytox Green (Fisher Scientific, Cat.#10768273) and 1 μM ML162 (Selleckchem, Cat.#S4452), followed by a 1-hour incubation at 37°C with 5% CO_2. Subsequently, the flasks were then stored under either cold (4°C in a standard laboratory refrigerator) or warm conditions (37°C in a cell culture incubator) after addition of 1 μM FXT-001 or not. To maintain consistent CO_2 levels in both conditions, the flasks were securely closed with non-filter caps before storage. After 24 hours, microscopic images were captured using a transmitted light microscope (Carl Roth, SHB 45) at 10x magnification.

Colorimetric lipid peroxidation assay

Plasma malondialdehyde (MDA), a biomarker of lipid peroxidation was measured via a colorimetric approach as previously described.[55] Briefly, 50 μL of the sample of interest was added to a reagent mixture containing 1-Methyl 2-phenylindole (NMPI, Sigma-Aldrich, Cat.#404888), acetonitrile (VWR Chemicals, Cat.#75-05-8) and methanol (Fisher Chemicals, Cat.#M/4000/17). In the presence of 37% hydrochloric acid (H/1200/PB15, Fisher Chemical) and at a temperature of 70°C, MDA reacts with NMPI producing a purple-blue colored adduct. Following centrifugation at 15,000 g for 10 minutes at 4°C, the absorbance of the supernatant was measured at 586 nm using a SPECTROStar Nano Microplate Reader (BMG Labtech). MDA concentration was calculated using a standard curve generated from 1,1,3,3-tetramethoxypropane (Sigma-Aldrich, Cat.#108383) as the source of MDA.

Epilipidomics analysis

Porcine liver tissue samples were store at -80°C, until further processing. Lipids were extracted according to Folch protocol.[56] Samples were homogenized in methanol (UHPLC-MS grade, >99.97%, Biosolve B.V, Valkenswaald, Netherlands) (volume adjusted for initial sample weight) using the Tissuelyser II Bead Mill (QiaGen). A fixed volume of tissue homogenate (200μl), corresponding to ~15mg, was transferred and used for further extraction. SPLASH LIPIDOMIX (Avanti Polar Lipids, 6 μl) and Ceramide/Sphingoid Internal Standard Mixture I (Avanti Polar Lipids Inc, 6 μl) were added and incubated for 15min. Additional methanol (920μl) and chloroform (2,240ml, analytical grade, EMSURE®) were added, samples were vortexed and incubated for 1h at 4°C with rotation (orbital shaker, 32rpm). Phase separation was induced by adding water (672μl). Samples were mixed by vortexing, incubated for 10 min 4 °C with rotation, followed by centrifugation (10 min, 1,000g, 4 °C). The lower, organic phase containing lipids was collected into new

Eppendorf tubes and dried under vacuum. Lipid extracts were reconstituted in 100μL isopropanol (ULC/MS-CC/SFC grade, >99.95%, Biosolve B.V, Valkenswaald, Netherlands) and transferred in glass vials for LC–MS analysis. To avoid oxidation, all solvents used for lipid extraction were spiked with 0.1% (w/v) butylated hydroxytoluene (BHT, Sigma Aldrich Chemie GmbH, Taufkirchen, Germany) and cooled on ice before use.

Reversed phase liquid chromatography (RPLC) was carried out on a Vanquish Horizon UHPLC (Thermo Fisher Scientific) system equipped with an Accucore C30 column (2.1×150mm,2.6μm,150Å; Thermo Fisher Scientific). Lipids were separated by gradient elution with solvent A (acetonitrile/water, 1:1, v/v) and B (isopropanol/acetonitrile/water, 85:10:5, v/v/v) both containing 5mM ammonium formate (NH_4HCO_2, MS grade, Sigma Aldrich Chemie GmbH) and 0.1% (v/v) formic acid (ULC/MS-CC/SFC grade, >99%, Biosolve B.V. (Valkenswaald, Netherlands). Acetonitrile (ULC/MS-CC/SFC grade, >99.97%) and water (ULC/MS-CC/SFC grade) were obtained from Biosolve B.V. (Valkenswaald, Netherlands). Separation was performed at 50°C with a flow rate of 0.3mL/min using following gradient: 0–20 min—10–80% B, 20–24min—80–95%B, 24–27min—95–100%, 27–32min100% (isocratic), 32.0-32.1 100-10% B, following 8 min of column equilibration at 10%. Mass spectrometry analysis was performed on an Exploris 240 Hybrid Quadrupole Orbitrap mass spectrometers equipped with a H-ESI source (Thermo Fisher Scientific) and operated in negative ion mode with the following parameters: spray voltage 2500V, sheath gas 40 arbitrary units, auxiliary gas 10 arbitrary units, sweep gas 1 arbitrary units, ion transfer tube temperature 300°C, vaporizer temperature 370°C, S-lens RF level– 35%.

Inclusion list generation and oxidized lipid identification was performed using LPPtiger 2.0.[57] Most abundant PUFA-containing (O/P-)PC, (O/P-)PE, PS, PI and PG were used for in silico oxidation including hydroperoxy, hydroxy, epoxy, and keto groups as well as truncated derivatives. All species identified by LPPtiger 2.0 were confirmed by manual inspection of MS/MS spectra (in Xcalibur QualBrowser Version 4.2.47, Thermo Fisher Scientific) and retention times mapping. For relative quantification of oxidized lipids, retention time scheduled parallel reaction monitoring using elemental composition of previously identified or computationally predicted oxidized lipids as precursors was used in negative ion mode at the resolution of 17,500 at m/z 200, AGC target of 2×10^6 and a maximum injection time of 200 ms. The isolation window for precursor selection was 1.5 m/z, and species-dependent optimized collision energy (20–40eV range) was used for HCD. Data were acquired in profile mode.

Acquired data were processed by Skyline v. 23.1[58,59] considering fragment anions of oxidized fatty acyl chains as quantifiers. The obtained peak areas were normalized by appropriate lipid species from SPLASH LIPIDOMIX Mass Spec Standard (Avanti), e.g. by LPC(18:1(d7)), LPE(18:1(d7)), PC(15:0/18:1(d7)), or PE (15:0/18:1(d7)), and the sample weights. Normalized peak areas were further log-transformed and auto-scaled in MetaboAnalyst online platform v5.0.[60] Zero values were replaced by 0.2× the minimum values detected for a given oxidized lipid within the samples. Heatmaps were created in GraphPad Prism v10.4.0. The colour scheme corresponds to auto-scaled log fold change relative to the mean log value within the samples.

Umbrella sampling (US) and classical molecular dynamics (cMD) simulations

System creation

Umbrella sampling (US) and classical molecular dynamics (cMD) simulations were performed to investigate the preferred binding locations of FXT-001 and L_1FXT-001 in a symmetrical double lipid membrane with the lipid composition shown in Table 1.

Table 1. Composition of the double lipid membrane used in the simulations. Abbreviations: MPPC: 1-myristoyl-2-palmitoyl-sn-glycero-3-phosphocholine; MOPC: 1-myristoyl-2-oleoyl-sn-glycero-3-phosphocholine; DPPC: 1,2-dipalmitoyl-sn-glycero-3-phosphocholine; POPC: 1-palmitoyl-2-oleoyl-sn-glycero-3-phosphocholine; SOPC: 1-stearoyl-2-oleoyl-sn-glycero-3-phosphocholine; DOPC: 1,2-dioleoyl-sn-glycero-3-phosphocholine; POPE: 1-palmitoyl-2-oleoyl-sn-glycero-3-phosphocholine; SOPE: 1-stearoyl-2-oleoyl-sn-glycero-3-phosphocholine; DOPE: 1,2-dioleoyl-sn-glycero-3-phopshoethanol-amine; SOPS: 1-stearoyl-2-oleoyl-sn-glycero-3-phosphoserine.

MPPC	MOPC	DPPC	POPC	SOPC	DOPC	POPE	SOPE	DOPE	SOPS
8.3%	3.1%	8.3%	37.5%	5.2%	14.6%	4.2%	7.3%	4.2%	7.3%

In this lipid bilayer, the respective molecule was immersed, and periodic boundary conditions were imposed by extending the box 60 Å in each direction along the *z*-axis. Water molecules were added and enough Na^+ and Cl^- ions were added to obtain a physiological salt concentration of 150 mM. The entire process of system setup was performed with the PACKMOL-Memgen software package.[61] Each generated box was approximately 83 x 83 x 171 Å in size. Unless indicated otherwise, all systems were simulated in constant temperature and constant pressure conditions (NPT). The temperature was kept constant at 300 K using Langevin dynamics with the collision frequency γ was set to 1.0 ps^{-1}. The pressure was set to 1.0 bar using a Berendsen barostat with semi isotropic pressure scaling, a pressure relaxation time of 1.0 ps and constant surface tension interfacing.

Force field parameters

All calculations were performed with the AMBER 24 suite of programs.[62] Water molecules were modelled according the TIP3P model,[63] and lipid parameters were from the Lipid21 forcefield.[64] GAFF2 parameters[65] for the ligands were assigned with Antechamber,[66] and their atomic partial charges were calculated using the AM1-BCC method.[67] All compounds were modelled in their neutral form, *i.e.* none of the piperazine nitrogens were positively charged. Initial attempts to work with the charged form of the compounds showed that it was impossible to pull the compounds through the membrane, as the required forces were too high and

Please cite this article in press as: Veeckmans et al., Ferroptosis inhibition enhances liver and lung graft function, Cell (2026), https://doi.org/10.1016/j.cell.2026.04.024

yielding unstable simulations. This is in accordance with similar studies on codeine and similar compounds.[68,69] In the given setup of force field-based simulations it is impossible to change the ionization state of compounds *ad hoc*, therefore one should keep in mind that the PMF values of the configurations in the aqueous phases are probably an underestimation of the actual values, as we might expect spontaneous protonation of one of the piperazine N's once in the aqueous environment. This protonation will increase the solubility of the compound in aqueous solvent and therefore alter the PMF profile.

Minimization and equilibration

Following the creation of suitable membrane boxes, each system was subsequently minimized and equilibrated. All these steps were done in triplicate to monitor statistical convergence. System minimization was performed in four stages during which positional restraints on the non-solvent atoms were gradually loosened in chunks of 20,000 minimization steps each, going from a restraint of 10.0 kcal/mol/Å^2 during the first stage, and then 2.5 and 1.0 kcal/mol/Å^2 in the following two stages. Finally, the entire system was minimized for 50,000 steps in the final unrestrained stage. After minimization, the systems were heated in a gradual manner. A series of MD and minimization steps were iterated, gradually increasing the temperature to 300 K whilst loosening the positional restraints on the non-solvent atoms from 1.0 to 0.5 kcal/mol/Å^2. Following each MD phase, 20,000 energy minimization steps were included to further remove all steric clashes. Finally, a 300 ns MD run was performed to fully equilibrate the entire system.

Umbrella sampling calculations to calculate the potential of mean force (PMF) of the aniline nitrogens with respect to the bilayer center

Equilibration. The US calculations all started by positioning the ligand on the center of the lipid bilayer. To achieve this, a restraint was imposed on the distance along the *z*-axis between the center-of-mass of all P atoms of the lipid bilayer and the center-of-mass of both aniline nitrogens of the compound. The restraint target distance was set to 0 Å and the force constant was set to 5.0 kcal/mol/Å^2. A 300 ns long MD was sufficient to position the ligand at the correct starting position.

Reaction coordinate generation. Then the reaction coordinate was generated by slowly pulling the ligand across the membrane along the z-axis. To generate this reaction coordinate and corresponding configurations, a restraint with a force constant of 100.0 kcal/mol/Å^2 was imposed on the distance along the *z*-axis between the center-of-mass of all P atoms of the lipid bilayer and the center-of-mass of both aniline nitrogens of the compound. The restraint target distance was moving from 0.0 to 50.0 Å over a total timespan of 1.5 ms, hence 30 ns / Å. Frames were saved every 3 ns, hence a total of 500 configurations that equally span a distance between 0 and 50 Å.

Umbrella sampling. The actual US calculations were performed on 101 configurations, ranging from 0.0 to 50.0 Å with a spacing of 0.5 Å. At each of these different configurations, the compound was restraint to its corresponding distance along the *z*-axis (aniline N's to lipid bilayer center) using a force constant of 5.0 kcal/mol/Å^2 and a sampling time of 200 ns on each of the 101 configurations (20.2 ms in total). During each configurational window, 100 x 10^6 distance samples were saved.

PMF calculations. PMF profiles were calculated with the weighted histogram analysis method (WHAM) of Kumar and co-workers.[70,71] All PMF profiles were made symmetrical (not only ranging from 0 to +50 Å but also from 0 to -50 Å) by simply mirroring the data of the 0 to +50 Å profile. This is possible as a symmetrical lipid bilayer was used. All PMF profiles were normalized in the sense that the configuration at 50 Å (full aqueous environment) was shifted to a value of 0.0 kcal/mol.

Classical MD calculations

Following the generation of the PMF profile, ten independent cMD simulations were run to generate distance histograms of both the aniline and the piperazine groups. Each of the cMD simulations started from the configuration in which the ligand was positioned at the minimum of the corresponding PMF profile. All ten simulations were run in parallel, spanning a total simulation length of 10 x 300 ns = 3.0 ms. A total of 20,000 snapshots were saved from which the distances histograms were calculated.

Iron intoxication model

Iron intoxication in male C57BL/6N mice was induced through a single intraperitoneal (i.p.) injection of iron(II) sulfate heptahydrate ($FeSO_4 \cdot 7H_2O$, Sigma Aldrich; Cat.#F7002-250G-D) dissolved in sterile 0.9% sodium chloride (0.9% NaCl, B.Braun; Cat.#3621502). For the 8-hour time-point experiment, a dosage of 250 mg/kg body weight of $FeSO_4 \cdot 7H_2O$ was administered at an injection volume of 200 μL per 20 g body weight. To compare the efficacy of FXT-001 or its analogues, equimolar amounts of these compounds were dissolved in sterile 0.9% NaCl and administered 30 minutes after the iron injection. The compounds were prepared at a concentration of 2 mM and administered at an injection volume of 200 μL per 20 g body weight. This corresponded to dosages of 12.35 mg/kg for FXT-001, 10.24 mg/kg for FXT-002, and 8.20 mg/kg for FXT-003. Control groups received sterile 0.9% NaCl only. For the survival study, iron intoxication was induced with 300 mg/kg $FeSO_4 \cdot 7H_2O$ (200 μL per 20 g body weight), and compounds were administered three times daily at 4 mM in 50 μL per 20 g body weight, corresponding to doses of 6.2 mg/kg (FXT-001), 5.0 mg/kg (FXT-002), and 4.1 mg/kg (FXT-003). Control groups again received sterile 0.9% NaCl only.

Rectal body temperature was monitored throughout the experiment using an industrial electric thermometer. To minimize animal discomfort, ibuprofen (Reckitt Benckiser; Cat.#2922607) was added to the drinking water at a concentration of 0.4 mg/mL, starting 16 hours prior to iron sulfate injection. At eight hours post iron sulfate injection (non-survival assay), mice were anesthetized with isoflurane, and blood was collected via intracardial puncture. Mice were then euthanized by cervical dislocation. Upon sacrifice blood was sampled in EDTA-coated tubes and subsequently centrifuged at 2,000 g for 10 minutes at 4 °C to obtain plasma for further

Please cite this article in press as: Veeckmans et al., Ferroptosis inhibition enhances liver and lung graft function, Cell (2026), https://doi.org/10.1016/j.cell.2026.04.024

analysis. Plasma levels of lactate dehydrogenase (LDH), aspartate aminotransferase (AST), and creatine kinase (CK) in mice were quantified at the clinical laboratory of the University Hospital Antwerp. In the survival experiment, no sample collection was performed, as the only readout was survival.

Porcine liver donation after circulatory death

The surgical procedures for liver donation and reperfusion in the pig model have been reported in more detail elsewhere.[30,46,72] In brief, pigs were brought under general anesthesia to allow for dissection of the infra-hepatic inferior vena cava and abdominal aorta. When requested by the protocol, and prior to liver flush-cooling, the abdominal aorta was clamped to provoke hepatic warm ischemia, mimicking donation after circulatory death. Porcine livers were flushed *in situ* with cold (4°C) preservation solution IGL-1® (Institute George Lopez, Lissieu, France) via the abdominal aorta, either immediately after cannulation, or after 60 minutes of warm ischemia, and removed from the abdominal cavity. Subsequently, all porcine livers were statically cold stored on ice for four hours. In dedicated experiments, porcine livers underwent next normothermic oxygenated reperfusion with a custom-made isolated liver perfusion device to mimic liver transplantation (see below).[30]

Pilot study: FXT-001 delivery in porcine livers during static cold storage

No sample size calculation was performed for this pilot experiment. Nine unused livers from control experiments of ongoing research projects (P038/2022 and P061/2022) were non-randomly, non-blinded assigned to three groups: (1) 4h SCS (n=3); (2) 4h SCS + 10 mg/kg FXT-001 (n=3); (3) 60'WI + 4h SCS + 10 mg/kg FXT-001 (n=3). Livers underwent the procedure of donation after circulatory death until SCS (without normothermic oxygenated reperfusion), but group (1) and (2) did not undergo warm ischemia. Needle biopsies were taken at start of storage (0h) and every hour (1-4h) from four different segments (III; IV; V; VI) and used for FXT-001 detection using mass spectrometry analysis (see below). In addition, bile duct samples and liver wedges from the same segments were taken for lipid peroxidation measurements (MDA) at each timepoint. The results of all lobes were pooled per timepoint.

Preclinical model of isolated, oxygenated, normothermic reperfusion of porcine livers

This model was chosen for its ability to mimic transplantation by replicating early post-transplant immune driven IRI-events on the perfusion device.[30] Livers were procured according to the porcine livers donation after circulatory death procedure described above but, at the back-table, they were non-randomly, non-blinded assigned to receive a second flush with either 1L of cold IGL-1® containing (1) 10 mg/kg FXT-001 (University of Antwerp, Belgium) (n=5) or (2) not (controls, n=5). Subsequently, the grafts were statically stored on ice for four hours. During this phase, the preservation solution was either enriched with 10 mg/kg FXT-001 or not, according to group allocation. Next, the livers were reperfused with a custom-made isolated liver perfusion device for 6 hours to mimic liver transplantation.[30] An overview of the experimental set-up is provided in Figure 3A. Briefly, portal vein perfusion was accomplished via gravity flow (target portal pressure 5-8 mmHg), while hepatic artery perfusion utilized a centrifugal pump with pressure-controlled non-pulsatile flow (Medtronic, target hepatic arterial pressure 60-80 mmHg). The perfusate, consisting of geloplasma (Cat.# 247429, 500mL) and leukocyte-containing blood (target hematocrit 30%), was oxygenated (target pO2 70-100 mmHg), thermally maintained at 38°C, and supplemented with standard additives including heparin (Cat.#BR-1005), antimicrobial agents, calcium gluconate (Cat.# 570/13596667/1214), and sodium bicarbonate (Cat.#3622339). Plasma/perfusate samples were collected at baseline (before surgery), at start of perfusion (0'), after 30 minutes (30') and every hour (1-6h) of reperfusion. Needle biopsies were collected at baseline, at the end of cold storage, and after 30', 1h, 3h and 6h of reperfusion. Bile duct samples were collected at baseline, at the end of cold storage and at 6h of reperfusion. Bile samples were collected at baseline, at the end of warm ischemia and every hour during perfusion (1-6h, if produced). The AUC of the perfusate AST concentrations was defined as primary outcome measure. (ALT, LDH, Suzuki scoring), inflammation (IL-6 (Cat.#ESIL6), IL-8 (Cat.#P8000), IL-10 (Cat.#P1000), TGFβ (Cat.#DB100C), IL-1β (Cat.#PLB00B) and TNFα (Cat.#PTA00)), lipid peroxidation (MDA, 4-HNE (Cat.# ab46545), oxidative lipidomic), redox capacity (GPX4 (Cat.#MBS420590)) and cell death (TUNEL (Cat.#12156792910)) were also analysed on plasma and/or tissue samples, which are described in more detail in dedicated sections. Control and treatment experiments were performed by two distinct transplant surgeons with experience in this porcine model, five months apart from each other. Due to technical failure of the perfusion machine, one experiment was prematurely terminated at 4h of reperfusion. Therefore, only 4 datapoints were analysed in group (1) at 5-6h.

Liver transaminases

AST, ALT and LDH perfusate concentrations were assessed through the International Federation of Clinical Chemistry method (COBAS 8000; Hitachi/Roche; Roche, Vilvoorde, Belgium) by the central laboratory of UZ Leuven. For AST and ALT, a colorimetric assay was applied (without pyridoxal phosphate activation). Signals were quantified through absorbance measurements. For LDH, a kinetic assay of lactate and pyruvate was applied at 37°C, using an N-methylglucamine buffer (Sigma Aldrich; Cat.#M2004) and quantified through UV measurements. To address the weight differences between livers, all concentrations were expressed per 100g (U/L/100g).

Hematoxylin and eosinophil staining

Hematoxylin and eosinophil (H&E) stainings were performed on 5 μm liver or lung paraffin sections by the Translational Cell and Tissue Research unit at KU Leuven according to standard operating procedures. Briefly, paraffin sections were deparaffinized using

xylene (Carl Roth; 1330-20-7) and declining ethanol (Thermo Fisher; cat.#E-0600DF-17) concentrations (100%-50%). Afterwards, nuclei were stained using hematoxylin (Sigma-Aldrich; Cat.# 1.15938.0100) and an eosinophil (Carl Roth; 17372-87-1) counterstain was applied to stain the cytoplasm. Lastly, the stained sections were dehydrated with increasing ethanol concentrations and xylene, and slides were mounted using DPX (Sigma-Aldrich; Cat.#1.00579). Liver parenchymal injury was quantified in a blinded manner by a pathologist based on Suzuki scoring, which evaluates features of sinusoidal congestion, cytoplasmic vacuolization, and parenchymal necrosis.

4-hydroxynonenal immunofluorescence staining

4-hydroxynonenal (4-HNE) immunofluorescence staining was performed according to the published protocol.[73] In short, 5 μm paraffin sections of liver and lung tissue were deparaffinized using xylene and declining ethanol concentrations (100%-50%). After heat-induced antigen retrieval in a citric acid buffer, slides were washed and incubated with the primary antibody (1/500; Cat.# ab46545) overnight at 4°C. Afterwards, tissue slides were washed and incubated with the secondary antibody (4 μg/mL; Cat.# A-11008) for 1h at room temperature. Next, cell nuclei were stained using DAPI (Cat.#62248) and washed with PBS. After mounting, the slides were dried overnight and visualized. The percentage of 4-HNE positive area was quantified using the 'Analyze Particles' feature in ImageJ/Fiji in multiple areas per slide.

Glutathione peroxidase 4 western blot

Glutathione peroxidase 4 (GPX4) concentration was determined by western blotting as previously described.[74] Briefly, 50 μg of tissue homogenates were prepared in PBS containing β-mercaptoethanol (3 minutes at 95°C) and loaded on a precast gell (Cat.#4569036, Mini-PROTEAN TGX gells, Bio-Rad, USA). SDS-PAGE was performed to separate proteins based on kD (150 V). Next, proteins were blotted on a membrane (#1704156, Transfer Turbo Transfer Pack, Bio-Rad, USA), that ultimately was blocked (room temperature, 1h, 5% milk powder), incubated with primary antibody (4°C, overnight), washed (PBS-T) and incubated with secondary horseradish peroxidase coupled antibody (room temperature, 45 minutes). After washing (PBS-T), immunoreactive bands were visualized through chemiluminescence. Band intensity was quantified using Chemidoc MP techniology and associated Imagelab software (Bio-Rad, USA).

Inflammatory cytokine analysis

Pro- and anti-inflammatory cytokines IL-6 (Cat.#ESIL6), IL-8 (Cat.#P8000), IL-10 (Cat.#P1000), TGFβ (Cat.#DB100C), IL-1β (Cat.#PLB00B) and TNFα (Cat.#PTA00)) concentrations were measured in liver perfusate using ELISA kits according to the manufacturer's instructions.

Porcine lungs mounted on *ex vivo* lung perfusion setup

15 pigs (median weight 42,6 kg) were randomly divided into 3 experimental groups (n=5/group). In the control condition, donor lungs were cold-flushed in situ, harvested, cannulated, and connected to an ex vivo lung perfusion (EVLP) system. All other lungs underwent 3 hours of warm ischemia in the donor animal prior to surgical removal, cannulation, and EVLP initiation. At the start of EVLP, no additives were added to the perfusate (Steen Solution™, Xvivo Perfusion AB, Gothenburg, Sweden) in the vehicle-treated group, whereas the FXT-001-treated lungs received the ferroptosis inhibitor. The duration of EVLP was set at 8 hours for all experimental groups.

The pilot experiment conducted on an iron sulfate treated porcine lung graft was performed in the same manner as for the control lungs. $FeSO_4.7H_2O$ (Sigma Aldrich; Cat.#F7002-250G-D) was added to the perfusate after 1 hour of reperfusion (steady-state).

Porcine donor procedure ex vivo lung perfusion

All animals were sedated with an intramuscular injection of 5 mg/kg Zoletil® 100 (Virbac, Carros, France, Cat.#1164330) and 3 mg/kg Xyl-M® 2% (V.M.D., Arendonk, Belgium, Cat.#000533). Anesthesia was maintained by continuous intravenous administration of propofol 10 mg/kg/h (PropoVet® Multidose 10mg/ml, Zoetis BV, The Netherlands, Cat.#1175472) and intermittent boli of fentanyl (Fentanyl-Piramal®, Piramal Critical Care BV, Voorschoten, The Netherlands, Cat.#41558) and pancuronium (Pancuronium Inresa®, Inresa Arzneimittel Gmbh, Freiburg, Germany, Cat.#07714122). The animals were intubated with an endotracheal tube (Mallinckrodt™; inner diameter 8.0 mm) and mechanically ventilated (Evita 2, Dräger Medical GmbH, Lübeck, Germany) using a volume-controlled ventilation mode with a tidal volume (TV) of 7 ml/kg, positive end-expiratory pressure (PEEP) of 5 cmH_2O and fraction of inspired oxygen (FiO_2) of 0.3. A recruitment maneuver was performed (peak airway pressure 30 cmH_2O for 30 seconds), and the respiratory rate (RR) was adjusted to maintain an end-tidal CO_2 between 45 and 55 mmHg. A right-sided neck dissection was performed for invasive arterial blood pressure monitoring in the right carotid artery and a large-bore central venous introducer was inserted into the right external jugular vein.

In the control group, after baseline sampling, a median sternotomy was performed. Both caval veins were encircled and a purse-string was sutured to the right ventricular outflow tract to secure a 20-Fr flush cannula into the pulmonary trunk. After inflow occlusion, clamping of the ascending aorta and incision of the left atrial appendage, lungs were flushed antegrade using 2 liters of cold (4°C) Perfadex® Plus solution (Xvivo Perfusion AB, Gothenburg, Sweden, Cat.#19800), while maintaining mechanical ventilation. 500ml of whole blood was drained through the large-bore central venous introducer into a collection bag with added acid-citrate-dextrose

Please cite this article in press as: Veeckmans et al., Ferroptosis inhibition enhances liver and lung graft function, Cell (2026), https://doi.org/10.1016/j.cell.2026.04.024

solution (Terumo Europe NV, Leuven, Belgium, Cat.#40818) and subsequently stored at room temperature. Next, the heart-lung block was surgically excised, the heart was removed, and the lungs were stored on ice in a deflated state. During a short instrumentation time the Xvivo Lung Cannula Set™ was used to cannulate the pulmonary artery and the left atrium, and an 8.0 mm endotracheal tube was re-inserted into the trachea. Finally, an additional retrograde flush using 500 ml of cold (4°C) Perfadex® Plus solution was performed. During this procedure, leakages at the cannula anastomoses were checked and secured if necessary.

In the vehicle- and FXT-001-treated groups, after baseline sampling, 500 IU/kg sodium heparin (LEO Pharma BV, Amsterdam, The Netherlands) was administered intravenously prior to inducing a hypoxic-hypovolemic arrest. This was done by disconnection of the endotracheal tube, while simultaneously draining 500ml whole blood through the central venous introducer. After a short agonal phase, circulatory arrest developed, and the lungs were left untouched and deflated in the deceased donor animal. After 2 hours, a median sternotomy was performed, caval veins encircled and pulmonary trunk cannulated as described before. Subsequently, after a total warm ischemic interval of 3 hours, the lungs were flushed antegrade with 2 liters Perfadex® Plus solution, while re-initiating mechanical ventilation. The first liter flush was administered at room temperature (21°C) while the next liter was administered at 4°C. Excision, storage and instrumentation of the pulmonary grafts were performed in the same way as in control lungs. Similarly, back-table instrumentation was followed by a retrograde flush using 500 ml cold (4°C) Perfadex® Plus.

Ex vivo lung perfusion protocol

Our EVLP setup consisted of a centrifugal pump, a reservoir, an oxygenator, a heater-cooler element, and tubing. A flow probe (Transonic Systems Inc, NY, USA) was placed around the inflow limb, and temperature was measured in both inflow and outflow limbs. The circuit was primed with 1500 ml Steen Solution™ (Xvivo Perfusion AB, Gothenburg, Sweden, Cat.#19004). 10,000 IU of sodium heparin (LEO Pharma BV, Amsterdam, The Netherlands, Cat.#1361559), 500 mg methylprednisolone (Solu-Medrol®, Pfizer n.v., Elsene, Belgium, Cat.#075801), and 5 mg milrinone (Corotrope®, Sanofi, Diegem, Belgium, Cat.#0457457) were added to the perfusate. Finally, 400 ml of the previously drained whole pig blood was added to create a cellular perfusate and to maximally evoke lung injury and ferroptosis.

Our EVLP technique was based on the Toronto protocol. The non-sterile donor lungs were placed in an Xvivo Organ Chamber™ in a supine position. During the first hour, the lung grafts were gradually reperfused and rewarmed up to a target flow of 40 ml/kg pig weight (40% of predicted cardiac output) and a target temperature of 37°C. Mechanical ventilation was initiated when the effluent temperature of the graft reached 34°C. A volume-controlled ventilation mode was used with TV 7 ml/kg, PEEP 5 cmH_20, RR 7/min and FiO_2 0.21. A recruitment maneuver (peak airway pressure 25 cmH_20 for 30 seconds) was performed when effluent temperature was 37°C. The gas-flow to the oxygenator (a mixture of oxygen, CO_2 and nitrogen) was used to de-oxygenate the inflow perfusate and maintain an inflow perfusate mixed venous gas composition. Sodium bicarbonate (B. Braun, Melsungen, Germany, Cat.#3622339) was added to the perfusate if necessary to keep inflow pH between 7,35 and 7,45. The height of the reservoir was adjusted to maintain left atrial pressure between 3 and 5 mmHg. A steady-state EVLP was reached after 1 hour and continued for another 7 hours. The flowrate through the graft was kept constant at the target flow. Hourly, FiO_2 was set at 1.0 for 3 minutes to determine oxygenation capacity (PO_2/FiO_2 ratio). No other changes were made to the ventilatory settings and recruitment maneuvers were not repeated.

Data and sample collection during ex vivo lung perfusion

In the donor animal and during EVLP, all circulatory and respiratory/ventilatory parameters were recorded continuously using ICM+® (Cambridge Enterprise, Cambridge, UK). After catheter placement in the donor animal, venous (FiO_2 3.0) and arterial (FiO_2 1.0) blood gas analysis was performed, and a venous blood sample was taken to determine ferroptosis markers and cytokine profile. During EVLP, peak airway pressure and dynamic compliance (Cdyn) were continuously recorded, and PaO_2/FiO_2 ratio was assessed hourly. Pulmonary vascular resistance was calculated based on the measurement of transpulmonary pressure gradient and transpulmonary flow. Perfusate samples were collected, centrifuged and stored at predefined time points: baseline (before start of EVLP), and, 30, 60, 120, 180, 240, 300, 360, 420 and 480 minutes after the start of EVLP. At the end of the experiment, tissue samples were collected from the right lower lobe, placed in a dehydrator (80°C) and weighed after 72 hours to calculate wet-to-dry (W/D) weight ratio. The right lung was completely removed, and the left lung was frozen in an inflated state (peak airway pressure 25 cmH_20). The frozen lungs were ex-vivo computed tomography (CT) scanned (Siemens Healthcare, Erlangen, Germany) to determine regional parenchymal density as a marker of lung injury, and analysis was performed with HOROS™ (DICOM Viewer, version 3 (LGPL-3.0). Perfusate cytokine levels (IL-6, IL-8, IL-10, IFN-γ, IL-1β and TNF-α) were measured using a personalized Bio-Plex Multiplex immunoassay from Thermo fisher Scientifics (Cat.#PPX-06-MXEPVRF) according to the manufacturer's instruction. MDA analysis of perfusate samples was performed as described previously.

Human lung grafts during ex vivo lung perfusion

Five pairs of human lungs were used to assess the effectiveness of treatment. Lungs were declined for clinical transplantation for too low quality and harvested by the local surgical procurement team (University Hospitals Leuven) in the donor hospital, stored on ice and transported to our laboratory. Each lung block was surgically split on the level of the main bronchi, pulmonary artery bifurcation and the pulmonary veins. A left atrial cuff was created on both sides. Next, these lungs were cannulated separately using an Xvivo Lung Cannula Set™, and an 8.0 mm endotracheal tube was re-inserted into the trachea and the left main bronchus. Finally, an

Please cite this article in press as: Veeckmans et al., Ferroptosis inhibition enhances liver and lung graft function, Cell (2026), https://doi.org/10.1016/j.cell.2026.04.024

additional retrograde flush with 500 ml of cold (4°C) Perfadex® Plus solution was performed to rule out any leakages at the cannulation sites.

Each lung was placed on a split-EVLP setup, and reperfusion was initiated simultaneously to avoid differences in ischemic times. The EVLP technique used was identical to that in the porcine experiments. However, total perfusion flow and tidal volume during mechanical ventilation were divided between left and right lung according to physiological differences observed *in vivo*. During reperfusion, vehicle was added to the perfusate of one lung, while the other lung from the same donor received FXT-001. The lungs remained on the EVLP setup for 6 hours or until one of the perfusate reservoirs was empty. Data collection and sampling was comparable to the porcine experiments. Additionally, each lung was weighed before and after EVLP to determine the weight gain during reperfusion as an indicator of increased extravascular lung water. Tissue samples were collected from both medial and lateral parts of all lower lobes.

QUANTIFICATION AND STATISTICAL ANALYSIS

Statistical analysis: Data are presented as mean ± s.e.m. or s.d., as specified. For box plots, boxes represent the interquartile range and median, with whiskers extending from the minimum to maximum values. Statistical analyses were performed using GraphPad Prism (v.10.5.0), employing two-sided Mann–Whitney U test, unpaired two-tailed t test, Kruskal–Wallis test, Welch's t-test, nested t-tests, one-way ANOVA, repeated measures two-way ANOVA, mixed-effects models, Spearman correlations, chi-squared goodness-of-fit test, and a wilcoxon matched-pairs signed rank test, as appropriate. Tukey's multiple comparison test was applied when comparing two groups at a single timepoint of a dataset. Graphs were generated using Prism (v.10.0.3), unless stated otherwise. Sample sizes (n) are provided in the figure legends. P values < 0.05 were considered statistically significant, and exact p values are shown in the figures. All statistical analyses were carried out in collaboration with a statistician to ensure methodological accuracy.

Resource availability

MS analysis and NMR spectra data have been deposited in Mendeley Data and are publicly available as of the date of publication. Mendeley Data: 10.17632/n7jbyznw8g.1. This article does not report any original code. Any additional information required to reanalyze the data reported in this article is available from the lead contact upon request.

Supplemental figures

A

		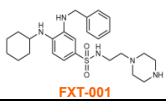 FXT-001	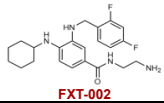 FXT-002	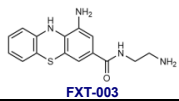 FXT-003
ADME Properties				
Ferroptosis inhibition in HT-1080 cells (IC_{50} (nM))		9.76 ± 6.71 (n=6)	6.91 ± 4.99 (n=3)	11.7 ± 7.39 (n=2)
Kinetic Solubility at pH 7.4 (μM)		> 200	> 200	> 200
HT Thermodynamic Solubility at pH 2 (μM)		8094	1265	> 2000
HT Thermodynamic Solubility at pH 7.4 (μM)		6900	439	> 2000
Distribution coefficient (LogD at pH 7.4)		2.43	2.12	0.449
Calculated partition coefficient (cLogP)		4.20	4.80	2.30
Chemical stability at pH 7.4 (%)		100	38.6	51.1
Plasma stability (%)	human	100	100	88
	mouse	93	100	12
Plasma protein binding (*unbound fraction %*)	human	6.1	1.7	67
	mouse	3.7	1.1	< 91
Microsomal stability (*μL/min/mg protein*)	human	29.3	2.90	< 1
	mouse	48.0	9.70	2.12
	rat	23.3	33.8	0.57
	dog	126	17.1	< 9.7
Hepatocyte stability (*μL/min/10^6 cells*)	human	21.2	24.0	15.8
	mouse	60.0	31.2	41.6
Permeability (MDCK-MDR1)		Not permeable	Not permeable	Not permeable
Safety and Toxicity properties				
Cytotoxicity in HepG2 cells (EC_{50})		19.5 μM (SI > 1900)	6.98 μM (SI > 1000)	48.6 μM (SI > 4000)
Mitochondrial Toxicity		Non-mitotoxic Glu/Gal: 1.030	Non-mitotoxic Glu/Gal: 0.684	Non-mitotoxic Glu/Gal: 0.947
Cardiotoxicity	hERG channel inhibition	IC_{50} = 2.4 μM	IC_{50} = 0.7 μM	N/C*
	Nav1.5 channel inhibition	IC_{50} > 30 μM	IC_{50} > 30 μM	N/C*
	Cav1.2 channel inhibition	IC_{50} > 30 μM	IC_{50} = 3.9 μM	N/C*
Micronucleus test	TK6 cells (24h)	negative	negative	negative
	TK6 cells + S9 (3h)	negative	negative	negative
Reactive metabolite formation (GSH trapping)		No reactive metabolites	No reactive metabolites	No reactive metabolites
Phospholipidosis		AC_{50} ≈ 15 μM PLD potential: YES	No response PLD potential: NO	No response PLD potential: NO
Cytotoxicity Screening Panel (μM)	Cell count	AC_{50} = 8.3	AC_{50} = 5.9	AC_{50} = 40
	Nuclear size	AC_{50} > 10	No response	AC_{50} > 40
	DNA structure	AC_{50} > 10	AC_{50} > 4.0	No response
	Cell membrane permeability	AC_{50} > 10	No response	No response
	Mitochondrial mass	AC_{50} > 10	No response	No response
	Mitochondrial membrane potential	AC_{50} > 10	No response	AC_{50} > 40
	Cytochrome c	AC_{50} > 4.0	No response	No response
Ames fluctuation (genotoxicity, μM)	TA98±S9	Not mutagenic at 5 μM	Not mutagenic at 1.2 μM	Not mutagenic at 25 μM
	TA100±S9	Not mutagenic at 5 μM	Not mutagenic at 2.5 μM	Not mutagenic at 25 μM
	TA1535±S9	Not mutagenic at 5 μM	Not mutagenic at 5 μM	Not mutagenic at 50 μM
	TA1537±S9	Not mutagenic at 10 μM	Not mutagenic at 2.5 μM	Not mutagenic at 25 μM
CYP450 Inhibition assay (μM)	CYP 1A2	IC_{50} > 25	IC_{50} > 25	IC_{50} > 3.6
	CYP2B6	IC_{50} > 25	IC_{50} > 25	IC_{50} > 25
	CYP2C8	IC_{50} > 25	IC_{50} > 25	IC_{50} > 25
	CYP2C9	IC_{50} > 25	IC_{50} > 25	IC_{50} > 25
	CYP2C19	IC_{50} > 25	IC_{50} > 15	IC_{50} > 2.7
	CYP2D6	IC_{50} > 25	IC_{50} > 15	IC_{50} > 9.0
	CYP3A4	IC_{50} = 14 [a] IC_{50} = 3.9 [b]	IC_{50} > 19 [a] IC_{50} > 15 [b]	IC_{50} > 25 [a] IC_{50} > 25 [b]
Off-target activities *(Safety Screen 87 Panel)* Binding (%)	Muscarinic acetylcholine receptor (GPCR)	M2 86.4 M3 54.8 M4 93.9	ND	ND
	Opioid receptor (GPCR)	mu (MOP) 97.0 Kappa (KOP) 82.0		
	Serotonin receptor (GPCR)	5-HT2A 81.2 5-HT2B 61.0 5-HT2C 61.0		
	Ion channel	hERG 63.2 Cav1.2 (L-type)* 65.3 sodium* 77.2		
	Vasopressin receptor (GPCR)	V1A 63.8		
	Prostaglandin-endoperoxide synthase	COX2 83.9		

(figure continued on next page)

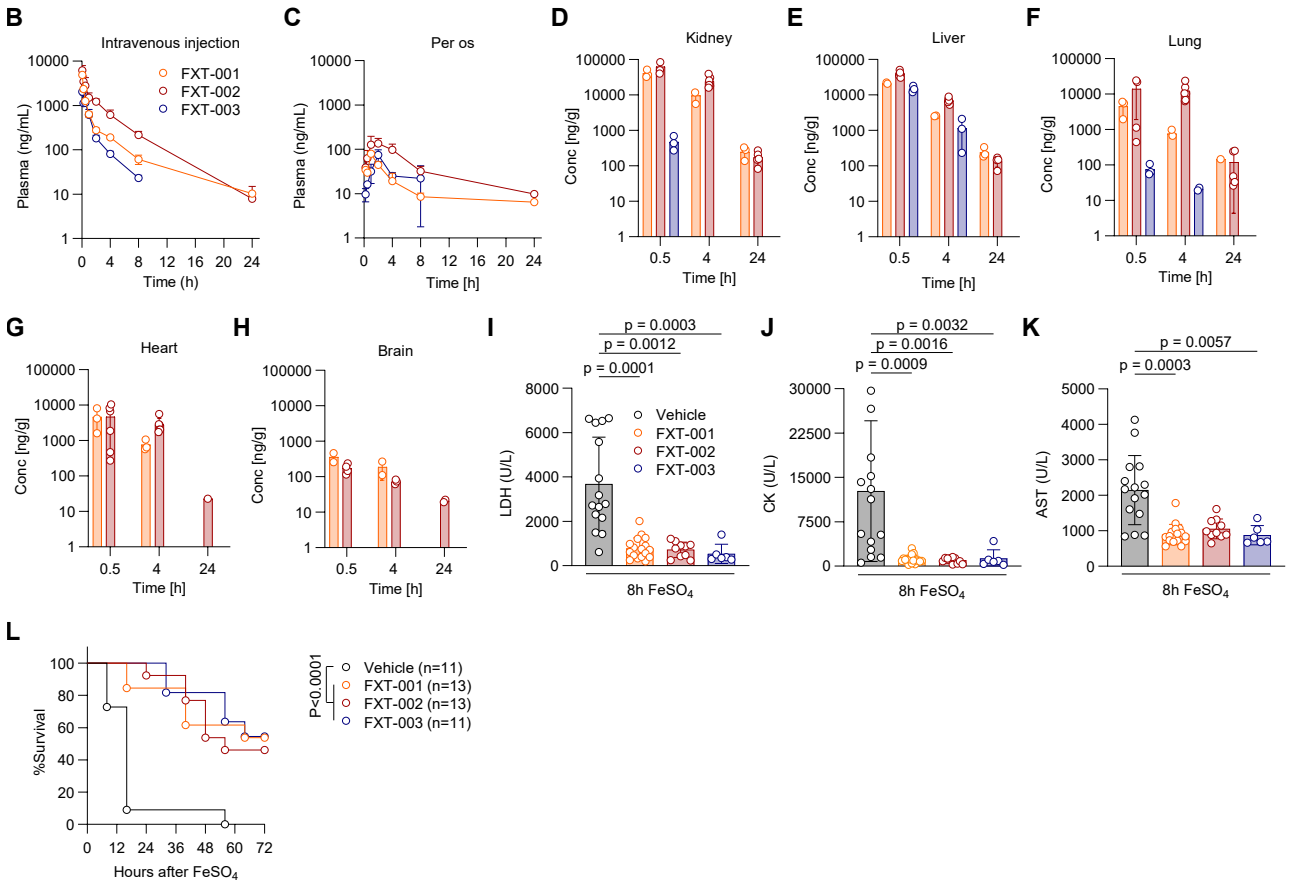

Figure S1. Comparative evaluation of ADME, safety-toxicity, pharmacokinetics, and therapeutic efficacy *in vivo* of two lead ferroptosis inhibitors compared with FXT-001, related to Figure 1

(A) Ferroptosis inhibition (IC_{50}, HT1080 cells, mean ± SD).) Kinetic solubility (PBS). High-throughput aqueous solubility (24 h, USP buffer, pH 2 [0.2 M hydrochloric acid buffer] and pH 7 [0.2 M phosphate buffer]). LogD (n-octanol/0.1 M phosphate buffer). cLogP was calculated using CDD Vault software (CDD, Burlingame, California, USA). Chemical stability after 2 h incubation (phosphate buffer, pH 7.4, 37°C). Plasma stability after 2 h incubation using species-specific plasma (37°C). Plasma protein binding reported as unbound fraction after 4 h incubation at 37°C. Microsomal stability expressed as intrinsic clearance in human, mouse, rat, and dog liver microsomes. Hepatocyte stability expressed as intrinsic clearance in human, mouse, and rat hepatocytes. MDCK-MDR1 permeability after 1 h (10 μM, HBSS, pH 7.4, 37°C, $n = 2$). Cytotoxicity, (EC_{50}), HepG2 cells, mean [$n = 3$]). Glucose/galactose fold change (AC_{50} ratio, HepG2 cells in medium supplemented with glucose or galactose [$n = 3$]). Cardiotoxicity, hERG inhibition, ion channel sodium (Nav1.5) and calcium (Cav1.2) using Qube electrophysiological platform automated patch clamp (APC) (IC_{50}, HEK293 cells). N/C* = indicates observed mean inhibition was < 25% or no dose-dependent response was observed. Reactive metabolite formation determined in human microsomes after 60 min in presence of stable labeled and unlabeled GSH. Phospholipidosis (AC_{50} ratio, HepG2 cells after 72 h incubation [$n = 3$]). Cytotoxicity screening panel (AC_{50}, HepG2 cells after 72 h incubation [$n = 3$]). CYP450 inhibition (IC_{50}, 7 isoforms, 8 substrates, 6 concentrations, 5–15 min incubation, 37°C). Safety Screen 87 Panel (Eurofins), *from rat cerebral cortex. For Cav1.2 (L-type), 4 Ca1.2 channel were measured. ND, not determined; [a]substrate testosterone; [b]substrate midazolam.

(B and C) Time-dependent plasma level following i.v. (B, 10 mg kg^{-1} or 2 mg mL^{-1}) or oral (C, 10 mg kg^{-1} or 1 mg mL^{-1}) administration of FXT-001, FXT-002, or FXT-003 in CD-1 male mice ($n = 3$–6).

(D–H) Time-dependent tissue distribution after i.v. administration (10 mg kg^{-1} or 2 mg mL^{-1}) of FXT-001, FXT-002, and FXT-003 in kidney (D), liver (E), lung (F), heart (G), and brain (H) of CD-1 male mice ($n = 3$).

(I–K) Plasma levels of LDH, CK, and AST in male mice (C57BL/6N) subjected to acute iron overload (i.p. 250 mg kg^{-1}) 8 h after treatment with vehicle, or equimolar amounts of FXT-001 (i.p. 12 mg kg^{-1}), FXT-002 (i.p. 10 mg kg^{-1}) or FXT-003 (i.p. 8 mg kg^{-1}). The combined results of two independent experiments are shown. Number of mice as indicated.

(L) Survival curve after acute iron overload (i.p. 300 mg kg^{-1}) for male mice (C57BL/6N) treated three times daily with vehicle (0.9% NaCl), or equimolar amounts of FXT-001 (i.p. 6.2 mg kg^{-1}), FXT-002 (i.p. 5 mg kg^{-1}) or FXT-003 (i.p. 4.1 mg kg^{-1}). The combined results of two independent experiments are shown. (I–K) Data were analyzed using Kruskal-Wallis followed by Dunn's post hoc test, and via (L) the Mantel-Cox test.

See also Methods S1; Table S1; Data S1.

(legend continued on next page)

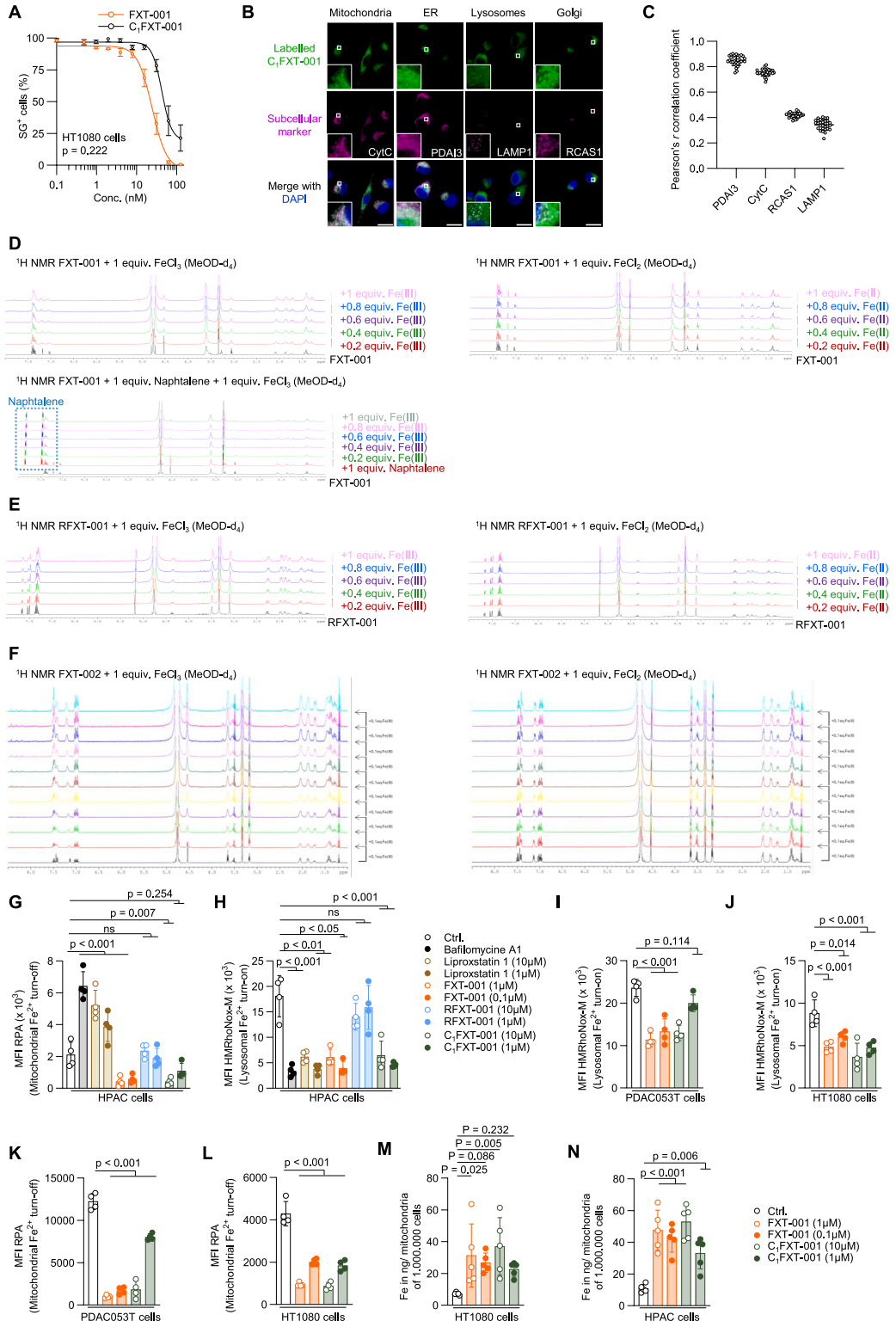

Figure S2. FXT-001 localizes to distinct subcellular organelles, selectively binds Fe^{3+}, and alters intracellular iron homeostasis, related to Figure 2

(A) Percentage of Sytox Green-positive HT1080 cells pretreated with 100 nM ML162, followed by treatment with FXT-001 or C_1FXT-001 (125–0.488 nM). Fluorescence (485/520 nm) measured at 24 h; mean ± SEM (n = 3).

(legend continued on next page)

(B) Fluorescence microscopy images showing C_1FXT-001 labeled with Alexa Fluor 488 Azide in HT1080 treated cells (10 μM for 1 h). Monoclonal antibodies against PDIA3, cytochrome *c*, RCAS1, and LAMP1 were used to stain the endoplasmic reticulum, mitochondria, Golgi apparatus, and lysosomes, respectively. DAPI was used to stain nuclear DNA. Scale bar represents 20 μm. z stacks were processed as maximum intensity projections.
(C) Pearson's correlation coefficient used to assess the linear correlation between the intensity values of corresponding individual pixels in the fluorescent channels. Between 100 and 150 cells/subcellular marker were imaged, and analysis was performed on z stack data using ImageJ with the Just Another Co-localization Plugin (JACoP) plugin. Mean ± SD.
(D) ^{1}H NMR spectra of FXT-001 in methanol titrated with $FeCl_3$ and $FeCl_2$ and ^{1}H NMR spectra of FXT-001 + naphtalene in methanol titrated with $FeCl_3$.
(E) ^{1}H NMR spectra of RFXT-001 in methanol titrated with $FeCl_3$ and $FeCl_2$.
(F) ^{1}H NMR spectra of FXT-002 in methanol titrated with $FeCl_3$ and $FeCl_2$.
(G–N) (G, H, and N) Data generated using HPAC cells, (I and K) data generated using PDAC053T cells, and (J, L, and M) data generated using HT1080 cells. (G–L) Flow cytometry of cells treated with the indicated compound for 5 h and then with the mitochondrial iron(II) turn-off probe RPA or lysosomal iron(II) turn-on probe HMRhoNox-M for 1 h. $n = 4$ independent experiments. MFI, mean fluorescence intensity. (M and N) Total iron content in mitochondria measured by ICP-MS. Statistical differences shown for the cell death assays were analyzed using an unpaired, two-tailed *t* test (A). An ordinary one-way ANOVA followed by Sidak test was used to compare differences between the groups (G–N).
See also Methods S1; Data S1.

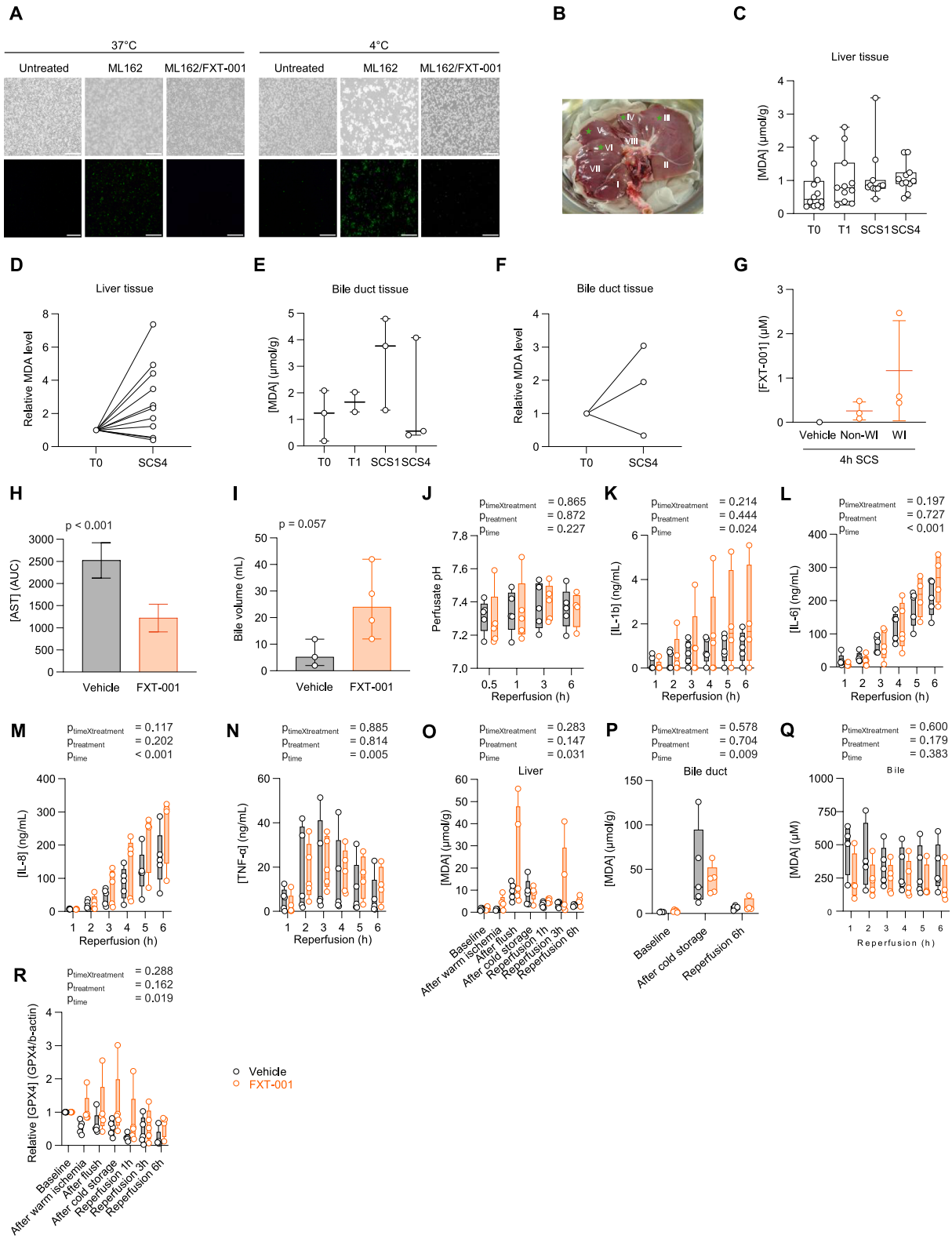

(figure continued on next page)

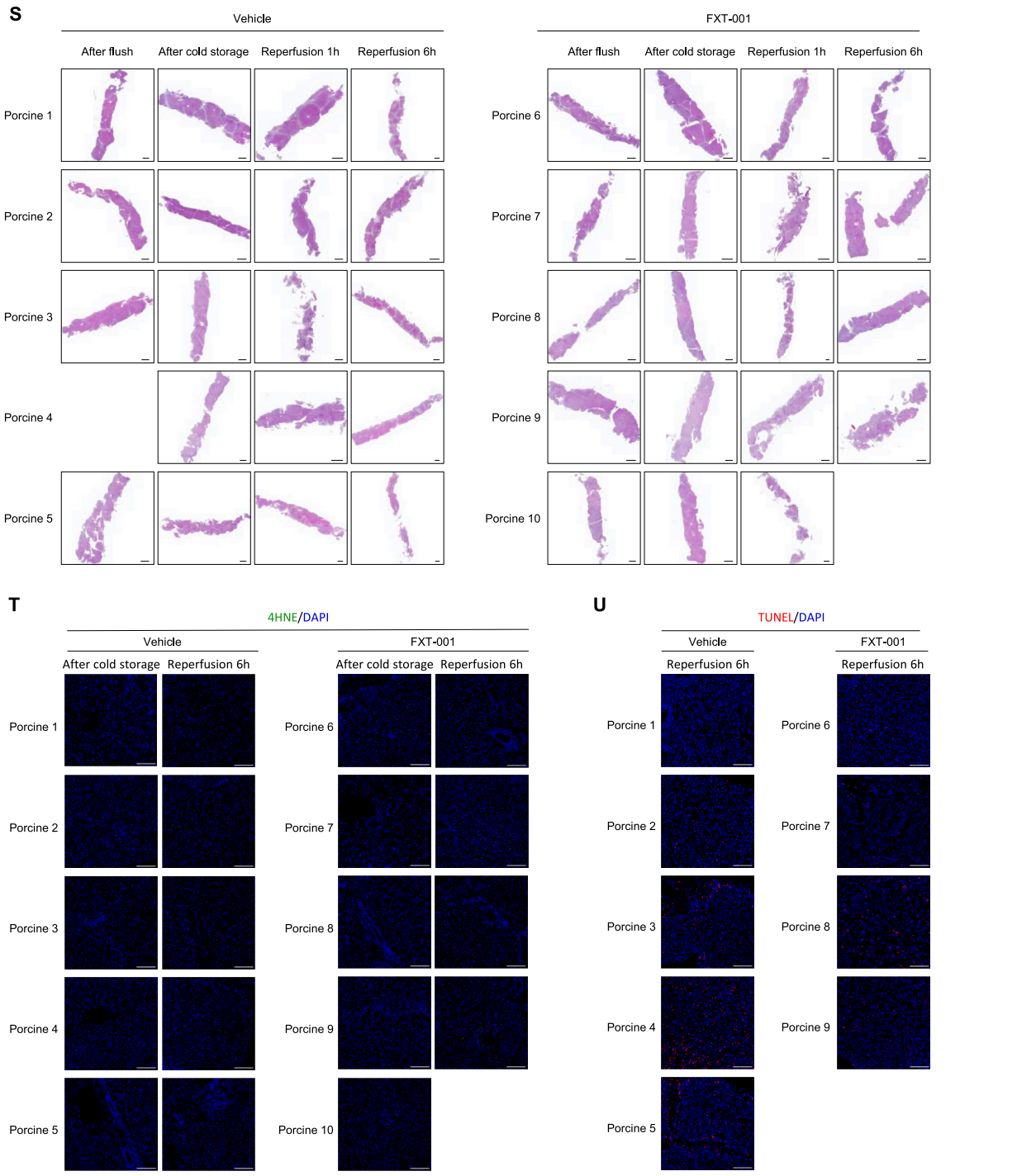

Figure S3. Lipid peroxidation occurs under hypothermic conditions, and FXT-001 improves liver injury and function in a preclinical pig model of DCD, related to Figure 3

(A) Microscopic images of HT1080 cells treated with 5 μM ML162 (ferroptosis inducer) at either 37°C or 4°C, in the presence or absence of 1 μM FXT-001 (ferroptosis inhibitor). Sytox Green nucleic acid stain was used to identify dead cells. Images were taken 24 h after ferroptosis induction. Scale bar represents 500 μm.

(B–G) Pilot study performed in porcine livers subjected to either 4 h SCS (non-WI livers, $n = 3$) or 1 h WI followed by 4 h SCS (WI livers, $n = 3$). Needle biopsies and tissue wedges were taken at the end of procurement (T0), end of cold flush (T1), and after 1 h (SCS1) and 4 h (SCS4) of cold storage (B) from four liver segments (III, IV, V, and VI). (C and D) Tissue wedges from liver segments and (E and F) bile duct tissue from non-WI livers ($n = 3$) were analyzed for lipid peroxidation measurements (MDA) at each time point. The results of all segments ($n = 12$) were pooled per time point. (G) Delivery of 10 mg/kg FXT-001 (orange) administered via cold flush and supplemented in preservation solution in non-WI livers ($n = 3$) and WI livers ($n = 3$) was quantified using mass spectrometry (VIB Metabolomics Core, KU Leuven). One non-WI liver treated with vehicle (0.9% NaCl) was used as control.

(legend continued on next page)

(H) AUC of AST concentrations during reperfusion generated based on data displayed in Figure 3B.
(I) The cumulative bile volume represents the sum of bile volume measured at each time point during reperfusion (n = 3 for vehicle; n = 4 for FXT-001). Three datapoints were excluded due to technical failure (both groups) and leakage of perfusate in the bile duct (vehicle).
(J) Perfusate pH during reperfusion.
(K–N) Perfusate concentration of IL-1β, IL-6, IL-8, and TNF-α during reperfusion.
(O and P) MDA concentration in liver and bile duct tissue at baseline (T0), after WI (T1), after flush, after SCS and after 1, 3, and/or 6 h of reperfusion.
(Q) MDA concentration in bile collected during reperfusion.
(R) Relative GPX4 expression in liver tissue at baseline, after WI, after flush, after cold storage, and after 1, 3, and 6 h of reperfusion.
(S) H&E staining of porcine liver graft biopsies collected after flush, following cold storage, and after 1 and 6 h reperfusion. Magnification, 10×; scale bar, 500 μm.
(T) Immunofluorescence staining of 4-HNE (green) in porcine liver grafts after cold storage and after 6 h reperfusion. Nuclear DNA was counterstained with DAPI (blue). Magnification 20×; scale bar, 50 μM.
(U) TUNEL (red) staining of porcine liver grafts after 6 h reperfusion, with DAPI (blue) used for nuclear counterstaining. Magnification 20×; scale bar, 50 μM. Due to a perfusion machine malfunction, one experiment ended at 4 h of reperfusion; therefore, only four treated samples are included (porcine 10 excluded). Unpaired t tests with Welch's correction and Mann-Whitney test were used in (H) and (I), respectively. Longitudinal data were analyzed using two-way ANOVA or mixed-effects model when appropriate. Tukey's multiple comparison or an uncorrected Fisher's least significant difference were applied to compare two conditions within the datasets (J–R). Due to technical failure, two datapoints are missing in the FXT-001 group at time points 5 and 6 h of reperfusion (J–R).
See also Video S2.

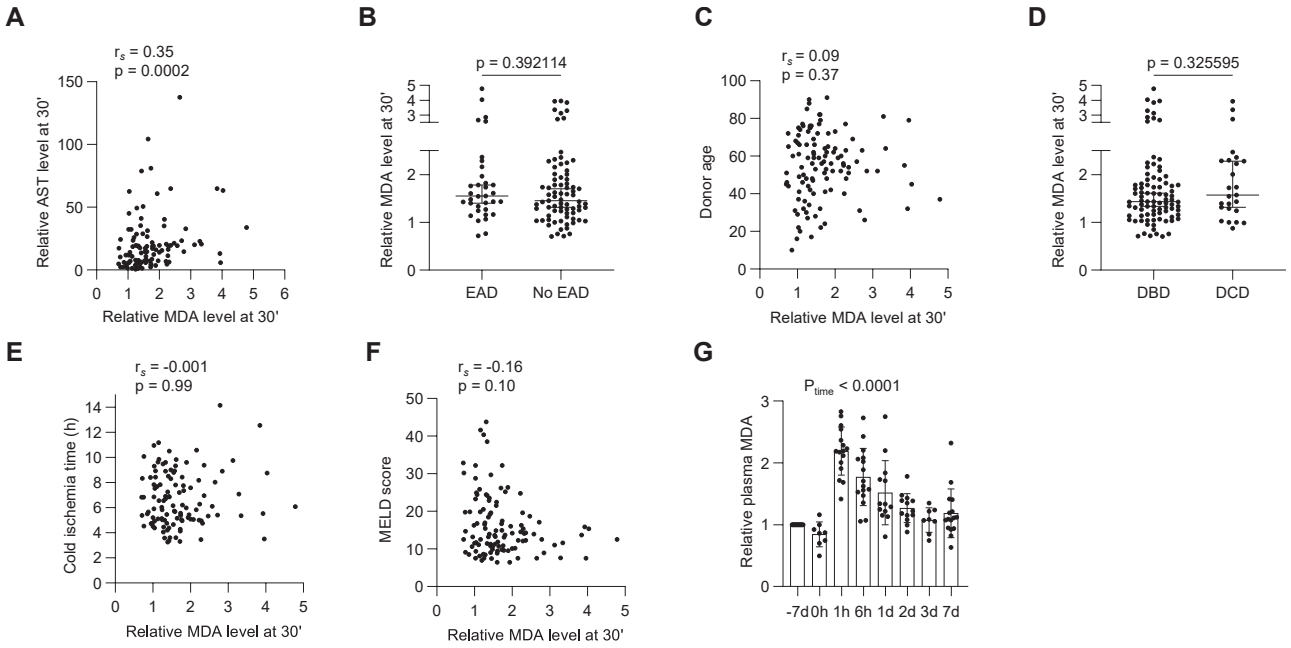

Figure S4. Plasma MDA peaks within 1 h post transplantation in human liver transplants as well as orthotopic pig-to-baboon cardiac xenotransplants, related to Figure 4

(A) Dot plot of relative AST concentrations correlated to relative MDA concentrations at 30 min post transplantation.

(B) Relative MDA concentration at 30 min post transplantation in patients diagnosed with EAD and patients not diagnosed with EAD.

(C) Dot plot of donor age correlated to relative MDA concentration at 30 min post transplantation.

(D) Relative MDA concentration at 30 min post transplantation in patients receiving DCD and DBD grafts.

(E) Dot plot of CIT correlated to relative MDA concentrations at 30 min post transplantation.

(F) Dot plot of MELD score correlated to relative MDA concentration at 30 min post transplantation.

(G) Relative MDA concentrations in plasma samples of baboons (n = 17) undergoing orthotopic pig-to-baboon heart xenotransplantation. Measurements were obtained before (−7 days) and after (0 h to day 7) cessation of cardiopulmonary bypass following xenotransplantation. Spearman correlations (r_s) were used to assess correlation between two variables (A, C, E, and F). A Mann-Whitney test was used to assess difference in MDA expression between different groups (B and D). Longitudinal data were analyzed using a mixed-effects model, and Tukey's multiple-comparison test was applied to assess differences between the two conditions within each dataset (G).

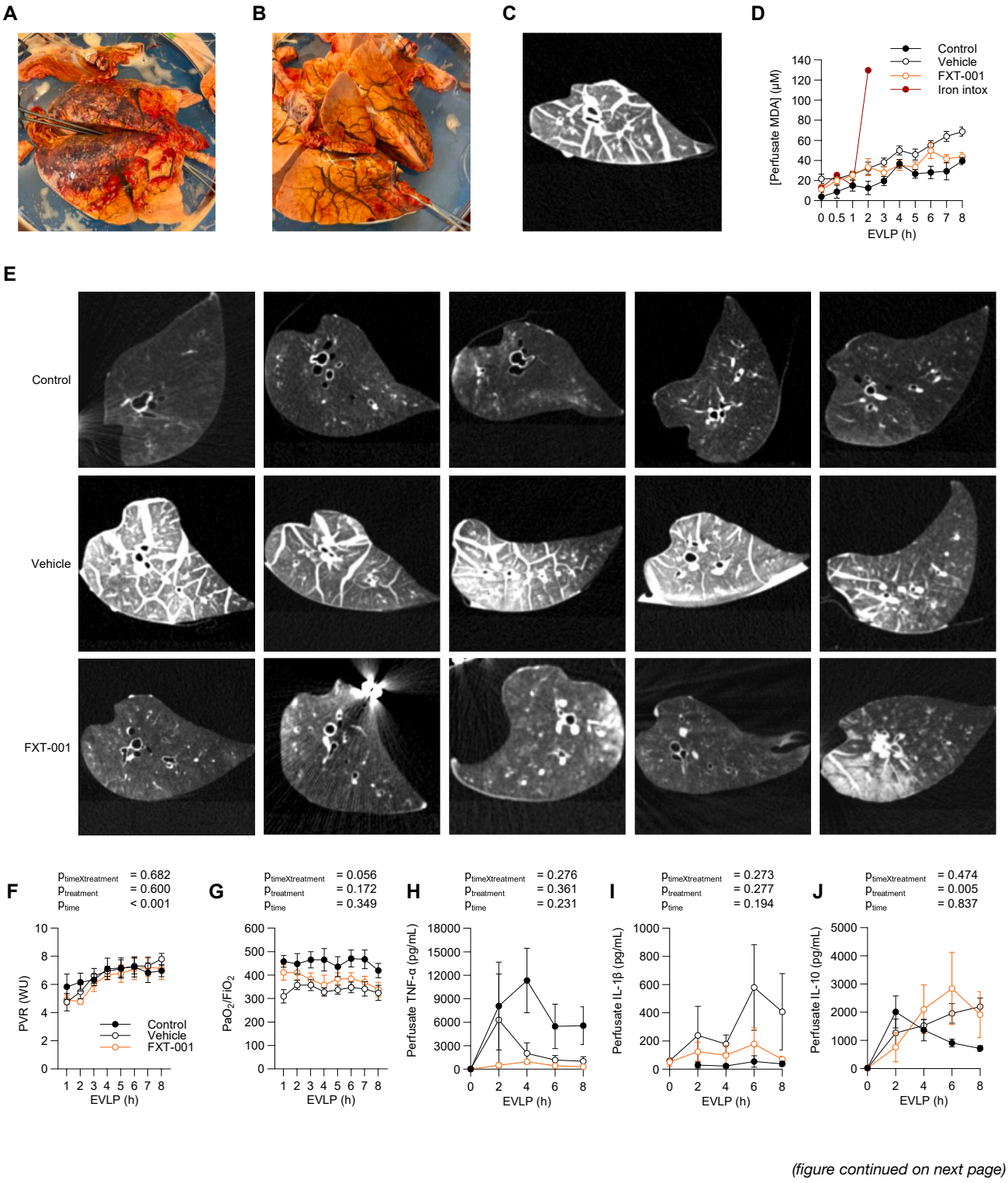

(figure continued on next page)

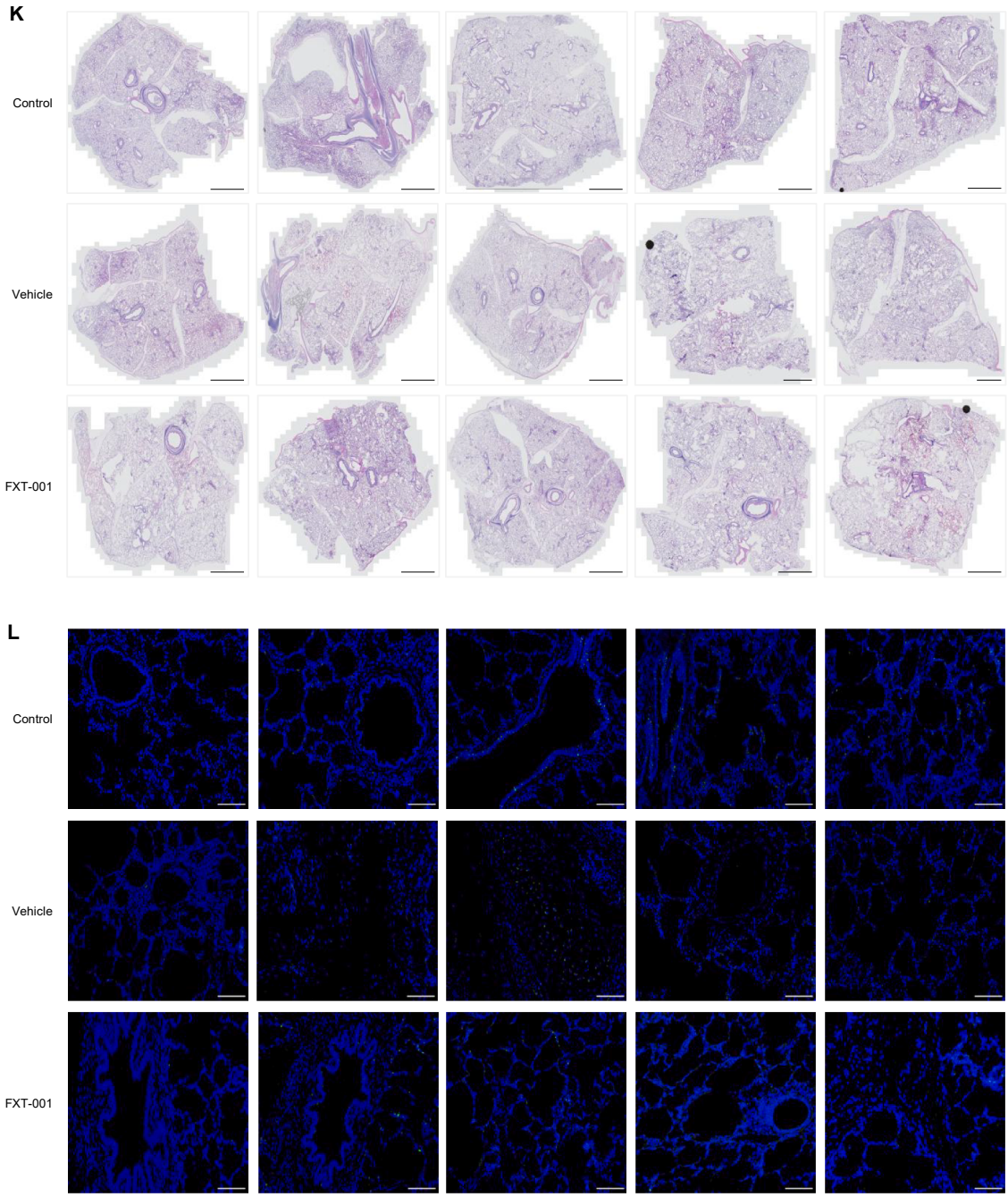

Figure S5. Ferroptosis inhibition protects porcine lung grafts during EVLP, related to Figure 5

(A and B) Prone (A) and supine (B) positioning of a porcine lung graft treated with 300 mg kg^{-1} iron sulfate to induce iron intoxication (n = 1).
(C) CT images (left lower lobe) of the same porcine, iron-intoxicated lung graft.
(D) Perfusate MDA concentrations during porcine normothermic EVLP (n = 1 iron-intoxicated lung).
(E) CT images (left lower lobe) of porcine lung grafts.
(F) PVR.
(G) Oxygenation capacity (PaO_2/FiO_2 ratio).
(H–J) Perfusate TNF-α, IL-1β, and IL-10 concentrations. INF-γ data were below the detection limit and therefore not shown. All analyses were performed with n = 5 per group, unless stated otherwise. MDA, malondialdehyde; PVR, pulmonary vascular resistance; PaO_2, arterial partial pressure of oxygen; FiO_2, fraction of inspired oxygen; TNF-α, tumor necrosis factor alpha; IL, interleukin. Data are presented as the mean ± SEM.

(legend continued on next page)

(K) H&E staining of (right lower lobe) porcine lung graft. Magnification 10×, scale bar, 5 mm.
(L) Immunofluorescence 4-HNE (green) staining of (right lower lobe) porcine lung graft. DAPI (blue) dye was used to stain nuclear DNA. Magnification 20×, scale bar, 50 μM. Repeated measures two-way ANOVA followed by Tukey's post hoc analysis was used to compare differences between vehicle and FXT-001 (D and F–J).
See also Videos S3–S6.

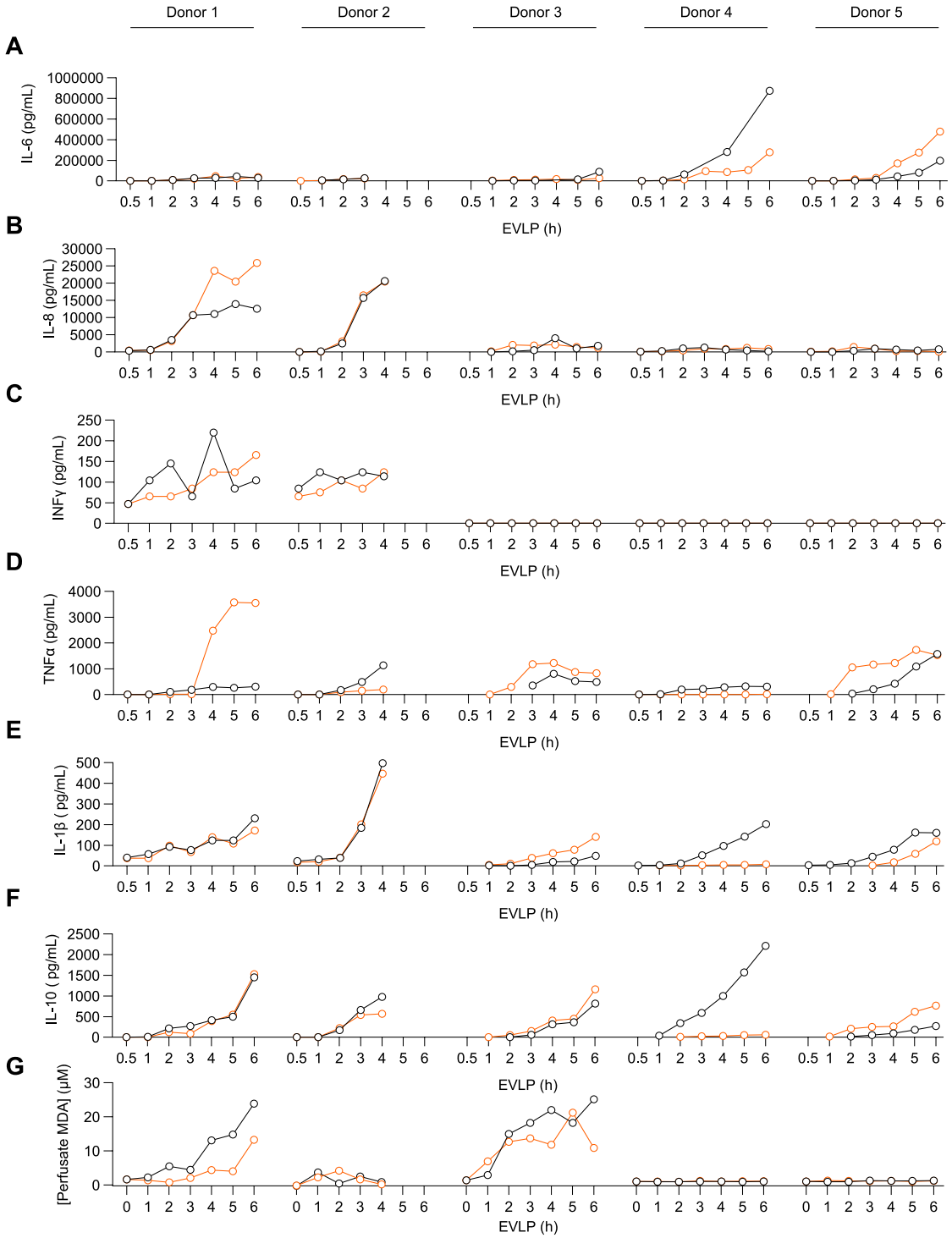

Figure S6. Cytokine and MDA concentrations in human lung grafts during EVLP, related to Figure 6

(A–F) Concentrations of IL-6, IL-8, IFN-γ, TNF-α, IL-1β, and IL-10 in lung perfusate solution measured up to 6 h of normothermic EVLP.

(G) MDA concentrations in perfusate samples from declined human lung grafts measured at baseline and at different time points during normothermic EVLP. IFN-γ, interferon-gamma; IL, interleukin.

See also Videos S7 and S8.